

Characterization of Electro-Optic Phase Modulations for Arbitrary
Unitary Transformations

by

Sarah Jade Ashby

A dissertation accepted and approved in partial fulfillment of the
requirements for the degree of

Doctor of Philosophy

in Physics

Dissertation Committee:

Hailin Wang, Chair

Brian J. Smith, Advisor

Ben Farr, Core Member

Andrew H. Marcus, Institutional Representative

University of Oregon

Fall 2024

© 2024 Sarah Jade Ashby

This work is openly licensed via a Creative Commons

Attribution-NonCommercial-NoDerivs (CC BY-NC-ND 4.0) License



DISSERTATION ABSTRACT

Sarah Jade Ashby

Doctor of Philosophy in Physics

Title: Characterization of Electro-Optic Phase Modulations for Arbitrary Unitary Transformations

Temporal modes are a viable framework for quantum information science and technology, being well suited for use in integrated photonics and single-mode fiber networks. Techniques for temporal mode transformations have been developed that allow for control over the mode structure, as well as beam-splitter like transformations between temporal modes. However, no scheme to perform targeted multi-mode unitary transformations on temporal modes has yet been achieved. In this dissertation we present a pathway toward implementing programmable arbitrary unitary transformations on temporal modes using phase-only operations. We present techniques to measure and characterize phase modulations via electro-optic phase modulation. We demonstrate the ability to generate and measure arbitrary phase modulations in the time and frequency domains using photonic arbitrary waveform generation.

This dissertation includes previously published co-authored material.

CURRICULUM VITAE

NAME OF AUTHOR: Sarah Jade Ashby

GRADUATE AND UNDERGRADUATE SCHOOLS ATTENDED:

University of Oregon, Eugene, OR
University of Portland, Portland, OR

DEGREES AWARDED:

Doctor of Philosophy, Physics, 2024, University of Oregon
Master of Science, Physics, 2024, University of Oregon
Bachelor of Science, Physics, 2016, University of Portland

AREAS OF SPECIAL INTEREST:

Optics
Quantum Optics

PROFESSIONAL EXPERIENCE:

Graduate Research Assistant, University of Oregon, 2017-2024

PUBLICATIONS:

J. Ashby et al., *Temporal mode transformations by sequential time and frequency phase modulation for applications in quantum information science*, *Opt. Express* **28** (2020), no. 25, 38376–38389, DOI: 10.1364/OE.410371

ACKNOWLEDGMENTS

First and foremost, I would like to express my deepest gratitude to my advisor, Dr. Brian Smith, for his exceptional guidance and unwavering support throughout my PhD journey. Your profound knowledge, insightful feedback, and extraordinary patience have been instrumental in shaping my research abilities and my growth as a doctoral student. Thank you for believing in my potential, and for encouraging me throughout these challenging and transformative times.

I am particularly grateful to all the current and former members of our research group who have made this journey both enriching and enjoyable. To Matthew Brown, Amy Soudachanh, Clark Embleton, Jack Lichtmann, Mostafa El Demery, and Sofiane Merkouche; I am truly fortunate to have had opportunity to work and learn alongside you. Thank you for all the discussions and the company as we worked in the lab together. I wish you all the best and hope you achieve amazing things.

I owe special thanks to Dr. Markus Allgaier and Dr. Valérian Thiel for their exceptional support in the lab. Your assistance has been invaluable throughout this work, and I appreciate the time you took to help when needed.

Last but not least, I am deeply grateful to my wonderful family for over three decades of unwavering support. Your encouragement and understanding have been my strength as I continue to learn and grow on this challenging journey.

TABLE OF CONTENTS

Chapter	Page
LIST OF FIGURES	9
LIST OF TABLES	15
1. MOTIVATION	16
1.1. Light	16
1.2. Quantum Information and Quantum Technologies	17
1.3. Thesis Outline	19
2. THEORY	21
2.1. Electromagnetic Waves	21
<i>Pulsed modes</i>	23
2.2. Temporal Modes	25
2.3. Wigner Function	28
2.4. Temporal mode transformations	29
2.5. Gaussian Pulses	31
2.6. Hermite-Gauss mode basis	32
<i>Sub-spaces</i>	34
3. CHARACTERIZATION OF SPECTRAL AND TEMPORAL PHASE MOD- ULATION	35
3.1. Spectral Phase	35
<i>Linear Spectral Phase</i>	36
<i>Quadratic Spectral Phase</i>	39

3.2.	Temporal Phase	46
	<i>Linear Temporal Phase</i>	46
	<i>Quadratic Temporal Phase</i>	49
	<i>Time Lens</i>	52
3.3.	Electro-optic Modulation	55
	<i>Creating Linear and Quadratic Phases</i>	57
3.4.	Measuring the frequency shift	60
3.5.	Bandwidth Manipulation	68
	<i>Theory</i>	68
	<i>Measuring the bandwidth</i>	69
3.6.	Spectral Interferometry	73
	<i>Theory</i>	74
	<i>Measurement</i>	76
4.	ARBITRARY UNITARY TRANSFORMATIONS	81
4.1.	Theory	81
4.2.	Temporal Mode Implementation	82
4.3.	Simulation	83
	<i>Single-mode transformations</i>	84
	<i>Multi-mode transformations</i>	86
	<i>Demultiplexing</i>	91
	<i>Practical Comments</i>	92
5.	CREATING AND MEASURING ARBITRARY PHASE MODULATIONS	95
5.1.	Photonic Arbitrary Waveform Generation	95
	<i>Pulse Shaping</i>	96
	<i>Photonic Arbitrary Waveform Generation.</i>	98

5.2. Creating Arbitrary Phase Modulations	98
5.3. Measurement	100
6. FUTURE STEPS AND CONCLUSIONS	106
6.1. Single-Shot Phase Characterization	106
6.2. Cavity Configuration for Arbitrary Unitary Transformations	107
6.3. Conclusions	109
REFERENCES CITED	111

LIST OF FIGURES

Figure	Page
2.1. An example of the Wigner function $W(t, \omega)$ and its marginals.	29
2.2. The first four Hermite-Gaussian modes	33
3.1. The effect of a linear spectral phase on a temporal mode. Using Gaussian mode as an example. (a) displays the Gaussian spectral profile (blue) along with a linear spectral phase (red dashed line). (b) In the time domain the original temporal profile is shown in blue. The temporal profile of the modulated mode, in red, is shifted by a time C	38
3.2. The effect of a linear spectral phase on the Wigner of a Gaussian temporal mode. (a) displays the initial Gaussian Wigner function of the mode prior to phase modulation. (b) After the linear spectral phase modulation the Gaussian is shifted along the temporal axis by a time $\Phi^{(1)}$	39
3.3. The effect of a quadratic spectral phase on a temporal mode. Using Gaussian mode as an example. (a) displays the Gaussian spectral profile (blue) along with a quadratic spectral phase (red dashed line). (b) In the time domain the original temporal profile is shown in blue. The temporal profile of the modulated mode, in red, has an expanded width proportional to the coefficient $\Phi^{(2)}$	42

- 3.4. The effect of a quadratic spectral phase on the Wigner of a Gaussian temporal mode. (a) displays the initial Gaussian Wigner function of the mode prior to phase modulation. (b) After the quadratic spectral phase modulation the Gaussian is sheared in the direction of the temporal axis by a factor proportional to $\Phi^{(2)}$. From the shearing, it is seen that lower frequencies arrive at a time earlier than higher frequencies. 43
- 3.5. The effect of a linear temporal phase on a temporal mode. Using Gaussian mode as an example. (a) displays the Gaussian temporal profile (blue) along with a linear temporal phase (red dashed line). (b) In the frequency domain the original temporal profile is shown in blue. The spectral profile of the modulated mode, in red, is shifted by a frequency D 48
- 3.6. The effect of a linear temporal phase on the Wigner of a Gaussian temporal mode. (a) displays the initial Gaussian Wigner function of the mode prior to phase modulation. (b) After the linear temporal phase modulation the Gaussian is shifted along the frequency axis by a time C 49
- 3.7. The effect of a quadratic temporal phase on a temporal mode. Using Gaussian mode as an example. (a) displays the Gaussian temporal profile (blue) along with a quadratic temporal phase (red dashed line). (b) In the frequency domain the original spectral profile is shown in blue. The spectral profile of the modulated mode, in red, has an expanded bandwidth proportional to the coefficient K 52

3.8.	The effect of a quadratic temporal phase on the Wigner of a Gaussian temporal mode. (a) displays the initial Gaussian Wigner function of the mode prior to phase modulation. (b) After the quadratic temporal phase modulation the Gaussian is sheared in the direction of the frequency axis by a factor proportional to K . From the shearing, it is seen that points earlier in the temporal profile are shifted to lower frequencies and later points are shifted to higher frequencies.	53
3.9.	The setup for measuring the frequency shift. The pulse originates from a Ti:Saph laser. It is split into two paths. In one the probe path the polarization is controlled by a wave plates, and a spectral filter is used so that the frequency shift of more visible. The other path has a delay line and a fast photodiode, the resulting signal is amplified and used as the driving signal for the EOM. An electronic output from the EOM is monitored on the Oscilloscope to observe the time of arrival. The output of the EOM is measured on a spectrometer.	62
3.10.	The linear temporal phase shifts the central frequency of the pulse in proportion to its slope. There several positive and negative peaks, implying that the phase oscillates. The maximum frequency shift is 0.69 THz and -0.79 THz.	63
3.11.	The reconstructed temporal phase	64
3.12.	The impulse response of the Thorlabs DX25CF photodiode, given in the specifications.	66
3.13.	A 4th degree polynomial fit to the first peak of the reconstructed phase.	67

3.14. The setup for measuring the bandwidth. The pulse originates from a Ti-Sapphire laser. It is split into two paths. In one the probe path the polarization is controlled by a wave plates, and a spectral filter is used so that the frequency shift of more visible. A 56.5 m spool of fiber is used to chirp the pulse. The other path has a delay line and a fast photodiode, the resulting signal is amplified and used as the driving signal for the EOM. An electronic output from the EOM is monitored on the Oscilloscope to observe the time of arrival. The output of the EOM is measured on a spectrometer.	70
3.15. The bandwidth shift	71
3.16. The spectral interferometry setup.	76
3.17. The measured spectrum showing interference fringes. The modulated spectrum is in blue, and the unmodulated spectrum is in red. With fringe spacing determined by the temporal delay.	77
3.18. The inverse Fourier transform of the interference spectrum. The two sidebands contain the phase information.	78
3.19. The phase measured using spectral interferometry, reconstructed from the fft.	79
4.1. The proposed experimental setup	83
4.2. The transformation of a 0th-order HG mode to a 5-th order HG mode for various values of N . After 4 steps the transformed begins to have the 6-peaked character of the 5-th order HG mode. After 8 steps the transformation achieves a very high fidelity of $F = 0.994$	86

4.3.	The transformation of a 0th-order HG mode to a 5-th order HG mode is simulated for various values of the bandwidth B and the fidelity F is computed after a certain number of steps. The fidelity appears to approach a maximum that depends on the bandwidth.	87
4.4.	The temporal amplitude of the output modes of the simulated beam-splitter transformation. The simulation assumes a phase modulation bandwidth of $B = 20$ GHz, optimized over $N = 6$ phase steps. The temporal amplitude of the target modes are displayed as dashed lines.	89
4.5.	The Hilbert-Schmidt fidelity and the success probability as a function of the number of phase modulation steps for the two and four mode beam-splitter transformations	91
4.6.	Demultiplexing the temporally overlapped Gaussian (turquoise), a 1 st -order HG (black), and 2 nd -order HG (magenta) pulses into temporally separated Gaussian pulses for an increasing number of phase modulation steps. The initial temporally overlapping HG pulses and target pulses have widths $\sigma = 20$ ps. The target Gaussian modes are separated by 200 ps. The average fidelity is shown for each transformation.	93
5.1.	Diagram of a 4f-line Fourier transform pulse shaper. Made up of a pair of gratings and lenses, and a mask placed at the Fourier plane.	96
5.2.	A schematic of the pulse shaper. A polarization controller (PC) set the polarization to the optimal wavelength. A grating disperses the beam across a range of angles. The cylindrical mirror (CM) collimates the beam. An SLM is placed at the Fourier plane of the mirror. The reflected beam is spatially separated and directed to a fiber coupler by the mirror M2.	99

5.3.	The PAWG measurement setup uses the same measurement scheme to the spectral interferometry measurement in chapter 3, but the output of the delay line is sent through PAWG. The pulse shaper is equipped with a SLM to shape the spectrum of the pulse. A 250m optical fiber is used for frequency-to-time mapping. The output of the fiber is detected by the fast photodiode, converting it into an RF signal that is amplified and used to drive the EOM.	101
5.4.	The 1272 x 1024 pixel mask sent to the SLM, used to create a pulse with a triangular shape.	102
5.5.	The measurement of the phase modulation using a triangular driving signal created using PAWG. The phase is extracted from a spectral interferometry measurement.	103
5.6.	The measurement of a rectangular phase created using PAWG. The phase is extracted from a spectral interferometry measurement.	104
5.7.	The measurement of a phase created using PAWG, consisting of a series of peaks. The phase is extracted from a spectral interferometry measurement.	105
6.1.	The proposed schematic for a setup that can efficiently perform many successive phase modulations to implement arbitrary unitary transformations.	108

LIST OF TABLES

Table	Page
3.1. The quadratic temporal phase coefficient $\Phi_t^{(2)}$ and the third-order phase coefficient $\Phi_t^{(3)}$ for each peak of the reconstructed phase, along with the computed apertures.	68
3.2. The bandwidth for each peak of Fig. 3.15, and the corresponding phase curvature K	72

CHAPTER 1

MOTIVATION

1.1 Light

Light has been used for thousands of years, in many forms, to communicate information over long distances. This is in part due to the many degrees of freedom that can be used to encode information. Most importantly, light is used because of its speed. Traveling at the speed of light allows light to be one of the fastest forms of communication, capable of delivering information at high data rates.

One of the earliest examples of light being used for communication is smoke signals. Found in many societies around the world, as in the case of indigenous Americans and in ancient China, smoke signals can be used to deliver messages such as arranging meetings or warning of enemy invasions. Produced by fires, puffs of smoke can be controlled and manipulated using blankets or skins, the shape and number of the puffs determining the meaning of the message. As the puffs rise into the sky, they can be seen from many miles away.

A more modern example is that of radio. In radio communication a transmitter uses an antenna to produce electromagnetic waves in the radio spectrum, these radio waves are detected by an antenna at the receiver. Information can be encoded in radio waves using many different types of modulation. Two of the major forms of modulation used in radio are amplitude modulation (AM) and frequency modulation (FM). AM radio encodes information by modulating the amplitude of a carrier wave, an AM radio receiver decodes this information by filtering out the carrier wave and extracting the modulation signal. AM radio is vulnerable to noise and interference that affects the amplitude of the electric voltage in the antenna of the transmitter and the receiver, by comparison FM radio is more resistant to

noise. FM encodes the information by modulating the frequency of the carrier wave in a small frequency band around the carrier frequency, this is demodulated by the receiver using narrow band frequency filters about the carrier frequency and the information is decoded.

Another type of modulation in radio communication is phase modulation, in which the phase of the carrier wave is modulated instead of the amplitude. One form of phase modulation is phase-shift keying (PSK), which is a digital modulation method used to encode bits or a string of binary data in a finite number of phase patterns. PSK is commonly used in Wi-fi and Bluetooth communication.

Another important form of communication using light is fiber optic communication. In fiber optics information is encoded in light in the visible or infrared spectrum and transmitted through glass fibers. Information can be encoded in the light using the same types of modulation used in radio communication. Fiber optic cables have the advantage of being resistant to electrical noise and interference. Optical fibers also can be used with a wide bandwidth of light, which allows for higher data rates using wavelength-division multiplexing.

1.2 Quantum Information and Quantum Technologies

The quantum nature of light and matter has been demonstrated to have a variety of properties that can be used for many purposes. The development of quantum technologies, which aim to utilize the non-classical nature of quantum systems such as superposition and entanglement to perform certain tasks, is an area of increasing interest. Examples of emerging quantum technologies include quantum computing, quantum communications and quantum enhanced sensing.

The development of quantum computing began with a quantum mechanical

model of a Turing machine [Ben80; Ben82], demonstrating theoretically that a quantum system can be used for computation. This raised a question about the possibility that quantum computers may be able to perform more efficiently than classical computers, particularly in the simulation of quantum systems [Fey82; DP85]. The potential for a quantum advantage led to a search for applications for which a quantum computer would be well suited and algorithms by which they can compute information faster than classical computing algorithms. An important result of this is Shor's algorithm [Sho94; Sho97], which allows the factoring of large numbers in polynomial time, compared to the exponential time it takes classical computers to perform the same task. A quantum computer running Shor's algorithm could break a number of public-key cryptography schemes that rely on the assumption that factoring large numbers is a difficult problem for classical computers.

While quantum computing may make classical cryptography schemes vulnerable to attack, quantum cryptography schemes have been developed that can enable physically-secure communication. The first quantum cryptography protocol was the BB84 protocol [BB14]. The protocol works by encoding a quantum bit (qubit) in one of two orthogonal states of a physical system, which can be sent over a channel to the receiver. The receiver then decodes the qubit by measuring in a randomly chosen basis. If the qubit was measured in the same basis it was encoded in then the measurement outcome can be used as part of bit string to generate a private key. This protocol is considered secure due to the no-cloning theorem, since a potential eavesdropper who attempts to measure the state of the qubit will change it.

The physical implementation of quantum computers and other quantum technologies can take many forms, from trapped ions [Mon+14] to superconducting systems [NPT99]. We can have many quantum computers and quantum technologies exchanging information with each other through a quantum network [Kim08]. Such

a network would need a way to exchange quantum information between each node through a quantum channel. Light is a very suitable choice for this task, because photons do not interact strongly with their environment, so the quantum information and quantum correlations would be preserved. However, each node of the quantum network may be comprised of disparate physical systems, for example trapped-ion quantum computers at one node and a neutral atom quantum computer at another, which interface with light of different wavelengths and with different bandwidths. This motivates the present work that aims to manipulate the light to make it compatible with each node without losing information. Such a transformation is a unitary transformation. More generally, techniques to control the temporal mode structure of quantum optical pulses enables the use of temporal modes wide range of applications in quantum information science and technology [Bre+15]. Techniques have been developed to allow frequency shifting, linear shifting in the time domain, compression and expansion of the bandwidth, and perform mode-selective beam-splitter-like transformations [Ans+17], all using unitary transformations. However, no scheme to perform targeted multimode unitary transformations on temporal modes has yet been achieved.

1.3 Thesis Outline

Here we present a pathway to implement general transformations for temporal modes. We show theoretically that any unitary transformation on temporal modes can be performed using a series of phase operations in the time and frequency domains. Numerical simulations show that several key transformations on temporal modes can be performed with greater than 95% fidelity using experimentally feasible specifications. Initial experimental efforts to implement this scheme are also

presented.

In chapter 2 we introduce the theoretical background of temporal modes, which are solutions to Maxwell equations for the electromagnetic field for traveling wave packets. We focus on the form of the solutions in the temporal domain, and the Fourier conjugate frequency domain, which leads to the development of temporal modes. We introduce the Wigner representation as a way of representing the temporal modes. And we describe how transformations on the temporal modes are defined.

Chapter 3 describes the common tools used to implement phase modulation in the frequency and time domains and how these can be used to control and manipulate temporal modes. We look in depth at the effect of linear and quadratic phase modulation in both the time and frequency domains, and we present methods to experimentally characterize these phases for verification purposes.

In chapter 4 we present the general theoretical framework for implementing programmable arbitrary unitary transformations on temporal modes using a sequential application of temporal and spectral phase modulation. We show simulations of targeted transformations that can be realized using realistic device parameters, optimized over a finite number of time and frequency phase applications. This chapter contains previously published material co-authored with Valérian Thiel, Markus Allgaier, Peru d'Ornellas, Alex O. C. Davis, and Brian J. Smith

In chapter 5 we investigate experimental approaches to generate specific temporal phase modulation using optical pulse shaping high-bandwidth photodetection to implement a photonic arbitrary waveform generation. We show measurements of several temporal phases demonstrated in this manner.

In chapter 6 discusses the future steps required to implement the proposed architecture for realizing arbitrary unitary temporal mode transformations.

CHAPTER 2

THEORY

In this chapter we discuss solutions to electromagnetic wave equation with a focus on the part of these solutions in temporal domain. We develop a description of the temporal modes, and we describe the effect of transformations on these temporal modes.

2.1 Electromagnetic Waves

To begin we describe the theory behind the temporal modes of light. The electric field $\mathbf{E}(\mathbf{r}, \mathbf{t})$ and magnetic field $\mathbf{B}(\mathbf{r}, t)$ are related through the Maxwell equations, which in free space have the form

$$\nabla \cdot \mathbf{E} = 0 \tag{2.1}$$

$$\nabla \cdot \mathbf{B} = 0 \tag{2.2}$$

$$\nabla \times \mathbf{E} = -\frac{\partial \mathbf{B}}{\partial t} \tag{2.3}$$

$$\nabla \times \mathbf{B} = \mu_0 \epsilon_0 \frac{\partial \mathbf{E}}{\partial t} \tag{2.4}$$

Here μ_0 and ϵ_0 are the magnetic permeability and the electric permittivity of free space, respectively. By taking the curl of equation (2.3), using the vector identity

$$\nabla \times \nabla \times \mathbf{F} = -\nabla^2 \mathbf{F} + \nabla(\nabla \cdot \mathbf{F}), \tag{2.5}$$

and using equation (2.1), we arrive at the wave equation for the electric field

$$\nabla^2 \mathbf{E} - \mu_0 \epsilon_0 \frac{\partial^2 \mathbf{E}}{\partial t^2} = 0 \tag{2.6}$$

Similarly we can find the wave equation for the magnetic field from equations (2.4) and (2.2). Here we note that this leads to $c = 1/\sqrt{\mu_0 \epsilon_0}$ being the speed of light in vacuum.

Solutions to the wave equation for a given experimental configuration define a set of modes that can be excited with photons. The plane wave modes $\{\phi_{\mathbf{k},\sigma}(\mathbf{r}, t)\}$ where

$$\phi_{\mathbf{k},\sigma}(\mathbf{r}, t) = \mathbf{e}_{\mathbf{k},\sigma} e^{i(\mathbf{k}\cdot\mathbf{r} - \omega_{\mathbf{k}}t)} \quad (2.7)$$

form a basis in which the field can be expanded. Here $\mathbf{e}_{\mathbf{k},\sigma}$ is a unit polarization vector that is orthogonal to the wave vector \mathbf{k} and labeled by index $\sigma = 1, 2$. The frequency of the plane wave is related to the magnitude of the wave vector as dictated by the wave equation $\omega_{\mathbf{k}}^2 = |\mathbf{k}|^2$. Thus the electric field can be expressed as

$$\mathbf{E}(x, y, z, t) = \sum_{\sigma} \int \frac{d^3k}{(2\pi)^3} \tilde{\psi}_{\sigma}(\mathbf{k}) \mathbf{e}_{\mathbf{k},\sigma} e^{i(\mathbf{k}\cdot\mathbf{r} - \omega_{\mathbf{k}}t)} \quad (2.8)$$

where the wave vector amplitude $\tilde{\psi}_{\sigma}(\mathbf{k})$ is determined by the experimental configuration.

Typically one encounters a beam-like geometry, such as found in an optical fiber or wave guide. Taking z to be the direction the beam travels, x and y are said to be the transverse directions. In this geometry the wave vector distribution $\tilde{\psi}_{\sigma}(\mathbf{k})$ is concentrated around a particular wave vector $\mathbf{k}_0 = k_0 \mathbf{e}_z$. In this case the wave vector amplitude can be factored into longitudinal, $\tilde{\alpha}_{\sigma}(k_z - k_0)$, and transverse, $\tilde{u}_{\sigma}(k_x, k_y)$, amplitudes $\tilde{\psi}_{\sigma}(\mathbf{k}) \approx \tilde{\alpha}_{\sigma}(k_z - k_0) \tilde{u}_{\sigma}(k_x, k_y)$. For a fixed polarization (dropping the σ subscript, the field can then be expressed as

$$\mathbf{E}(x, y, z, t) = \alpha(z - ct) u(x, y, z) \mathbf{e} e^{i(k_0 z - \omega_0 t)}, \quad (2.9)$$

where \mathbf{e} is the polarization unit vector,

$$\alpha(z) = \int \frac{dk}{2\pi} \tilde{\alpha}(k) e^{ikz}, \quad (2.10)$$

is the longitudinal amplitude of the field,

$$u(x, y, z) = \int \frac{d^2k}{(2\pi)^2} \tilde{u}(k_x, k_y) e^{i(k_x x + k_y y)} e^{-i(k_x^2 + k_y^2)z/(2k_0)}, \quad (2.11)$$

is the transverse amplitude of the field. The transverse amplitude has a slowly varying dependence on z , which arises from taking $k_z = \sqrt{k^2 - k_x^2 - k_y^2} \approx k_0 - (k_x^2 + k_y^2)/(2k_0)$. This is often called the paraxial approximation. Note that the longitudinal amplitude takes the form of a traveling wave packet with carrier wave $e^{i(k_0z - \omega_0t)}$ modulated by the slowly-varying envelope $\alpha(z - ct)$. This approach is often called the slowly-varying envelope approximation and forms the basis on which the temporal modes are constructed.

Pulsed modes

We now turn our attention to the longitudinal modes introduced above. Here the modes take the form

$$f(z, t) = \alpha(z - ct)e^{i(k_0z - \omega_0t)}, \quad (2.12)$$

where k_0 is the carrier wave vector and ω_0 is the carrier wave frequency. The wave equation for such modes is

$$\left[\partial_z^2 - \frac{1}{c^2} \partial_t^2 \right] f(z, t) = 0. \quad (2.13)$$

Note that this can be expanded out using

$$\partial_z \alpha(z - ct)e^{i(k_0z - \omega_0t)} = [ik_0\alpha(z - ct) + \partial_z \alpha(z - ct)]e^{i(k_0z - \omega_0t)}, \quad (2.14)$$

$$\partial_z^2 \alpha(z - ct)e^{i(k_0z - \omega_0t)} = [2ik_0\partial_z \alpha(z - ct) + \partial_z^2 \alpha(z - ct) - k_0^2 \alpha(z - ct)]e^{i(k_0z - \omega_0t)}, \quad (2.15)$$

$$\partial_t \alpha(z - ct)e^{i(k_0z - \omega_0t)} = [-i\omega_0\alpha(z - ct) + \partial_t \alpha(z - ct)]e^{i(k_0z - \omega_0t)}, \quad (2.16)$$

and

$$\partial_t^2 \alpha(z-ct) e^{i(k_0 z - \omega_0 t)} = [-2i\omega_0 \partial_t \alpha(z-ct) + \partial_t^2 \alpha(z-ct) - \omega_0^2 \alpha(z-ct)] e^{i(k_0 z - \omega_0 t)}. \quad (2.17)$$

to give the equation

$$\left[\partial_z^2 - \frac{1}{c^2} \partial_t^2 + 2ik_0 \left(\partial_z + \frac{1}{c} \partial_t \right) \right] \alpha(z-ct) = 0, \quad (2.18)$$

for the envelope function. The slowly-varying envelope approximation (SVEA) assumes that the spatial and temporal variation of the wavepacket amplitude is small compared to the carrier wavelength and frequency. This means that the second-order derivatives in Eq. (2.18) are neglected, giving rise to the wave equation for the slowly varying amplitude

$$\left(\partial_z + \frac{1}{c} \partial_t \right) \alpha(z-ct) = 0. \quad (2.19)$$

An example solution for this equation is a Gaussian pulse

$$\alpha_G(t-z/c) = \frac{1}{\sqrt{T}\sqrt{\pi}} e^{-(t-z/c)^2/(2T^2)}. \quad (2.20)$$

From now on we will neglect the spatial dependence (dropping z), effectively going into the moving reference frame of the pulse. We can then express the field $E(t) = E_0 \alpha(t)$. We can also represent this field in the frequency domain by the spectral amplitude $\tilde{E}(\omega)$. These representations are related to each other by the Fourier transform

$$E(t) = \int_{-\infty}^{\infty} \tilde{E}(\omega) e^{-i\omega t} d\omega \quad (2.21)$$

and

$$\tilde{E}(\omega) = \frac{1}{2\pi} \int_{-\infty}^{\infty} E(t) e^{i\omega t} dt \quad (2.22)$$

Although the solutions to the wave equation can be complex, to correspond to physical fields we are only interested in solutions $E(t)$ that are real. The the spectrum will satisfy $\tilde{E}(\omega) = \tilde{E}^*(\omega)$. This spectrum includes negative frequencies, which we do not want. To solve this we can define the positive and negative frequency parts of the spectrum $\tilde{E}^{(\pm)}(\omega)$ such that

$$\tilde{E}(\omega) = \tilde{E}^{(+)}(\omega) + \tilde{E}^{(-)}(\omega) \quad (2.23)$$

From this we can get a complex, positive frequency electric field

$$E^{(+)}(t) = \frac{1}{2\pi} \int_{-\infty}^{\infty} \tilde{E}^{(+)}(\omega) e^{-i\omega t} d\omega \quad (2.24)$$

and a corresponding negative frequency part of the electric field $\tilde{E}^{(-)}(t)$. The real electric field can be reconstructed from

$$E(t) = E^{(+)}(t) + E^{(-)}(t) \quad (2.25)$$

Because it is a complex function, we can express the positive frequency field in terms of a real amplitude and a complex phase $E(t) = A(t)e^{i\theta(t)}$. From now on we shall focus on this part of the electric field.

2.2 Temporal Modes

From now on we focus on the temporal solutions of the wave equation of the form $E(t) = E_0\alpha(t)e^{-i\omega_0 t}$. Where ω_0 is called the central frequency and $\alpha(t)$ is the temporal profile. In general $\alpha(t)$ can be any complex function of time. Firstly let us consider the case of the delta functions $\delta(t - \tau)$, which could be viewed as an impulse centered on time τ , defined as

$$\delta(t - \tau) = \begin{cases} 0, & t \neq \tau \\ \infty, & t = \tau \end{cases} \quad (2.26)$$

such that the integral over the delta function is

$$\int_{-\infty}^{\infty} \delta(t - \tau) dt = 1. \quad (2.27)$$

We can define the overlap (or inner product) between two temporal profiles $\alpha(t)$ and $\beta(t)$ as the integral $\int \alpha^*(t)\beta(t)dt$, where $\alpha^*(t)$ is the complex conjugate of $\alpha(t)$. We have suppressed the limits on the integral, which we will continue to do so from here on. Then the inner product between two delta functions centered at different times is

$$\int \delta^*(t - \tau')\delta(t - \tau)dt = \delta(\tau - \tau'). \quad (2.28)$$

Here we see that the inner product between two delta functions is zero everywhere unless they are the same delta function. Therefore the set of delta functions is orthonormal.

Any temporal profile $\alpha(t)$ can be expressed in terms of the delta functions as the integral $\alpha(t) = \int \alpha(\tau)\delta(t - \tau)d\tau$, where the coefficients are $\alpha(\tau) = \int \delta^*(t - \tau)\alpha(t)dt$. This is known as completeness.

The delta functions form an orthonormal set with an inner product that is a complete basis for the set of temporal modes, these are the conditions for a Hilbert space. With that in mind we can rewrite these functions in Dirac notation. Let us call $|\tau\rangle$ the mode with the temporal profile $\delta(t - \tau)$. A general mode with the temporal profile $\alpha(t)$ can be written as $|\alpha\rangle$. Since this is a Hilbert space we can also define a Hermitian conjugate $\langle\alpha|$ as the mode with the temporal profile $\alpha^*(t)$. Then in this notation the inner product between two temporal modes $|\alpha\rangle$ and $|\beta\rangle$ is defined as

$$\langle\beta|\alpha\rangle = \int \beta^*(t)\alpha(t)dt \quad (2.29)$$

The completeness of the delta function basis can be expressed as

$$|\alpha\rangle = \int |\tau\rangle \langle \tau | \alpha \rangle d\tau \quad (2.30)$$

Where the coefficients are the inner products $\langle \tau | \alpha \rangle = \int \delta^*(t - \tau) \alpha(t) dt$. The above equation is equivalent to the action of an identity operator on the mode $|\alpha\rangle = \hat{I}|\alpha\rangle$, where

$$\hat{I} = \int |\tau\rangle \langle \tau | d\tau \quad (2.31)$$

This is the completeness relation for the $|\tau\rangle$ basis.

The $|\tau\rangle$ modes are a basis from which any temporal profile can be constructed. Since we know that the electric field has an equivalent representation in the frequency domain, it follows that there is an equivalent basis for the spectral profile. We can define the basis modes $|\Omega\rangle$ to be the delta functions $\delta(\omega - \Omega)$. The inner product of the modes is

$$\langle \Omega' | \Omega \rangle = \int \delta^*(\omega - \Omega') \delta(\omega - \Omega) d\omega = \delta(\Omega' - \Omega) \quad (2.32)$$

Which is similar to the inner product in the temporal domain. Thus any spectral mode $|\alpha\rangle$ can be expressed in terms of the frequency modes as

$$|\alpha\rangle = \int |\Omega\rangle \langle \Omega | \alpha \rangle d\Omega \quad (2.33)$$

Then analogously to the time domain, the completeness relation in the frequency domain is

$$\hat{I} = \int |\Omega\rangle \langle \Omega | d\Omega \quad (2.34)$$

The temporal profile and the spectral profile are closely related via the Fourier transform.

$$\tilde{\alpha}(\omega) = \int \alpha(t) e^{i\omega t} dt \quad (2.35)$$

This relationship means that anything affects the temporal profile will have an effect on the spectral profile, and vice-versa.

2.3 Wigner Function

A temporal mode, $|\alpha\rangle$, can be described in the time domain by the temporal profile, $\alpha(t) = \langle t|\alpha\rangle$, and in the frequency domain by its spectral profile, $\tilde{\alpha}(\omega) = \langle \omega|\alpha\rangle$. We have seen that both of these representations are intricately related via the Fourier transform. An alternative way of representing a temporal mode is to use the chronocyclic Wigner function. This is a powerful tool for analyzing temporal modes, representing them in a way that displays both their temporal and spectral behavior. The Wigner function is a two-dimensional function of time and frequency, which allows the frequency and time properties of the mode to be visualized simultaneously. Consider a pulse that has a temporal profile $\alpha(t)$ and corresponding spectral profile $\tilde{\alpha}(\omega)$. the Wigner function associated with this mode is

$$W_\alpha(t, \omega) = \frac{1}{2\pi} \int \alpha\left(t + \frac{\tau}{2}\right) \alpha^*\left(t - \frac{\tau}{2}\right) e^{-i\omega\tau} d\tau \quad (2.36)$$

It can also be written in an alternative way using the frequency representation $\tilde{\alpha}(\omega)$ as

$$W_\alpha(t, \omega) = \frac{1}{(2\pi)^2} \int \tilde{\alpha}\left(\omega + \frac{\Omega}{2}\right) \tilde{\alpha}\left(\omega - \frac{\Omega}{2}\right) e^{i\Omega t} d\Omega \quad (2.37)$$

An important property of the Wigner function is that the integral over time and frequency gives one (assuming the modes are normalized)

$$1 = \int \int W(\omega, t) d\omega dt. \quad (2.38)$$

Additionally, the marginal integrals of the Wigner function gives the modulus squared of the mode function in the time or frequency domain

$$\int W_\alpha(t, \omega) dt = |\tilde{\alpha}(\omega)|^2, \quad (2.39)$$

and

$$\int W_\alpha(t, \omega) d\omega = |\alpha(t)|^2. \quad (2.40)$$

An example of the Wigner function is shown in Fig. 2.1 for an arbitrary temporal mode, along with its time and frequency marginals found by integrating over the opposite variable.

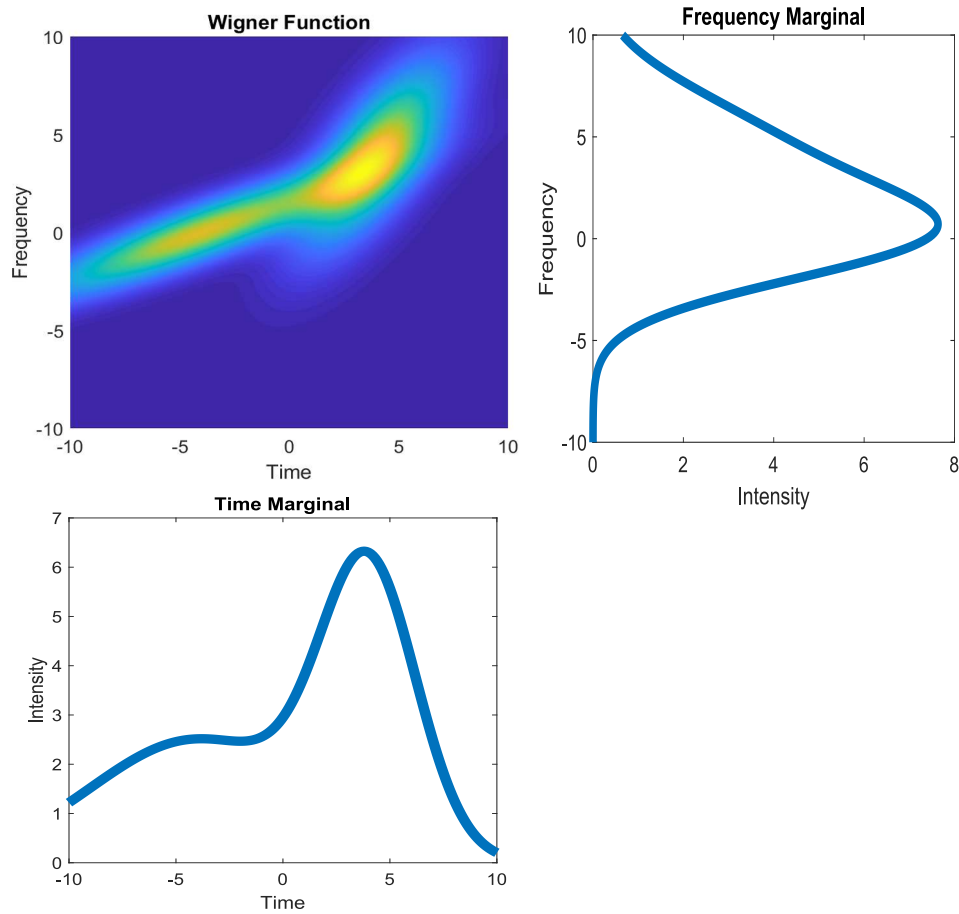


Figure 2.1. An example of the Wigner function $W(t, \omega)$ and its marginals.

2.4 Temporal mode transformations

Unitary linear transformations between temporal modes are analogous to beam splitter transformations on beams of light. Such transformations are important in numerous classical and quantum optical applications. For example, such transfor-

mations can be used as mode sorters for improved classical and quantum sensing, Boson sampling and linear-optics quantum computing.

A unitary temporal mode transformation can be viewed as an operator that maps one set of temporal modes $\{|\alpha_j\rangle\}$ to another set of temporal modes $\{|\beta_j\rangle\}$. Owing to the unitarity of the transformation, the mapping preserves the inner product between modes and thus the normalization of the modes. Consider a transformation with an operator \hat{U} on the temporal modes

$$\hat{U}|\alpha_i\rangle = \sum_j U_{i,j}|\alpha_j\rangle, \quad (2.41)$$

where $U_{i,j} = \langle\alpha_i|\hat{U}|\alpha_j\rangle$ is the matrix element of the transformation in the $\{|\alpha_j\rangle\}$ mode basis.

The matrix elements of the unitary transformation allow us to easily calculate the effect of the transformation. One can also use the δ -function basis to represent the temporal mode transformation

$$\hat{U} = \iint U(t, t')|t\rangle\langle t'|dt dt', \quad (2.42)$$

where the matrix elements are

$$U(t, t') = \langle t|\hat{U}|t'\rangle. \quad (2.43)$$

The inner product of the transformed mode is

$$\langle\alpha_i|\hat{U}^\dagger\hat{U}|\alpha_i\rangle = \langle\alpha_i|\hat{U}^{-1}\hat{U}|\alpha_i\rangle = \langle\alpha_i|\alpha_i\rangle = 1, \quad (2.44)$$

where we used the fact that we are considering unitary transformations in which $\hat{U}^\dagger = \hat{U}^{-1}$. Keep in mind that unitary transformations necessarily preserve orthogonality of modes. One example of a unitary transformation is the Fourier transform. This can be expressed by the operator

$$\hat{F} = \int |\omega\rangle\langle t|e^{i\omega t}dt, \quad (2.45)$$

where ω is the frequency. The Fourier transform of one of the temporal basis modes is

$$\hat{F}|\tau\rangle = \int |\omega\rangle\langle t|\tau\rangle e^{i\omega t} \delta(t - \tau) dt = \int |\omega\rangle \delta(t - \tau) e^{i\omega t} dt = e^{i\omega\tau} |\omega\rangle. \quad (2.46)$$

2.5 Gaussian Pulses

The temporal and spectral profiles of a temporal mode can in general be any complex function of the variables. However, there are some that are of particular interest to us. The most important of these is are Gaussian pulses. These are defined by the temporal profile

$$g_T(t) = \frac{1}{\sqrt{T}\sqrt{\pi}} e^{-t^2/(2T^2)}, \quad (2.47)$$

where T is a parameter that determines the temporal duration of the pulse. The full width at half max (FWHM) is $T\sqrt{2\ln 2}$. An important property of a Gaussian pulse is that the corresponding spectral profile, from the Fourier transform, is also a Gaussian

$$\tilde{g}_T(\omega) = \sqrt{2T}\sqrt{\pi} e^{-\omega^2 T^2/2} \quad (2.48)$$

If we add a quadratic temporal phase to the Gaussian pulse, the result is also a Gaussian

$$g_T(t) = \frac{1}{\sqrt{T}\sqrt{\pi}} e^{-t^2/(2T^2)} e^{i\kappa t^2/2}. \quad (2.49)$$

This quadratic phase does not change the temporal duration of the pulse, however it does modify the spectral bandwidth as we will see. Quadratic temporal phase is often called a time lens, in analogy to the spatial phase a lens imprints on a wavefront of a beam.

2.6 Hermite-Gauss mode basis

The states $|\tau\rangle$ and $|\Omega\rangle$ form a set of states that act as a continuous basis for the temporal-spectral domain, with overlap $\langle\omega|t\rangle = e^{i\omega t}$. However, we can also construct other bases. One such basis is the set of Hermite-Gaussian temporal modes, $\{|n\rangle\}$ where the temporal profile is given by

$$\psi_n(t) = \langle t|n\rangle = \frac{1}{\sqrt{2^n n! T \sqrt{\pi}}} H_n(t/T) e^{-t^2/2T^2} \quad (2.50)$$

where $n = 0, 1, 2, \dots$ and $H_n(t/T)$ is the n -th order Hermite polynomial. This is an infinite set of modes that spans the space of temporal modes (i.e. they are complete), with completeness relation

$$\hat{I} = \sum_{n=0}^{\infty} |n\rangle\langle n|, \quad (2.51)$$

being the identity. The modes are also orthonormal with the usual overlap

$$\langle m|n\rangle = \int \psi_m^*(t) \psi_n(t) dt = \delta_{mn}. \quad (2.52)$$

The first four Hermite-Gaussian modes are shown in Figure 2.2.

A general temporal mode, $|\alpha\rangle$, with temporal amplitude $\alpha(t) = \langle t|\alpha\rangle$ can be expanded in terms of the Hermite-Gaussian modes as

$$|\alpha\rangle = \sum_n c_n |n\rangle, \quad (2.53)$$

where the expansion coefficients are given by the overlap of the mode $|\alpha\rangle$ and the n th HG mode

$$c_n = \langle n|\alpha\rangle = \int \psi_n^*(t) \alpha(t) dt. \quad (2.54)$$

Remarkably, the spectral profile of a Hermite-Gaussian mode is also a Hermite-Gaussian function, which is found by taking the Fourier transform. Another interesting property of the Hermite-Gaussian modes is that they overlap in time and

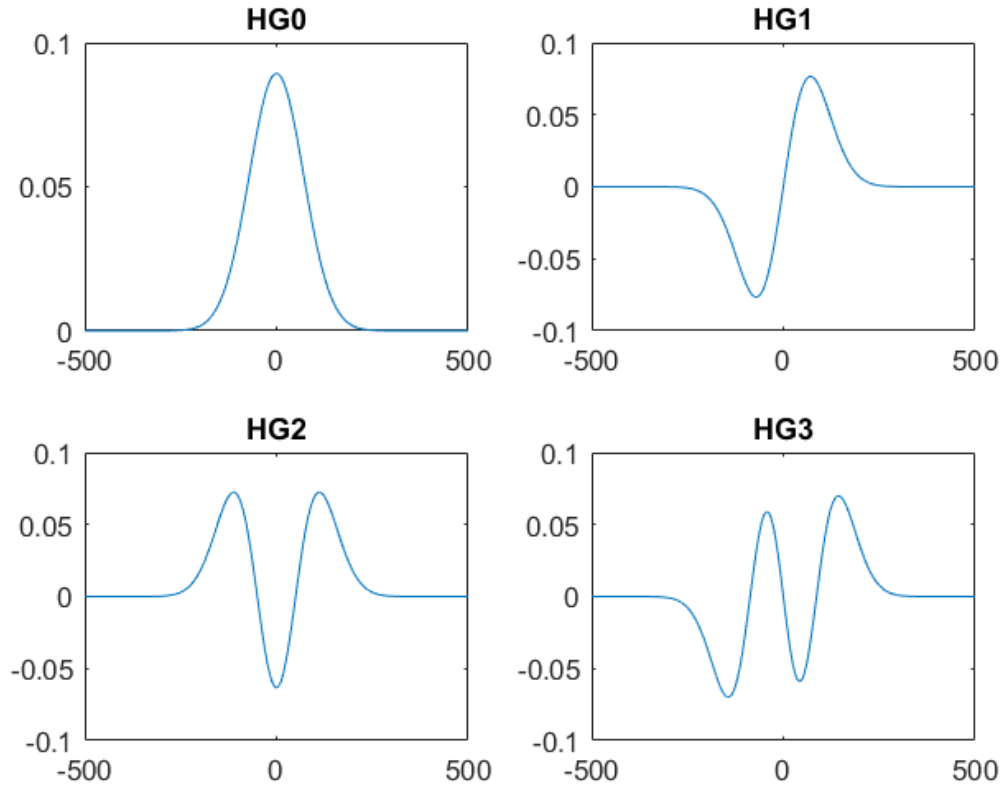


Figure 2.2. The first four Hermite-Gaussian modes

frequency, yet remain orthogonal to one another. These modes can be used as an information encoding basis for quantum information.

A temporal mode transformation \hat{U} can be expressed in the Hermite-Gaussian mode basis as

$$\hat{U} = \sum_{m,n} U_{m,n} |m\rangle \langle n|, \quad (2.55)$$

where the matrix elements of the operator, $U_{m,n}$, are given by

$$U_{m,n} = \langle m | \hat{U} | n \rangle. \quad (2.56)$$

We will further explore temporal mode transformations between the Hermite-Gaussian modes and other sets of modes that can act as a mode sorter.

Sub-spaces

A basis for the temporal modes may have sub-spaces with their own complete set of basis vectors. For instance the first two Hermite-Gaussian modes are a basis for the space of modes of the form $|u\rangle = c_0|0\rangle + c_1|1\rangle$ where c_0 and c_1 are scalar coefficients. Any mode in this subspace can be conveniently written as a two dimensional vector

$$\mathbf{u} = \begin{pmatrix} c_0 \\ c_1 \end{pmatrix}. \quad (2.57)$$

A temporal mode transformation \hat{M} that operates only on this subspace (leaving all other modes unchanged) can be written as a matrix

$$\mathbf{M} = \begin{pmatrix} m_{00} & m_{01} & & \\ m_{10} & m_{11} & & \\ & & 1 & 0 \\ & & 0 & 1 \end{pmatrix}, \quad (2.58)$$

where we have truncated the matrix to only four Hermite-Gaussian modes, but the unit diagonal elements extend on for all higher-order modes. Here the components of the transformation matrix are defined by the matrix elements $m_{ij} = \langle i|M|j\rangle$. In the following chapters we will utilize the mathematics of temporal modes and transformations on temporal modes developed here.

CHAPTER 3

CHARACTERIZATION OF SPECTRAL AND TEMPORAL PHASE MODULATION

The previous chapter set out the mathematical foundation of temporal modes and transformations between different. In this chapter, we introduce a set of important transformations in the form of linear and quadratic phase modulation in the temporal and spectral domains. These elementary operations display remarkable control over the temporal modes, and form a complete set of transformations on Gaussian modes, in the sense that by using appropriate combinations of linear and quadratic phases one can transform one Gaussian pulse to any other Gaussian pulse.

Temporal phase modulation has been demonstrated to have usefulness in a variety of applications. They can be used to shift the frequency of light, also known as spectral shearing, and can be used on single photons [Wri+17]. This can be used to characterize a single photon pulse using spectral shearing interferometry [Dav+18]. It can also be used to manipulate the bandwidth of a pulse [Kar+17], which can be paired with spectral dispersion to create a time lens [SFG13]. All of these applications are useful for instance, in mode-matching between different nodes of a quantum network.

Here we describe these phase modulations, their numerous uses, and show how they can be implemented and measured in the lab.

3.1 Spectral Phase

We begin by looking at phase modulation in the spectral domain. It is useful to start here because spectral phase modulation is commonly encountered and easy

to achieve. In general, we can write a spectral phase modulation of a pulse as a power series about the central frequency of the pulse

$$\Phi(\omega) = \Phi^{(0)} + \Phi^{(1)}(\omega - \omega_0) + \frac{1}{2}\Phi^{(2)}(\omega - \omega_0)^2 + \dots \quad (3.1)$$

where ω_0 is the central frequency of the pulse. For convenience we will suppress reference to ω_0 for most of this chapter unless otherwise needed.

Linear Spectral Phase

To demonstrate the effect of spectral phase modulation on a pulse we start with the first non-trivial example, a linear spectral phase. For this purpose we consider the phase

$$\Phi(\omega) = \Phi^{(1)}\omega, \quad (3.2)$$

where $\Phi^{(1)}$ is constant coefficient. To see how this spectral phase affects a test pulse with temporal mode $u_{in}(t)$, we apply this as a phase shift to the spectral amplitude of the pulse $\tilde{u}_{in}(\omega)$. The resulting spectral amplitude is simply

$$\tilde{u}_{out}(\omega) = \tilde{u}_{in}(\omega)e^{i\Phi^{(1)}\omega}. \quad (3.3)$$

In the spectral domain the original spectral amplitude is simply multiplied by the corresponding phase factor $\Phi(\omega)$. This is a unitary transformation on the mode that does not affect the spectral intensity and thus the spectral bandwidth for any applied phase $\Phi(\omega)$, not just linear spectral phase. However, a spectral phase can modify the temporal amplitude though. We can see the effect of the spectral phase in the time domain by applying the inverse Fourier transform

$$u_{out}(t) = \frac{1}{2\pi} \int \tilde{u}_{in}(\omega)e^{i\Phi^{(1)}\omega}e^{-i\omega t}d\omega. \quad (3.4)$$

By combining the phase terms, this is just the inverse Fourier transform of $\tilde{u}_{in}(\omega)$ where the kernel has been modified to $e^{-i\omega(t-\Phi^{(1)})}$. Then we find that the output temporal amplitude has been modified to

$$u_{out}(t) = \frac{1}{2\pi} \int \tilde{u}_{in}(\omega) e^{-i\omega(t-\Phi^{(1)})} d\omega = u_{in}(t - \Phi^{(1)}). \quad (3.5)$$

This is an example of the Fourier transform shift theorem. The output temporal amplitude is the original temporal amplitude delayed by time $\Phi^{(1)}$, as shown in Fig. 3.1. This means that a linear spectral phase modulation generates a time delay on a temporal mode that can be controlled by changing the slope of the phase. This can also be seen in reverse. Any time delay on a temporal mode, caused by a delay line or any other source of delay, will cause a spectral phase modulation of the mode that is linear in frequency. This is a simple effect, but one that is very useful and ubiquitous in optics, which shows that phase modulation in the frequency domain is a tool for controlling and manipulating the temporal amplitude of pulses.

This demonstrates the effect of a linear spectral phase modulation on a general temporal mode $u(t)$. To visualize this with a specific example, it is useful to see how this linear phase affects a Gaussian mode. Consider a Gaussian mode with a spectral amplitude $\tilde{u}_{in}(\omega)$ such that the modulated spectral amplitude is

$$\tilde{u}_{out}(\omega) = \sqrt{2T\sqrt{\pi}} e^{-\omega^2 T^2/2} e^{i\Phi^{(1)}\omega}. \quad (3.6)$$

As we see again this is a multiplication by a phase factor that has no effect on the spectral intensity itself. But if we look in the time domain we find that the temporal amplitude becomes

$$u_{out}(t) = \frac{1}{\sqrt{T\sqrt{\pi}}} e^{-(t-\Phi^{(1)})^2/(2T^2)}. \quad (3.7)$$

So as expected, in the time domain the output is Gaussian mode of the same width, but shifted by a time $\Phi^{(1)}$. This effect is shown in Fig. 3.1.

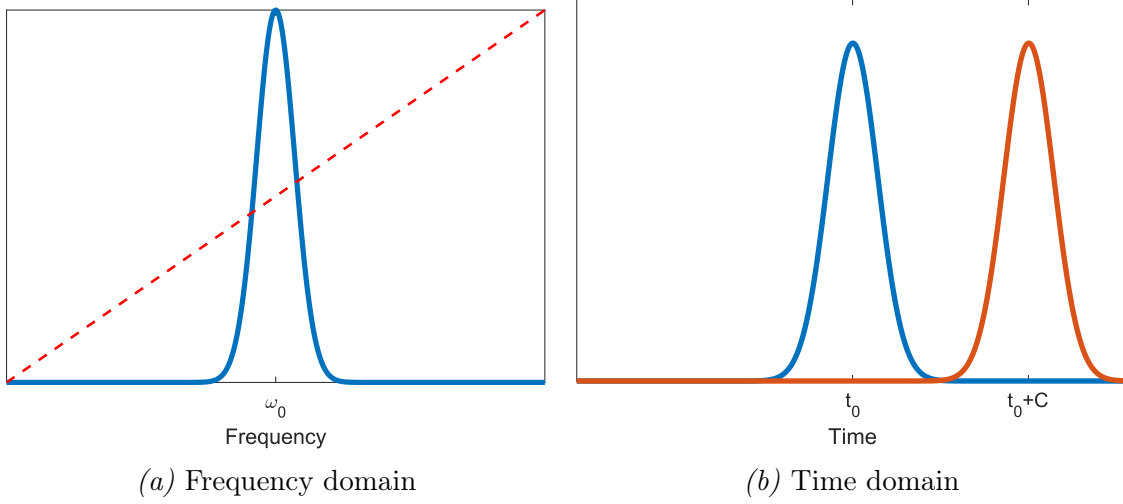


Figure 3.1. The effect of a linear spectral phase on a temporal mode. Using Gaussian mode as an example. (a) displays the Gaussian spectral profile (blue) along with a linear spectral phase (red dashed line). (b) In the time domain the original temporal profile is shown in blue. The temporal profile of the modulated mode, in red, is shifted by a time C .

We can also look at the effect of the linear spectral phase on the Wigner function of a temporal mode. If we consider that the temporal mode with amplitude $u_{in}(t)$ has the Wigner function

$$W_{in}(t, \omega) = \int u\left(t + \frac{\tau}{2}\right) u^*\left(t - \frac{\tau}{2}\right) e^{i\omega\tau} d\tau \quad (3.8)$$

Then after the linear spectral phase modulation it becomes

$$W_{out}(t, \omega) = \int u\left(t - \Phi^{(1)} + \frac{\tau}{2}\right) u^*\left(t - \Phi^{(1)} - \frac{\tau}{2}\right) e^{i\omega\tau} d\tau = W_{in}(t - \Phi^{(1)}, \omega). \quad (3.9)$$

Like the temporal amplitude itself, the Wigner function for the mode is delayed by a time $\Phi^{(1)}$. This transformation is equivalent to a translation along the time axis of a duration $\Phi^{(1)}$. Fig. 3.2 shows the effect of this transformation on a the Wigner function for a Gaussian mode. The Gaussian shape of the mode is retained while being shifted along the time axis.

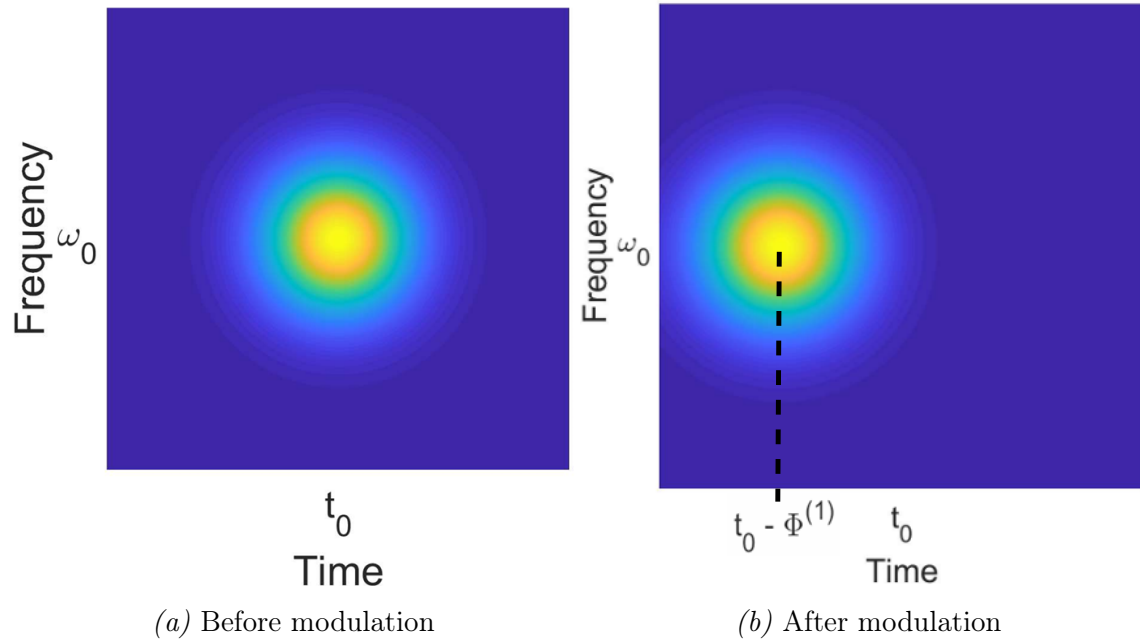


Figure 3.2. The effect of a linear spectral phase on the Wigner of a Gaussian temporal mode. (a) displays the initial Gaussian Wigner function of the mode prior to phase modulation. (b) After the linear spectral phase modulation the Gaussian is shifted along the temporal axis by a time $\Phi^{(1)}$.

Quadratic Spectral Phase

The next step in demonstrating the useful and power of phase modulation is to look at the effect of a quadratic spectral phase on a temporal mode. Here we consider a phase of the form

$$\Phi(\omega) = \Phi^{(2)}\omega^2/2, \quad (3.10)$$

where $\Phi^{(2)}$ is a constant coefficient that is related to the curvature of the phase. We use this to modulate a mode with a spectral amplitude $\tilde{u}_{in}(\omega)$, such that the output is

$$\tilde{u}_{out}(\omega) = \tilde{u}_{in}(\omega)e^{i\Phi^{(2)}\omega^2/2}. \quad (3.11)$$

As in the case of the linear phase, and in fact for any spectral phase modulation, this does not affect the spectral intensity. To see a measurable effect we have to look again at the resulting temporal amplitude, which is

$$u_{out}(t) = \frac{1}{2\pi} \int \tilde{u}_{out}(\omega) e^{-i\omega t} d\omega = \frac{1}{2\pi} \int \tilde{u}_{in}(\omega) e^{i\Phi^{(2)}\omega^2/2} e^{-i\omega t} d\omega. \quad (3.12)$$

This can also be computed by using the fact that the Fourier transform of a product of two functions is the convolution of their individual Fourier transforms.

$$u_{out}(t) = \frac{1}{\sqrt{-2\pi i\Phi^{(2)}}} \int u_{in}(\tau) e^{-i(t-\tau)^2/(2\Phi^{(2)})} d\tau. \quad (3.13)$$

This is the general form of a mode modulated with a quadratic spectral phase, but to see how this effects the properties of a mode we can look at specific examples. Once again, for convenience, we consider the example of a Gaussian mode which has the spectral amplitude

$$\tilde{u}_{in}(\omega) = \sqrt{2T\sqrt{\pi}} e^{-\omega^2 T^2/2}, \quad (3.14)$$

where $1/T$ is the spectral bandwidth. Likewise, the temporal amplitude is

$$u_{in}(t) = \frac{1}{\sqrt{T\sqrt{\pi}}} e^{-t^2/(2T^2)}. \quad (3.15)$$

So the temporal width of this mode is T .

If we modulate the spectral amplitude by the quadratic phase given above, the resulting temporal amplitude is given by the Fourier transform

$$u_{out}(t) = \sqrt{\frac{T}{2\pi\sqrt{\pi}}} \int e^{-\omega^2 T^2/2} e^{i\Phi^{(2)}\omega^2/2} e^{-i\omega t} d\omega. \quad (3.16)$$

After computing the integral, this becomes

$$u_{out}(t) = \frac{1}{\sqrt{T\sqrt{\pi}(1 - i\Phi^{(2)}/T^2)}} e^{-t^2/[2(T^2 - i\Phi^{(2)})]}. \quad (3.17)$$

Taking the modulus squared of this we obtain

$$|u_{out}(t)|^2 = \frac{1}{T\sqrt{\pi}(1 + (\Phi^{(2)}/T^2)^2)} e^{-t^2/[T^2(1+(\Phi^{(2)}/T^2)^2)]}. \quad (3.18)$$

We see that the temporal duration of the modulated mode becomes

$$T' = T\sqrt{1 + (\Phi^{(2)}/T^2)^2}. \quad (3.19)$$

So we see that, as depicted in Fig. 3.3, the effect of a quadratic spectral phase is to expand the temporal width of a mode by an amount that depends on the coefficient of the phase. The amount of expansion is larger for modes with smaller temporal widths. Note that we found a linear spectral phase corresponds to a time delay of a pulse $\phi^{(1)}(\omega) = \tau\omega$. So we see that quadratic spectral phase can be thought of as a frequency dependent time delay, $\phi^{(2)}(\omega) = \tau(\omega)\omega = (\Phi^{(2)}\omega/2)\omega$, with time delay $\tau(\omega) = \Phi^{(2)}\omega/2$. This arises in dispersive materials in which different frequencies travel at different speeds leading to what is known as a chirped pulse in which the red part of the spectrum arrives prior to the blue part of the spectrum for normal dispersion.

Alternatively, we can the properties of a chirped pulse from the time domain by examining the imaginary part of the argument of the Gaussian temporal envelope

$$\arg \left\{ e^{-i\Phi^{(2)}t^2/[2(T^4+(\Phi^{(2)})^2)]} \right\} = -i\Phi^{(2)}t^2/[2(T^4 + (\Phi^{(2)})^2)]. \quad (3.20)$$

This can be viewed as a time-varying frequency. So for this pulse we can define the instantaneous frequency

$$\omega(t) = \omega_0 + \frac{\Phi^{(2)}}{2(T^4 + \Phi^{(2)})^2}t, \quad (3.21)$$

where we have included the central frequency of the pulse, ω_0 , which we have omitted for most of this chapter.

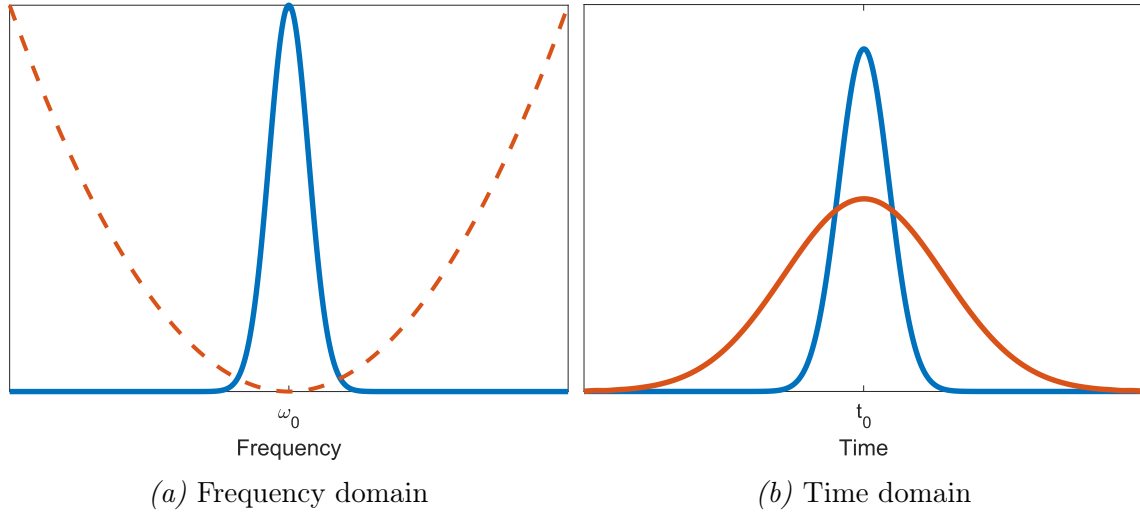


Figure 3.3. The effect of a quadratic spectral phase on a temporal mode. Using Gaussian mode as an example. (a) displays the Gaussian spectral profile (blue) along with a quadratic spectral phase (red dashed line). (b) In the time domain the original temporal profile is shown in blue. The temporal profile of the modulated mode, in red, has an expanded width proportional to the coefficient $\Phi^{(2)}$.

The instantaneous frequency has a linear time dependence. This means that if we used a fast spectrometer to measure the spectral intensity over time, instead of measuring a constant spectrum $I_{in}(\omega)$, we would find different frequency components at each time, this is the effect of "chirp" on a pulse. Red light will arrive before blue light, or blue light will arrive before red light, depending on the sign of the quadratic phase coefficient $\Phi^{(2)}$. Since the spectral intensity remains constant throughout this phase modulation, this means that the spectral components of the mode have been dispersed throughout its increased temporal duration.

It is convenient to visualize a chirped mode using the Wigner function representation. If the Wigner function for the original mode is $W_{in}(t, \omega)$, then Wigner function for this modulated mode is

$$W_{out}(t, \omega) = W_{in}(t - \Phi^{(2)}\omega/2, \omega) \quad (3.22)$$

This amounts to a frequency-dependent shearing along the time axis by a factor of $\Phi^{(2)}\omega/2$. The marginal along the frequency axis remains the same. This transformation of a quadratic spectral phase on the Wigner function for a Gaussian mode is shown in Fig. 3.4. This shows that the spectral components of the pulse are stretched to arrive at different times.

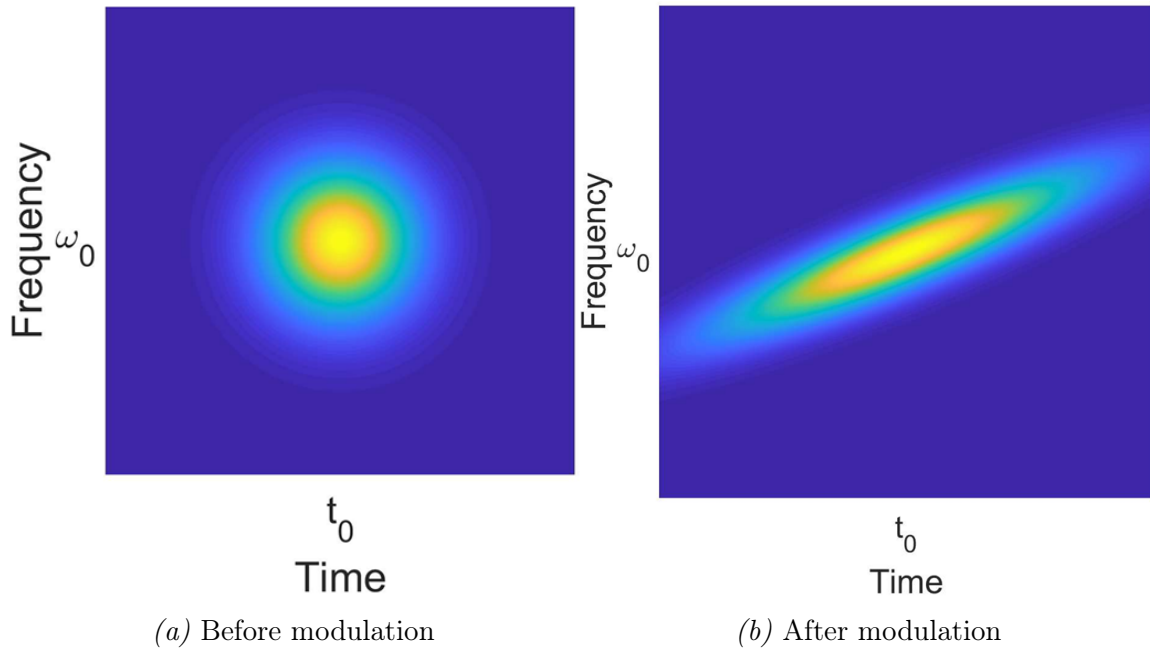


Figure 3.4. The effect of a quadratic spectral phase on the Wigner of a Gaussian temporal mode. (a) displays the initial Gaussian Wigner function of the mode prior to phase modulation. (b) After the quadratic spectral phase modulation the Gaussian is sheared in the direction of the temporal axis by a factor proportional to $\Phi^{(2)}$. From the shearing, it is seen that lower frequencies arrive at a time earlier than higher frequencies.

This chirping effect of the quadratic spectral phase has a useful application in the form of a time-of-flight spectrometer. To see this more clearly we return to the case of a general temporal mode in Eq. (3.11). We can write the output temporal

amplitude in another way by using the convolution, this is written as

$$u_{out}(t) = \frac{e^{-it^2/(2\Phi^{(2)})}}{\sqrt{-2\pi i\Phi^{(2)}}} \int u_{in}(\tau) e^{-i\tau^2/(2\Phi^{(2)})} e^{-i\tau(t/\Phi^{(2)})} d\tau. \quad (3.23)$$

This equation can be simplified by making an approximation. If $\sqrt{\Phi^{(2)}}$ is large compared to the temporal duration of the mode, $\sqrt{\Phi^{(2)}} \gg T_p$, then the quadratic phase term $e^{-i\tau^2/(2\Phi^{(2)})}$ inside the integral will be negligible. So in the regime of this approximation the temporal amplitude is

$$u_{out}(t) \approx \frac{e^{-it^2/(2\Phi^{(2)})}}{\sqrt{-2\pi i\Phi^{(2)}}} \int u_{in}(\tau) e^{-i\tau(t/\Phi^{(2)})} d\tau = \frac{e^{-it^2/(2\Phi^{(2)})}}{\sqrt{-2\pi i\Phi^{(2)}}} \tilde{u}_{in}(t/\Phi^{(2)}). \quad (3.24)$$

Aside from a phase factor, this has the form of the spectral amplitude of the mode where the frequency ω is replaced with $t/\Phi^{(2)}$.

The extra phase factor vanishes when we look at the temporal intensity, which is

$$I_{out}(t) \approx \frac{1}{2\pi|\Phi^{(2)}|} \tilde{I}_{in}(t/\Phi^{(2)}). \quad (3.25)$$

So after a quadratic spectral phase modulation the output temporal intensity is a replica of the original spectrum mapped to time with a scaling factor $1/\Phi^{(2)}$. Then by measuring the intensity as a function of time, using a fast detector, we can measure the spectrum of the unmodulated temporal mode. This technique, known as the dispersive Fourier transform (DFT), can be used to perform single-shot measurements on the spectra of classical optical pulses [God13].

This also has application to the case of single-photon spectrometry. The general approach to measuring the spectrum of a pulse is to use spectrometers that use angular dispersion to map spectral components across spatial modes which can be measured using an array of detectors. This approach has downsides in the case of measuring at the single-photon level due to the need for a large array of single-photon detectors. On the other hand, by using the DFT, only one single-photon

detector is required. Another benefit of this approach is the ability to make high resolution measurements, depending on the amount of spectral dispersion. This technique has been used previously to measure spectra at the single-photon level down to 55 pm resolution [Dav+17].

We have shown that a quadratic spectral phase modulation is useful in controlling the temporal width of a mode, as well the usefulness of frequency-to-time mapping. Quadratic spectral phase is readily available in many materials in the form of their group delay dispersion (GDD) properties. Many elements used in optics have GDD to some degree. One of the most useful sources is optical fiber, which for a desired amount of GDD can be cut to the required length. Another source is from a chirped fiber Bragg grating (CFBG), which can provide a large amount of GDD with relatively low time delay.

Both linear and quadratic spectral phase modulations are useful tools for controlling and manipulating the temporal modes. Of course, higher order phase modulations are possible and each will have an effect on the mode. However, for now we stop at the quadratic phase. As has been demonstrated the modulation by a spectral phase leaves the spectral intensity unchanged, but affects the amplitude of the mode in the time domain. Due to the symmetry between frequency in time this suggests there are equivalent effects due to temporal phase modulation, which we shall describe next.

3.2 Temporal Phase

Linear Temporal Phase

As before in the case of spectral phase modulation, we start by looking at a linear temporal phase. We choose a phase of the form

$$\phi(t) = \alpha t \tag{3.26}$$

Where α is a constant coefficient. This is used to modulate a mode with a temporal amplitude $u_{in}(t)$ and a spectral amplitude $\tilde{u}_{in}(\omega)$. The output temporal amplitude

$$u_{out}(t) = u_{in}(t)e^{i\alpha t}, \tag{3.27}$$

which is simply the original temporal amplitude multiplied by the temporal phase factor, which has no effect on the temporal intensity, which is similar to the case of spectral phase, except we are now treating to Fourier conjugate. The effect of linear temporal phase does not change the temporal amplitude, and thus the temporal intensity. However, there may be changes to the spectral amplitude, which can be found by using the Fourier transform

$$\tilde{u}_{out}(\omega) = \int u_{in}(t)e^{i\alpha t}e^{i\omega t}dt. \tag{3.28}$$

By combining the phase terms inside the integral, this is just the Fourier transform of $u_{in}(t)$ where the kernel has been modified to $e^{i(\omega+\alpha)t}$. Then we find that the output spectral amplitude has been modified to

$$\tilde{u}_{out}(\omega) = \tilde{u}_{in}(\omega + \alpha) \tag{3.29}$$

Thus the effect of applying a linear temporal phase modulation is a shift in frequency of the mode from ω to $\omega - \alpha$, where α is the slope of the linear temporal

phase. This is similar to the time delay caused by a linear spectral phase, but now we have swapped the domains.

To visualize this frequency shift we again focus on the example of a Gaussian mode. Consider a temporal mode with a Gaussian temporal amplitude Eq. (3.13), leading to output temporal amplitude

$$u_{out}(t) = \frac{1}{\sqrt{T}\sqrt{\pi}} e^{-t^2/(2T^2)} e^{i\alpha t}. \quad (3.30)$$

Then in the frequency domain we see that the resulting spectral amplitude becomes

$$\tilde{u}_{out}(\omega) = \sqrt{2T}\sqrt{\pi} e^{-(\omega+\alpha)^2 T^2/2}. \quad (3.31)$$

So as in the case of a general mode, the Gaussian is shifted by a frequency α . This frequency shift due to a linear temporal phase modulation on a Gaussian mode is shown in Fig. 3.5. This looks nearly identical to the effect of a linear spectral phase, except the domains are switched, showing the symmetry between the two.

In the Wigner function representation, the initial mode has the Wigner function

$$W_{in}(t, \omega) = \frac{1}{(2\pi)^2} \int \tilde{u}(\omega + \Omega/2) \tilde{u}^*(\omega - \Omega/2) e^{i\Omega t} d\Omega. \quad (3.32)$$

Then after a linear temporal phase modulation the output Wigner function is

$$W_{out}(t, \omega) = \frac{1}{(2\pi)^2} \int \tilde{u}(\omega + \alpha + \Omega/2) \tilde{u}^*(\omega + \alpha - \Omega/2) e^{i\Omega t} d\Omega = W_{in}(t, \omega + \alpha). \quad (3.33)$$

Similar to what we saw in the case of the spectral phase, the Wigner function is shifted by a frequency α . This transformation is equivalent to a translation along the frequency axis of a distance α . This effect of a linear temporal phase modulation on the Wigner function for a Gaussian pulse is depicted in Fig. 3.6, showing

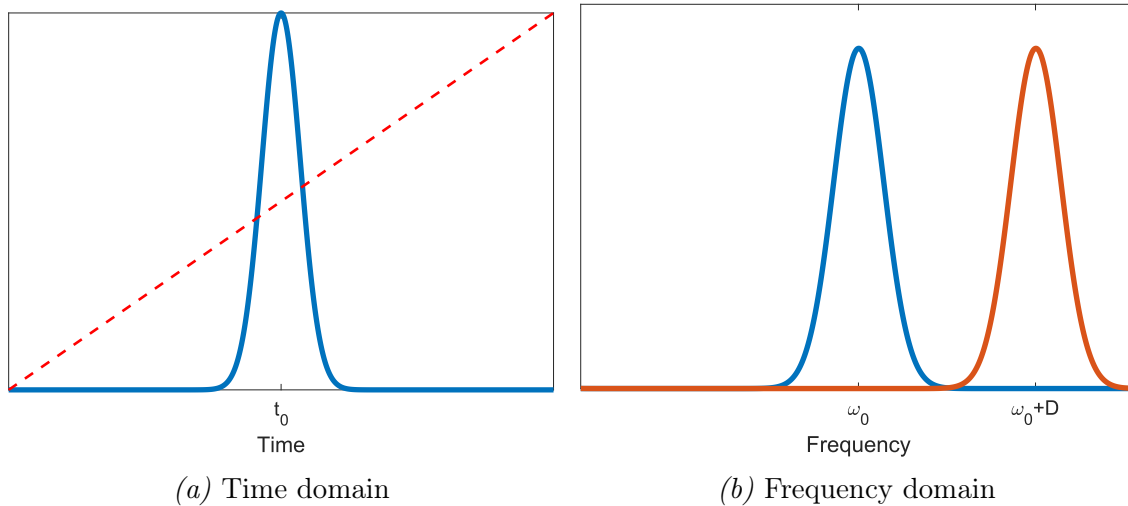


Figure 3.5. The effect of a linear temporal phase on a temporal mode. Using Gaussian mode as an example. (a) displays the Gaussian temporal profile (blue) along with a linear temporal phase (red dashed line). (b) In the frequency domain the original temporal profile is shown in blue. The spectral profile of the modulated mode, in red, is shifted by a frequency D .

the frequency shift as a displacement of the Wigner function along the frequency axis.

The ability for linear temporal phase modulation to shift the frequency of light is an important step toward controlling and manipulating the spectrum of a temporal mode. Since phase modulation is a unitary transformation on the temporal modes, it can be used in quantum applications where low loss mode transformation is essential to preserve the quantum nature of light. Linear temporal phase modulation has been used previously to shift the frequency of single photons [Wri+17; Zhu+22], and has been used as part of a spectral shearing interferometer to characterize single-photon pulses [Dav+18].

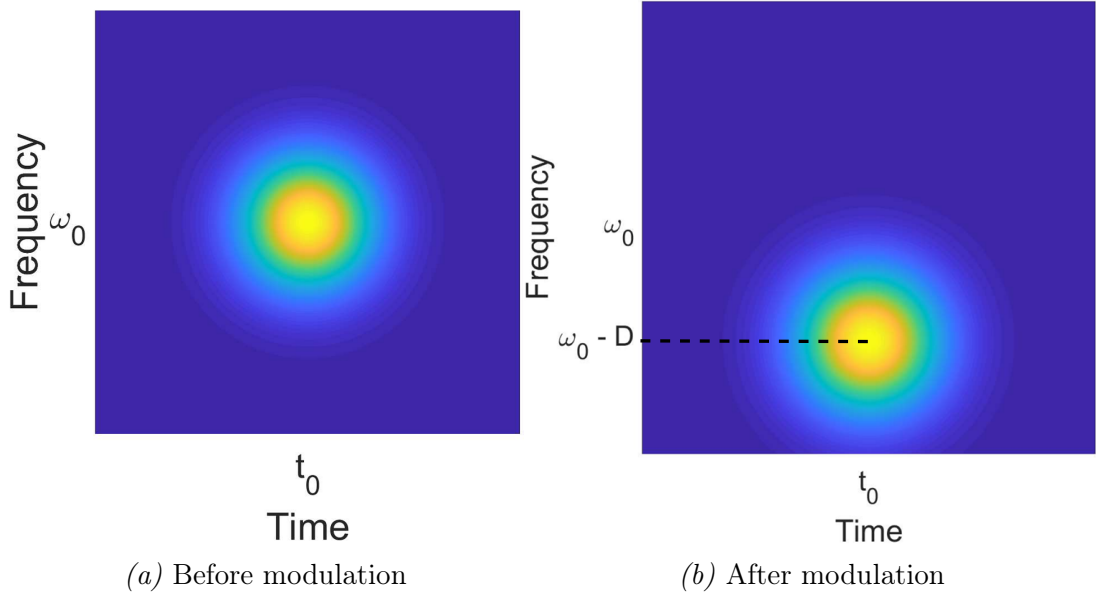


Figure 3.6. The effect of a linear temporal phase on the Wigner of a Gaussian temporal mode. (a) displays the initial Gaussian Wigner function of the mode prior to phase modulation. (b) After the linear temporal phase modulation the Gaussian is shifted along the frequency axis by a time C .

Quadratic Temporal Phase

To complete our discussion of simple phases that can be applied to pulses, we also want to look at the effects of a quadratic temporal phase modulation on the temporal modes. For this purpose we consider the quadratic temporal phase

$$\phi(t) = Kt^2/2, \tag{3.34}$$

where K is a constant coefficient that defines the curvature of the phase. This phase is applied to a mode with a temporal amplitude $u_{in}(t)$, and the output is

$$u_{out}(t) = u_{in}(t)e^{iKt^2/2}. \tag{3.35}$$

We see once again that a temporal phase modulation does not affect the temporal intensity. However, in the frequency domain the spectral amplitude becomes

$$\tilde{u}_{out}(\omega) = \int u_{in}(t)e^{iKt^2/2}e^{i\omega t}dt. \quad (3.36)$$

As we did with the spectral phase, we can rewrite this Fourier transform as a convolution of the individual Fourier transforms of $u_{in}(t)$ and $e^{iKt^2/2}$

$$\tilde{u}_{out}(\omega) = \sqrt{\frac{2\pi}{iK}} \int \tilde{u}_{in}(\Omega)e^{\frac{i(\Omega-\omega)^2}{2K}}d\Omega = \sqrt{\frac{2\pi}{iK}}e^{i\omega^2/(2K)} \int \tilde{u}_{in}(\Omega)e^{i\Omega^2/(2K)}e^{-i\omega\Omega/K}d\Omega. \quad (3.37)$$

If the curvature of the quadratic phase, K , is large compared to the bandwidth of the pulse, $K \gg 1/T^2$, where the bandwidth is taken as $1/T$, then the quadratic phase inside the integral is negligible and the remaining integral is the inverse Fourier transform of $\tilde{u}_{in}(\omega)$. Thus we replace the argument of the inverse Fourier transform $t \rightarrow \omega/K$. In this regime the spectral amplitude will be

$$\tilde{u}_{out}(\omega) \approx \sqrt{\frac{2\pi}{iK}}e^{i\omega^2/(2K)}u_{in}(\omega/K), \quad (3.38)$$

and the spectral intensity is

$$\tilde{I}_{out}(\omega) = \frac{2\pi}{|K|}I_{in}(\omega/K). \quad (3.39)$$

So a quadratic temporal phase maps time to frequency in a way that is similar to the frequency-to-time mapping effect of a quadratic spectral phase.

We again consider a Gaussian temporal mode that has the spectral envelope

$$\tilde{u}_{in}(\omega) = \sqrt{2T\sqrt{\pi}}e^{-\omega^2T^2/2} \quad (3.40)$$

and a temporal envelope of

$$u_{in}(t) = \frac{1}{\sqrt{T\sqrt{\pi}}}e^{-t^2/(2T^2)}, \quad (3.41)$$

where $1/T$ is the spectral bandwidth and T is temporal duration of the pulse. After applying the quadratic temporal phase, the duration of the pulse is unchanged, but the spectral amplitude of this mode becomes

$$\tilde{u}_{out}(\omega) = \sqrt{\frac{2T\sqrt{\pi}}{1 - iKT^2}} e^{-\omega^2 T^2 / [2(1 - iKT^2)]}. \quad (3.42)$$

This modulated spectrum has a spectral width of

$$\Delta\omega_{out} = \sqrt{[1 + (KT^2)^2]/T^2}. \quad (3.43)$$

So similar to the case of the spectral quadratic phase, a temporal quadratic phase expands the spectral width by an amount related to the initial width and the coefficient of the quadratic phase. This is depicted in Fig. 3.7, where again the effect appears to be identical to that of the quadratic spectral phase in the opposite domains.

We shall also look at the effect of the quadratic temporal phase on the Wigner function of a mode. After this modulation the Wigner function becomes

$$W_{out}(t, \omega) = W_{in}(t, \omega - Kt/2), \quad (3.44)$$

which can be readily seen by noting that the quadratic temporal phase in Eq. (3.34) can be viewed as a time-varying frequency shift $\Delta\omega(t) = -Kt/2$. The Wigner function with quadratic spectral phase undergoes a shearing along the frequency axis by an amount $Kt/2$, while the marginal along the time axis remains the same. This transformation is shown in Fig. 3.8 for a Gaussian mode.

This ability to control the spectral bandwidth of a mode is important for many applications. For instance transferring information between nodes of a quantum network that have different bandwidths this can be used to change the bandwidth of the light travelling between the nodes to be compatible on either end.

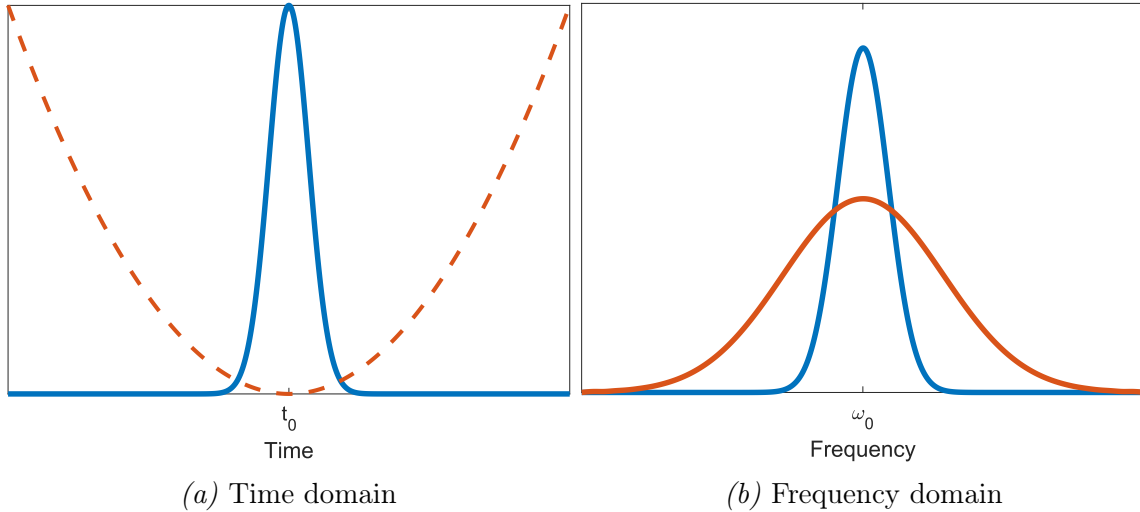


Figure 3.7. The effect of a quadratic temporal phase on a temporal mode. Using Gaussian mode as an example. (a) displays the Gaussian temporal profile (blue) along with a quadratic temporal phase (red dashed line). (b) In the frequency domain the original spectral profile is shown in blue. The spectral profile of the modulated mode, in red, has an expanded bandwidth proportional to the coefficient K .

Time Lens

The quadratic temporal phase modulation is analogous to the quadratic spatial phase modulation of a lens under the space-time analogy in optics. This lends to the idea of a time lens that can be used to perform similar operations. Another important effect that we should consider then is that of a quadratic spectral phase, which is analogous to diffraction in free space.

We have seen that a quadratic spectral phase expands the temporal width of a pulse, and likewise a quadratic temporal phase expands the spectral width of a pulse. Something interesting happens when we use quadratic spectral and temporal phase consecutively. Consider a temporal mode $u(t)$, that undergoes quadratic spectral phase characterized by $\Phi^{(2)}$ followed by quadratic temporal phase charac-

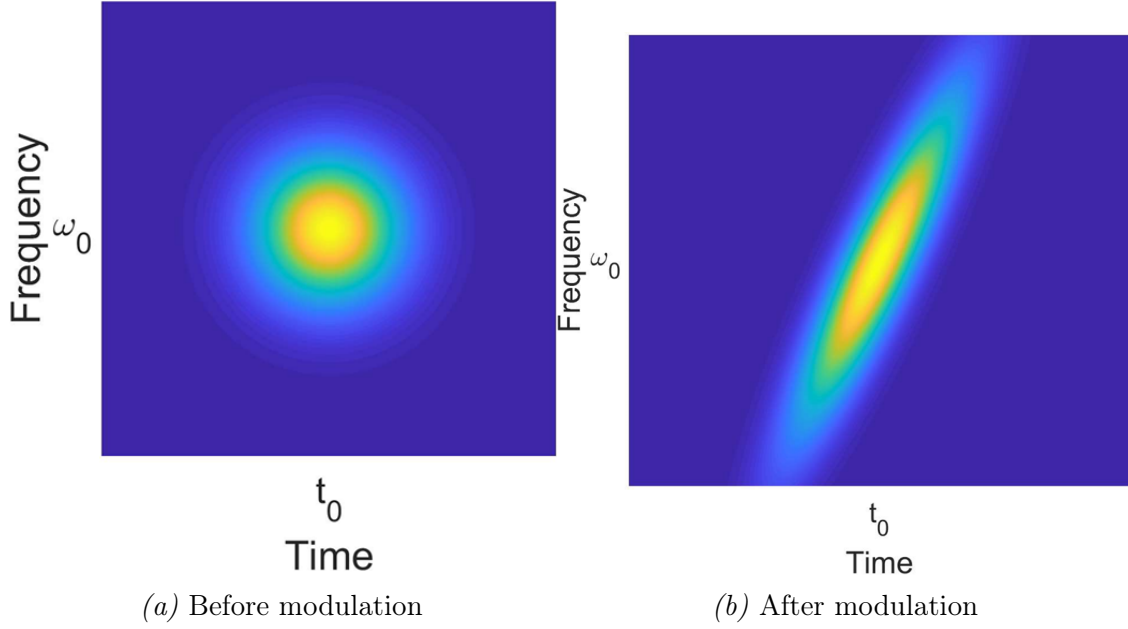


Figure 3.8. The effect of a quadratic temporal phase on the Wigner of a Gaussian temporal mode. (a) displays the initial Gaussian Wigner function of the mode prior to phase modulation. (b) After the quadratic temporal phase modulation the Gaussian is sheared in the direction of the frequency axis by a factor proportional to K . From the shearing, it is seen that points earlier in the temporal profile are shifted to lower frequencies and later points are shifted to higher frequencies.

terized by K . The resulting spectral amplitude will be given by

$$\tilde{u}_{out}(\omega) = \int e^{iKt^2/2} e^{i\omega t} \int e^{i\Phi^{(2)}\Omega^2/2} \tilde{u}(\Omega) e^{-i\omega t} \frac{d\Omega}{2\pi} dt. \quad (3.45)$$

We can change the order of integration, performing the time integral first, and use the following result

$$\int e^{iKt^2/2} e^{i\omega t} e^{-i\omega t} dt = \sqrt{\frac{2\pi}{-iK}} e^{-i(\omega-\Omega)^2/(2K)}, \quad (3.46)$$

to give

$$\tilde{u}_{out}(\omega) = \sqrt{\frac{2\pi}{-iK}} e^{-i\omega^2/(2K)} \int e^{i(\Phi^{(2)}-1/K)\Omega^2/2} e^{-i(\omega/K)\Omega} \tilde{u}(\Omega) \frac{d\Omega}{2\pi}. \quad (3.47)$$

If we choose $K = 1/\Phi^{(2)}$, then the quadratic phase inside the integral vanishes and the integral takes the form of an inverse Fourier transform with time replaced by ω/K

$$\tilde{u}_{out}(\omega) = \sqrt{\frac{2\pi}{-iK}} e^{-i\omega^2/(2K)} \int e^{-i(\omega/K)\Omega} \tilde{u}(\Omega) \frac{d\Omega}{2\pi} = \sqrt{\frac{2\pi}{-iK}} e^{-i\omega^2/(2K)} u(\omega/K). \quad (3.48)$$

Thus we see that aside from a spectral phase and constant amplitude change, the output spectral envelope is a replica of the initial temporal envelope with the frequency axis scaled by $1/K$. The extra phase term vanishes if we look at the spectral intensity $\tilde{I}(\omega) = (2\pi/|K|)I(\omega/K)$. The phase factor can be compensated by the application of an additional quadratic spectral phase characterized by $\Phi^{(2)} = 1/K$. If the input mode is a Gaussian with initial spectral bandwidth $\Delta\omega$ then the output spectral bandwidth will be $\Delta\omega' = K/\Delta\omega$. So unlike the case of a lone temporal phase modulation, where the spectral bandwidth could only be compressed, here the spectral bandwidth can also be magnified using the proper choice of K .

This effect of pairing a quadratic temporal phase with quadratic spectral phases is analogous to the same effect in the spatial domain. A quadratic spectral phase is analogous to free-space propagation, which results in diffraction, and the quadratic temporal phase is analogous to the effect of a lens, so it is called a time lens [SFG13]. A time lens is a powerful tool that enables temporal imaging [KN89] and bandwidth manipulation [Kar+17], among other applications. It is an important technique for controlling and manipulating temporal modes. Finally, note that unlike spatial propagation, the quadratic spectral phase can have either a positive or negative sign, whereas in free space propagation, the field accumulates only positive quadratic phase for the spatial frequency.

3.3 Electro-optic Modulation

While linear and quadratic spectral phase modulation is relatively easy to achieve, either in the form of a delay line or from the use of a *passive*, dispersive element, temporal phase modulation requires the ability to *actively* modulate the phase of the field in time. The temporal phase modulation must occur on the time-scale of the pulse duration, which for our approach is on the order of 1 – 100 ps. To achieve time-varying phase on the time-scale of a few picoseconds, we utilize the electro-optic effect for temporal phase modulation.

Electro-optic phase modulation works on the principle of the Pockels effect, which is a second-order nonlinear electric-field interaction between a low-frequency *electronic* field (voltage) and an optical field, commonly known as an electro-optic effect. In an electro-optic medium the refractive index is a function of an applied low-frequency (typically radio-frequency) electric field. We focus on media where the variation of the refractive index is small, and thus the refractive index can be expanded as a power series in the applied field amplitude

$$n(E) = n_0 + \alpha E + \beta E^2 + \dots \quad (3.49)$$

where α and β are expansion coefficients that depend on the properties of the particular electro-optic medium. To a good approximation, higher-order terms are negligible and can be ignored. In many media, such as lithium niobate, the second order coefficient β is also negligible compared to α . Then the refractive index becomes

$$n(E) \approx n_0 + \alpha E. \quad (3.50)$$

Thus the refractive index varies linearly with the applied electric field. This is known as the Pockels effect. This change in the refractive index modifies the optical path

length of light traveling through the medium. Consider a medium of length L . If the electric field applied across the medium is uniform and constant, the light will accumulate a phase

$$\phi = n(E)k_0L, \quad (3.51)$$

where $k_0 = \omega/c$ is the free space wavenumber. If we define ϕ_0 to be the phase accumulated when there is no applied electric field. We can express this as

$$\phi_n = \phi_0 + \alpha E k_0 L, \quad (3.52)$$

where $\phi(E) = \alpha E k_0 L$ is the additional phase modulation due to the applied electric field. If a uniform and constant electric field is applied across the medium then a pulse of light will acquire a constant phase shift independent of time, but the phase modulation we desire varies with time. To get around this we use traveling wave electro-optic modulators in which the low-frequency electric field in the medium arises from a voltage across two electrodes, which are set up as a transmission line. If the phase velocity of low-frequency voltage through the transmission line is matched with the group velocity of an optical pulse passing through the medium, then a time-varying voltage will apply a corresponding time-varying phase to the optical field.

An electro-optic modulator is characterized by the half-wave voltage, V_π , which voltage required to achieve a π phase shift, i.e. $\alpha E k_0 L = \pi$. In light of this we can rewrite the phase modulation as

$$\phi(t) = \pi \frac{V(t)}{V_\pi}, \quad (3.53)$$

where the time-varying voltage is proportional to the applied low-frequency electric field amplitude. Realistically, V_π will depend on the frequency of the applied voltage. However, most broadband electro-optic modulators (EOMs) are designed to

have sufficiently flat frequency response from near DC up to a specified maximum frequency.

Creating Linear and Quadratic Phases

Electro-optic phase modulation can be used to modulate the temporal phase of a mode. We are particularly interested in linear and quadratic phase modulation. It is impractical to create exactly the phases described in the sections above, but by using approximations and by limiting the temporal modes we use to appropriate bandwidths and temporal durations we can achieve these temporal-phase modulations.

To achieve linear temporal phase modulation for an optical pulse requires a linear phase shift across the duration of the pulse, but the phase applied outside this temporal region does not matter. For temporally long pulses this can pose an issue, as the voltage required to create that phase can become infeasible on the high and low ends. One way around this difficulty is to use a phase that has the form of a sawtooth function with a maximum height of 2π , then the slope is constant across all the peaks and the driving voltage never has to reach higher $2V_{pi}$ while the phase wraps around properly to create a linear phase across the mode. This approach is known as serrodyne frequency modulation.

If the temporal duration of the mode being modulated is small, then we can use various approximations to apply linear temporal phase modulation. The typical method is to drive the EOM with a sinusoidal voltage $V(t) = V_0 \sin(2\pi ft)$ where V_0 is the amplitude of the applied voltage and f is the frequency. This leads to a phase modulation of $\phi(t) = \pi (V_0/V_\pi) \sin(2\pi ft)$. If the pulse duration is short compared to the period of oscillation and aligns with the zero of the sinusoid, we can

expand the resultant phase as a power series around $t = 0$

$$\phi(t) = \pi \frac{V_0}{V_\pi} (2\pi ft - \frac{1}{3}\pi^3 f^3 t^3 + \dots). \quad (3.54)$$

If the pulse we want to modulate is sufficiently short in time, then we need only retain the lowest-order expansion term and arrive at the desired linear phase

$$\phi(t) \approx \frac{2V_0}{V_\pi} \pi^2 ft. \quad (3.55)$$

So the pulsed mode is modulated with a linear temporal phase that has a slope of $(2V_0/V_\pi) \pi^2 f$. The slope of the linear phase modulation can therefore be controlled by changing the amplitude of the driving signal V_0 , or its frequency f . Outside of the region in which this approximation holds there will be variation in the phase compared to the desired linear phase, due to the second order and higher order terms. To make sure that the mode is modulated with a linear phase with small error, we can define an "aperture" for the applied sinusoidal phase in which the mode should be contained. The phase shift expansion in Eq. (3.54) can be rewritten as

$$\phi(t) = \frac{V_0}{V_\pi} 2\pi^2 ft (1 - \frac{\pi^2}{6} f^2 t^2 + \dots). \quad (3.56)$$

Suppose we decide that the aperture is defined as the maximum width at which the variation from a linear phase is limited to 1%. Then the aperture width T will correspond to

$$\frac{\pi^2}{6} f^2 T^2 = 0.01, \quad (3.57)$$

which implies $T = \sqrt{0.06}/(\pi f)$. Any mode that fits within this aperture will experience a linear phase modulation, within the 1% variation. For example if the driving signal has a frequency of $f = 20$ GHz then the aperture will be $T = 3.9$ ps and any modes with temporal duration smaller than 3.9 ps will be linearly modulated to within the stated error.

A similar approach can be taken to achieve a linear phase modulation from an arbitrary driving signal. Any approximately linear section of the signal can be used for modes of sufficiently short duration. In this case there is no analytic method to define the aperture in which the linear approximation holds, but it can be determined if the phase is known by measuring the deviation from a linear fit. Note that if the duration of a mode is small compared to the temporal variation in the applied phase, then any point in the signal will cause an approximately a linear phase modulation.

A quadratic temporal phase modulation can be achieved in an analogous manner. Consider a phase modulation in the form of a cosine function of frequency f

$$\phi(t) = \pi \frac{V_0}{V_\pi} \cos(2\pi ft). \quad (3.58)$$

This too can be expanded in a power series around $t = 0$ to give

$$\phi(t) = \pi \frac{V_0}{V_\pi} \left(1 - \frac{1}{2}(2\pi ft)^2 + \frac{1}{24}(2\pi ft)^4 - \dots \right) \quad (3.59)$$

If the temporal duration of the mode being modulated is small compared to the period of the phase then the third and higher order terms can be ignored and the phase is approximately

$$\phi(t) \approx \pi \frac{V_0}{V_\pi} \left(1 - \frac{1}{2}(2\pi ft)^2 \right). \quad (3.60)$$

So if the duration of the mode is small enough then the phase is approximately quadratic, with an additional constant phase of $\pi V_0/V_\pi$. So the mode is modulated with a quadratic phase with a strength that depends on V_0 and f . But if the duration of the mode is larger then the higher order terms will cause a variation in the phase. The phase expansion in Eq. (3.59) can be rewritten as

$$\phi(t) = \pi \frac{V_0}{V_\pi} - \frac{\pi V_0}{2V_\pi} (2\pi ft)^2 \left(1 - \frac{1}{12}(2\pi ft)^2 - \dots \right) \quad (3.61)$$

As in the case of the linear phase we can define an aperture T as the maximum width at which the variation from a quadratic phase is limited to 1%. Then the aperture T will correspond to

$$\frac{\pi^2}{3} f^2 T^2 = 0.01, \quad (3.62)$$

which implies $T = \sqrt{0.03}/(\pi f)$. A mode of any width smaller than the aperture T will be modulated by a phase that is sufficiently close to quadratic. In this case of a quadratic phase calling this an aperture is even more appropriate, since this is the temporal analogue of a lens, and thus we call it a time lens. Along with restricting the width of modes that can be modulated, this also restricts the bandwidth of the possible modes. As in the case of the linear phase, one can extend the aperture of this time lens by wrapping the phase around at 2π , analogous to a fresnel lens. The possibility of extending the aperture this way has been demonstrated [Soś+23]

A time lens can also be created by using the peaks of any oscillating driving signal, each of which can have different curvatures and apertures.

With the ability to create the linear and quadratic phase modulations in hand, we are able to demonstrate their effects in the lab.

3.4 Measuring the frequency shift

First we shall demonstrate the ability of a linear temporal phase modulation to shift the frequency of a mode. This is created using an amplified signal from the impulse response of a fast photodiode to drive an electro-optic modulator.

The experimental setup for measuring the frequency shift is shown in Fig. 3.9. We generate a train of 100 fs pulses at a repetition rate of 80 MHz, with a central wavelength of 830 nm by using a Ti:Sapph laser. A polarizing beam-splitter (PBS) splits the pulses and directs them along two different paths, a half-wave plate

is used in front of the PBS to control the amount of power going into each path. One path, which we call the probe path, is sent through another set of wave-plates to control the polarization. The pulse probe is spectrally filtered using a 0.5 nm bandpass filter centered at a wavelength of 830 nm, this makes it easier to get a more precise measurement of the central wavelength of the pulse and how much it shifts. The probe then passes through an EOSPACE Electro-optic phase modulator (EOM) which has a 20 GHz bandwidth and a V_π of 1.9 V. The optical output of the EOM is measured on a Horiba iHR spectrometer with a 0.03 nm spectral resolution.

The other path, which we call the signal path, takes the pulse through a delay line. The delay line is made up of a half meter long rail, with mirrors placed along a motorized stage that offers sub-picosecond resolution. We collect the signal pulse in a fiber and detect it using a Thorlabs DX25CF photodiode (PD) with a stated bandwidth of $DC - 25$ GHz and a 15 ps impulse response. The output radio-frequency (RF) electronic signal from the photodiode is amplified using an RF amplifier (Amp) which has a bandwidth of 30 GHz. The resulting amplified RF signal is used to drive the EOM.

The RF output from the EOM is monitored on an oscilloscope. We use this to adjust the timing of the RF signal so that it arrives at the EOM at the same time as the probe pulse. This is done coarsely by moving the translation stage along the delay line rail to the necessary point. The two paths are made with equivalent length so that the RF driving signal is derived from the same pulse in the pulse train as the probe pulse.

We scan through the length of the translation stage using the motor until we observe a shift in the central wavelength of the spectrum. The EOM is birefringent, and only modulates one polarization with very little crosstalk. Using the wave-

plates in the probe path, we adjust the polarization to maximize the shift in the central wavelength so that the probe has the optimal polarization.

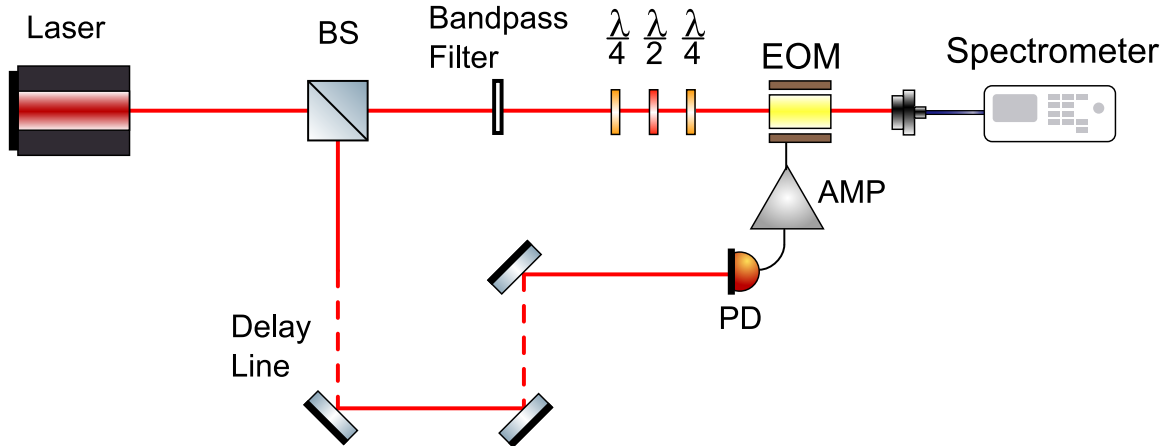


Figure 3.9. The setup for measuring the frequency shift. The pulse originates from a Ti:Saph laser. It is split into two paths. In one the probe path the polarization is controlled by wave plates, and a spectral filter is used so that the frequency shift is more visible. The other path has a delay line and a fast photodiode, the resulting signal is amplified and used as the driving signal for the EOM. An electronic output from the EOM is monitored on the Oscilloscope to observe the time of arrival. The output of the EOM is measured on a spectrometer.

We adjust the delay line so that the probe pulse arrives just before the RF signal. We then use the translation stage to move the RF signal forward at 1.68 ps increments, measuring the output spectrum of the probe pulse at each point. Each measured spectrum is fit to a Gaussian waveform from which we determine the central wavelength of the pulse. The central frequency is then found using $\omega = 2\pi c/\lambda_0$ where λ_0 is the initial wavelength of the unmodulated probe, which is found by turning the RF signal off. By doing this we build up a profile of the frequency shift across a portion of the RF signal.

The results are shown in Fig. 3.10, for measurements with an RF driving signal created by an optical pulse of 200 μW optical power. The results are normalized to the initial central frequency of the probe pulse, which is measured to be

829.4 nm. We see that as probe pulse is scanned through the RF signal, the frequency shifts between higher and lower frequencies in an oscillating fashion. The largest frequency shift is 0.69 THz in the positive direction and -0.79 THz in the negative direction.

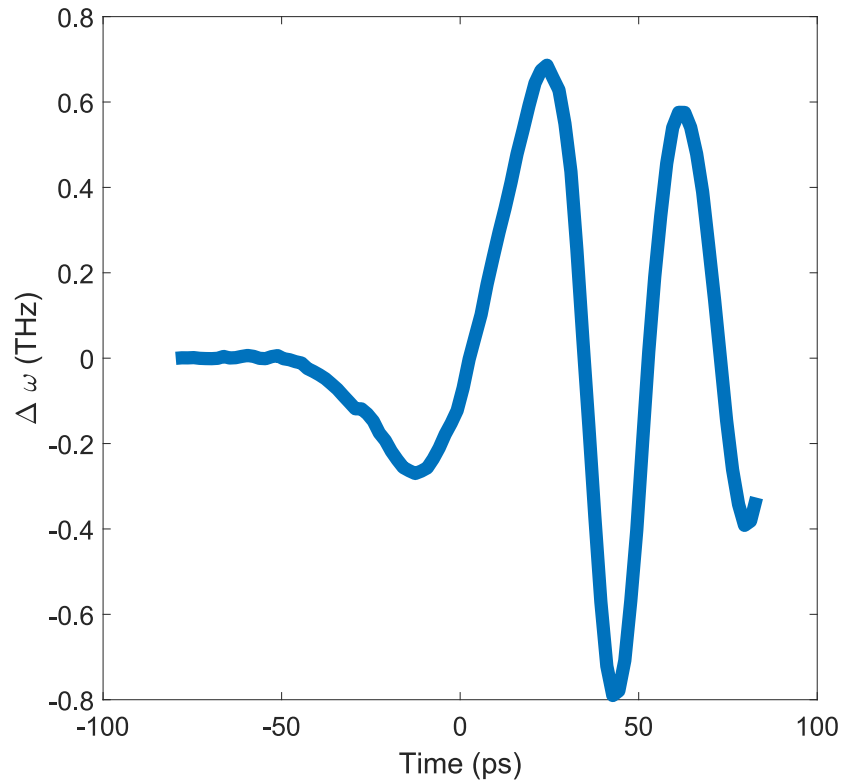


Figure 3.10. The linear temporal phase shifts the central frequency of the pulse in proportion to its slope. There several positive and negative peaks, implying that the phase oscillates. The maximum frequency shift is 0.69 THz and -0.79 THz.

Reconstructing the temporal phase

If the temporal width of the probe pulse is small compared to the period of oscillation in the frequency shift. Then as shown above in Eq. 3.31, the frequency shift will be equivalent to the slope of the slope of the temporal phase modulation

at the point being measured. Then Fig. 3.10 is equivalent to a plot of the slope of the of the phase modulation. Using this fact, we can integrate over the frequency shift to reconstruct the phase modulation. By doing so, we find the phase modulation profile in shown in Fig. 3.11 We see that the reconstructed phase has an

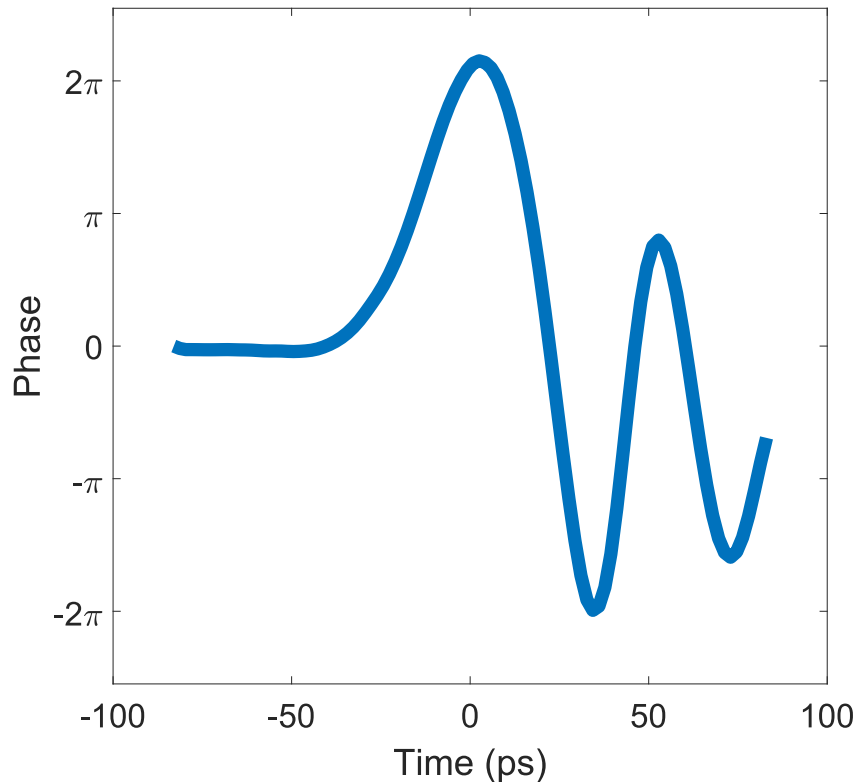


Figure 3.11. The reconstructed temporal phase

initial initial peak, followed by subsequent oscillating peaks of decaying amplitude. The peaks of the phase modulation line up with the maxima and minima of the of the frequency shift. The initial peak is the widest, while the following peaks have a smaller width.

The phase modulation is proportional to the voltage applied to the EOM. If we assume that the half-wave voltage V_π of 1.9 V specified at 1 GHz is sufficiently

flat up to 23 GHz then the phase modulation should be linearly proportional to the applied voltage. In this case the peak phase of 6.76 radians would correspond to a peak voltage of 4.09 V.

We can compare this reconstructed phase to the impulse response given in the specifications of the photodiode shown in Fig. 3.12. In this impulse response the initial peak is prominent compared to the subsequent peaks. By inspection, the time difference between the first and second peak is approximately 40 ps; which makes sense for a photodiode with a bandwidth of 23 GHz. By comparison the reconstructed phase has an initial peak that is less prominent in than the specified impulse response. Additionally, the time difference between the first two peaks is 50.3 ps, longer than that of the specified impulse response. The discrepancy between the reconstructed phase and the photodiode impulse response may be explained by the temporal width of the probe pulse not being sufficiently short to be considered an impulse with respect to the speed of the photodiode. It also could be the result of the frequency responses of the amplifier and the EOM filtering out the higher frequency components from the photodiode. The EOM has a specified bandwidth of up to 20 GHz operation, which is smaller than the 23 GHz bandwidth of the photodiode. Considering this, we note that 20 GHz sinusoidal wave has a period of 50 ps, which is near the time difference between the first to peaks of the reconstructed phase.

As mentioned before, like a sinusoidal wave, an oscillating signal may have regions at the extrema in which the phase is approximately quadratic. They can therefore be useful in applications such as bandwidth compression or use as a time lens. We can investigate this possibility for each of the peaks in the reconstructed phase. By fitting a polynomial curve to each peak we can calculate the approximate quadratic coefficient of the phase in the region of that peak. Considering the

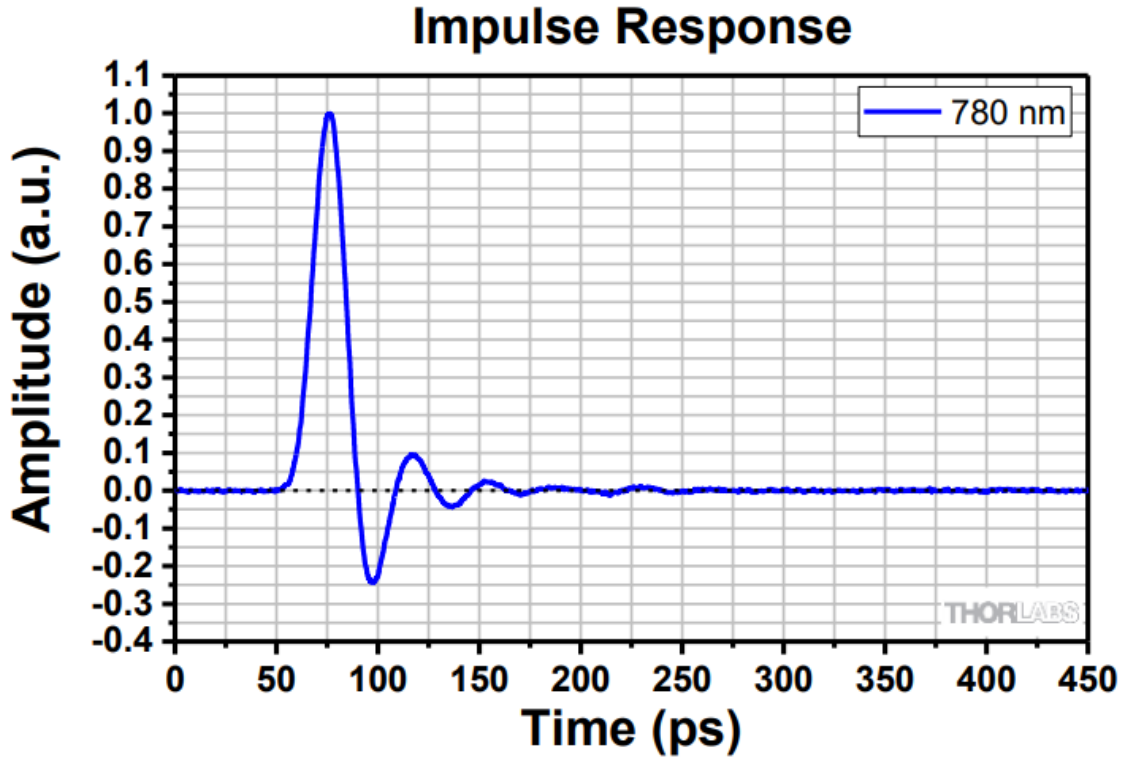


Figure 3.12. The impulse response of the Thorlabs DX25CF photodiode, given in the specifications.

case of a time lens, the quadratic coefficient is the time lens curvature. There phase modulation profile may include higher order components beyond the quadratic modulation, so we choose to use a 4th-order polynomial curve to fit the peaks. The polynomial fit to the first peak of the reconstructed phase is shown in Fig. 3.13.

The quadratic component for this peak is $\Phi_t^{(2)} = -0.016 \text{ THz}^2$, this is the effective time lens curvature. By comparing the quadratic coefficient with the next highest order coefficient we can determine an effective aperture over which this peak could be used as a time lens. The third-order coefficient for this peak is $\Phi_t^{(3)} = 2.1 * 10^{-4} \text{ THz}^3$. If we define the aperture to be the width at which the third-order component to the phase is 1% of the quadratic component, we find the aperture T using the inequality

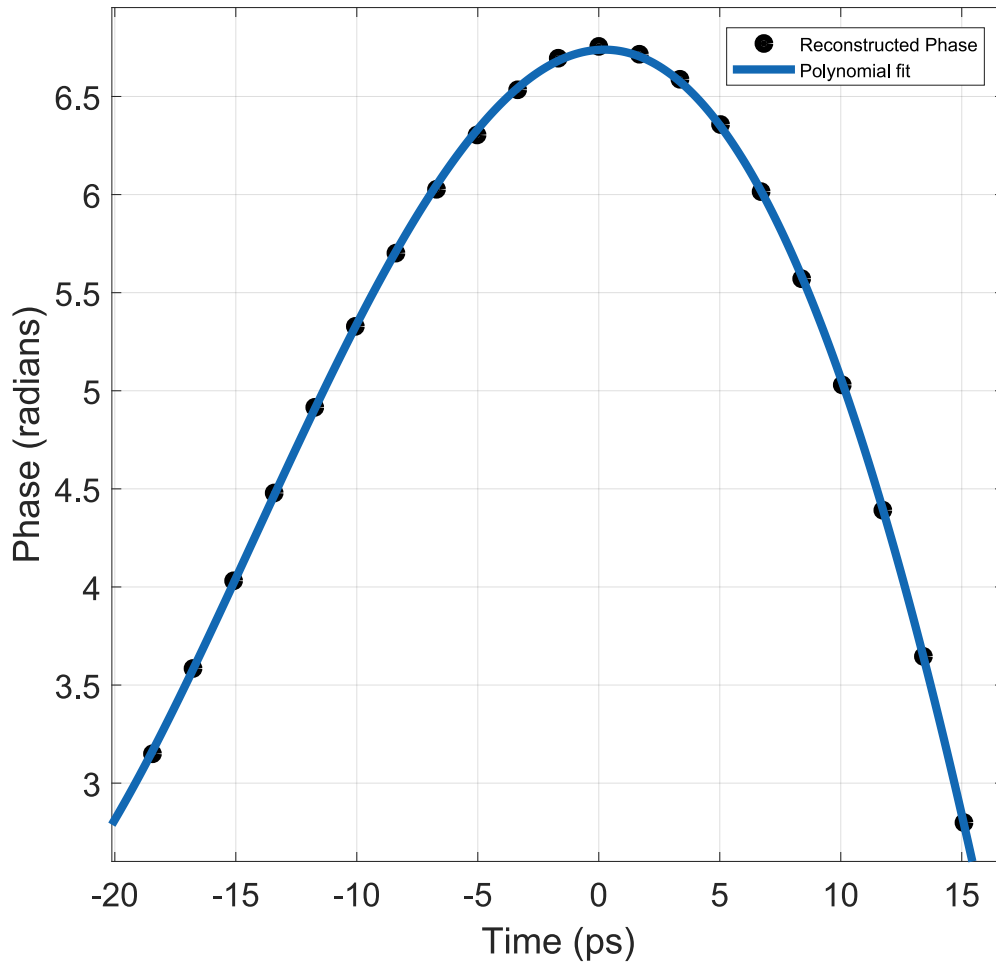


Figure 3.13. A 4th degree polynomial fit to the first peak of the reconstructed phase.

$$\left| \Phi_t^{(2)} \left(\frac{T}{2} \right)^2 \right| < \left| \frac{1}{100} \Phi_t^{(3)} \left(\frac{T}{2} \right)^3 \right| \quad (3.63)$$

From this we find that the aperture for this first peak is $T = 1.7$ ps, this is the maximum width of a pulse that can be with this time lens before significant errors occur. The equivalent aperture of a sinusoidal wave with a frequency of 20 GHz is 6.2 ps. We can do the same for each of the peaks of the reconstructed phase, and

the results are shown in the Tab. 3.1.

Peak	$\Phi_t^{(2)}$ (THz ²)	$\Phi_t^{(3)}$ (THz ³)	Aperture (ps)
#1	-0.016	$-2.1 * 10^{-4}$	1.7
#2	0.062	$5.1 * 10^{-4}$	2.2
#3	-0.054	$9.1 * 10^{-4}$	1.5
#4	0.040	$-7.3 * 10^{-4}$	1.5

Table 3.1. The quadratic temporal phase coefficient $\Phi_t^{(2)}$ and the third-order phase coefficient $\Phi_t^{(3)}$ for each peak of the reconstructed phase, along with the computed apertures.

Here we see that the second peak has the largest curvature and the widest aperture, making it the best candidate for use as a time lens but restricted to pulses with a width of 2.2 ps. By comparison, the approximately quadratic part of a sinusoidal phase modulation with a frequency of 20 GHz has an aperture of 5.5 ps, which is larger than any of the apertures found in the reconstructed phase.

3.5 Bandwidth Manipulation

Another interesting application of temporal is the ability to manipulate the bandwidth of a pulse, this is another step toward the controlled generation of optical pulses and to enable communication between different systems. Bandwidth manipulation has been achieved using an electro-optic time lens [Kar+17], which uses a quadratic temporal phase modulation to compress or expand the bandwidth of a pulse.

Theory

As we saw in Eq. (3.43), a quadratic temporal phase will expand the spectral width of a Gaussian pulse. If we apply a quadratic phase of curvature K to a Gaus-

sian pulse of spectral width σ_ω then the resulting pulse will have a FWHM of

$$\Delta\omega_{out} = 2\frac{\sigma_\omega^4 + K^2}{\sigma_\omega^2} \quad (3.64)$$

So the bandwidth of the pulse will be expanded proportionally to the square of the phase curvature, regardless of the sign.

We have seen with the concept of a time lens that additional effects occur if the temporal phase modulation is preceded by a quadratic spectral phase. We have seen that if the quadratic spectral phase coefficient $\Phi^{(2)}$ is matched with the temporal phase curvature such that $K = 1/\Phi^{(2)}$ then the spectral width of the mode will be $\sigma_{out,\omega} = K/\sigma_\omega$. So the bandwidth of the mode will be expanded or compressed relative to the amount of curvature.

If the quadratic spectral phase is not matched with the temporal phase curvature then we can still find the effect on the bandwidth. The FWHM of the resulting pulse is:

$$\Delta\omega_{out} = \sqrt{2 \log 2 \left[\left(\frac{2\sigma^2}{1 + \sigma^4\Phi_\omega^{(2)}} \right) + \frac{\left(\frac{2\sigma^4\Phi_\omega^{(2)}}{1 + \sigma^4\Phi_\omega^{(2)}} - 2K \right)^2}{\frac{2\sigma^2}{1 + \sigma^4\Phi_\omega^{(2)}}} \right]} \quad (3.65)$$

In this case the bandwidth is either expanded for negative values of K or compressed for positive values of K .

Measuring the bandwidth

The setup for measuring the bandwidth is show in 3.14, it is similar to that for measuring the frequency shift, but in the path of the probe pulse we add a 56.5 m optical fiber with a $\Phi_\omega^{(2)}$ of 2.26 ps². The dispersion applied by this fiber chirps the pulse, expand it to a temporal width of 7.6 ps in order to better fill the width

of the approximately quadratic peaks of the modulation. We again measure the spectrum using the Horiba spectrometer, with a spectral resolution of 0.03 nm. The delay line is adjusted so that the probe pulse passes through the modulation signal, and we take measurements at a constant time increment. For each measurement, the spectral width is calculated. The bandwidth of the pulse is compared to that when the RF signal driving the EOM is turned off. At each of the peaks, where the phase will be most approximately quadratic, we calculate the phase curvature that would account for this bandwidth and compare it to the reconstructed phase from frequency shifting. We can use the bandwidth measurement and the amount of dispersion introduced by the fiber to estimate what the quadratic component of the temporal phase is at each peak.

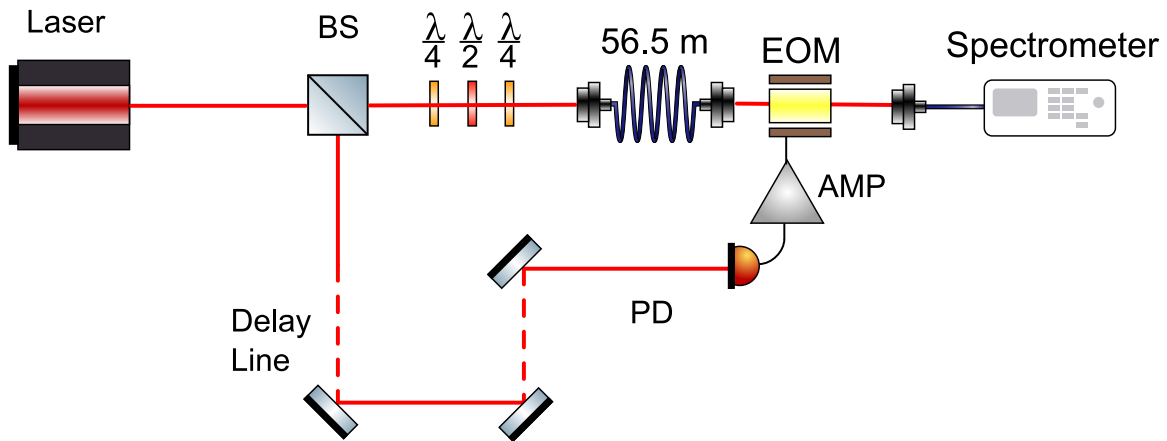


Figure 3.14. The setup for measuring the bandwidth. The pulse originates from a Ti-Saph laser. It is split into two paths. In one the probe path the polarization is controlled by wave plates, and a spectral filter is used so that the frequency shift is more visible. A 56.5 m spool of fiber is used to chirp the pulse. The other path has a delay line and a fast photodiode, the resulting signal is amplified and used as the driving signal for the EOM. An electronic output from the EOM is monitored on the Oscilloscope to observe the time of arrival. The output of the EOM is measured on a spectrometer.

The bandwidth measurement, using a power of 200 μW to create the phase

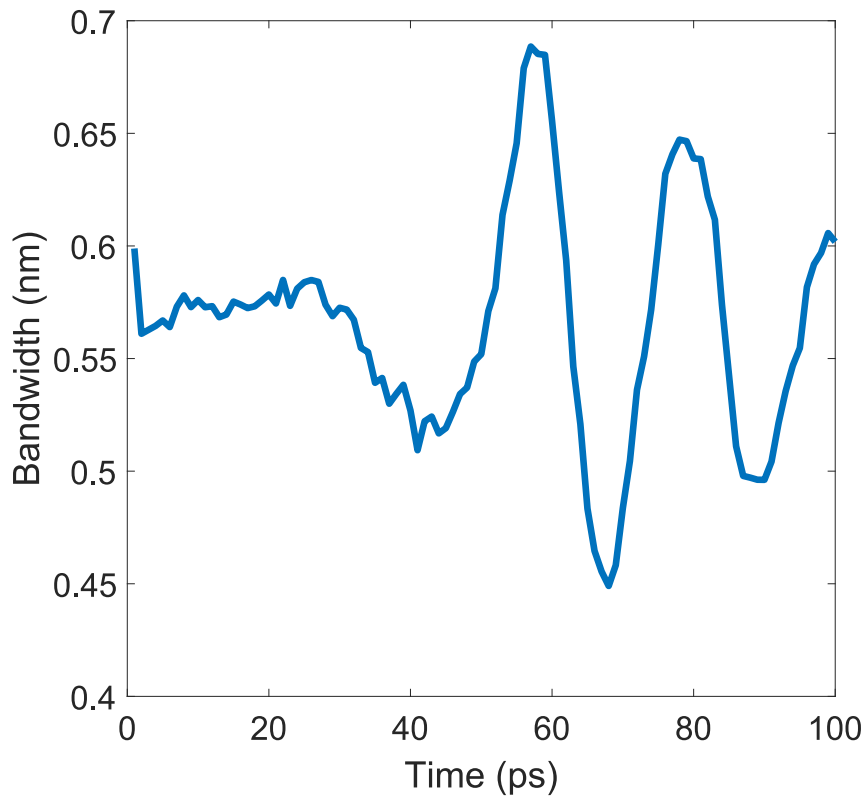


Figure 3.15. The bandwidth shift

modulation driving signal, is shown in Fig. 3.15. We see several oscillating peaks of decreasing amplitude which is to be expected from the reconstructed phase of 3.11. The period of oscillation is consistent with that of the reconstructed phase and the impulse response of the photodiode. The highest peak has a bandwidth of 0.69 nm while the lowest peak has a bandwidth of 0.45 nm, these are both compared to an unmodulated bandwidth of 0.57 nm when the rf signal is turned off. These peaks are the points where the phase modulation is approximately quadratic, at other points there is still an effect on the bandwidth, but they are not determined by the same equation. We can compare the bandwidth compression at the peaks to those by the curvatures at the peaks of the reconstructed phase. Considering the disper-

sion coefficient of a 56.5 m optical fiber is 2.26 ps², we can estimate the time lens curvature K using Eq. (3.65). The bandwidths of each peak, along with their estimated time lens curvatures are listed in Tab. 3.2.

Peak	Bandwidth (nm)	K (THz ²)
#1	0.52	-0.0095
#2	0.69	0.023
#3	0.45	-0.023
#4	0.65	0.016

Table 3.2. The bandwidth for each peak of Fig. 3.15, and the corresponding phase curvature K

Comparing this to the curvature we found using the phase reconstruction from linear temporal phase modulation, we see that they are in the same order of magnitude but otherwise different. Particularly, the second peak has a curvature of 0.023 THz² determined from the bandwidth, whereas the the reconstructed phase has a curvature of 0.062 THz². This is a significant disagreement between the two measurements. There are several possible explanations for this disagreement. A potential explanation for the discrepancy is that we aren't actually measuring the same phase as during the frequency shift measurement, since in adding the dispersive fiber in the probe line we have to adjust the position of the delay line. Any change in the delay line can affect the pulse that is used to generate the RF signal, which it turn may affect the shape of the signal itself.

Another possible source of error is that the pulse is too wide to fit within the aperture. As found from the reconstructed phase the 1% error apertures of each peak are around 2 ps. But the width of a 0.57 nm pulse after 56.5 m of dispersion is 7.3 ps, so there may be more significant error and contribution to the bandwidth from higher order terms.

Another source of error could be from timing jitter in the pulse train of the laser. Since there is a 56.5 m fiber in one arms and not the other, the phase modulation driving signal is not derived from the same probe pulse. So if there is any variation in the repetition rate of the laser this will affect the timing of the phase modulation. Since the measurements are a integration over several pulses, this can affect the final result.

Another possibility is that the polarization is not optimal, in which case the spectral measurement is including a contribution from the unmodulated mode. This would have the effect of causing an apparently smaller change in bandwidth.

3.6 Spectral Interferometry

Both the frequency shift and bandwidth manipulation techniques provide us with a way to characterize a temporal phase modulation by measuring the effect of the linear and quadratic components of the modulation at various points in time in time across the signal, these are both ways of indirectly measuring the phase modulation. Here we introduce another technique, to directly measure the phase modulation, using spectral interferometry. This works by interfering a modulated pulse with an un-modulated reference pulse. The resulting interferogram contains information about the relative spectral phase between the two pulses, but if the pulses are first chirped this will also contain information about the relative temporal phase. We can use this to extract the temporal phase modulation. This technique has previously been used [MK18] to characterize temporal phase modulations. As in both the previous techniques the RF signal that drives the phase modulation is created using a fast photodiode with a pulse picked off from the same source as the probe pulse. This helps with stability and synchronization, as the ar-

rival times between the two pulses will be well correlated as long as they are near to each other in the pulse train.

Theory

To perform a spectral interferometry measurement we interfere a reference pulse $\tilde{u}(\omega)$ with a copy of the pulse modulated a spectral phase $\phi(\omega)$ that we wish to measure. Between the two pulses we add a relative delay t_d , which adds a relative phase $e^{i\omega t_d}$. The measurement of the resulting spectral intensity is, known as the interferogram, is

$$\tilde{I}'(\omega) = 2\tilde{I}(\omega) + 2\tilde{I}(\omega)\cos(\phi(\omega) + \omega t_d) \quad (3.66)$$

Where $\tilde{I}(\omega)$ is the intensity of the original pulse. So the output spectrum has a term that is a copy of the original intensity, which we call the DC term; and a term that oscillates with a frequency proportional to the time delay, which we call the AC term. Due to the AC term the interferogram will have fringes with a period of $2\pi/t_d$, which are modulated by the additional spectral phase $\phi(\omega)$. The AC term can be separated into positive and negative components. In which case the form of the spectral intensity is

$$\tilde{I}'(\omega) = 2\tilde{I}(\omega) + \tilde{I}(\omega)e^{i(\phi(\omega)+\omega t_d)} + \tilde{I}(\omega)e^{-i(\phi(\omega)+\omega t_d)} \quad (3.67)$$

This can be rewritten as

$$\tilde{I}'(\omega) = \tilde{I}^{DC}(\omega) + \tilde{I}^{+AC}(\omega)e^{i\omega t_d} + \tilde{I}^{-AC}(\omega)e^{-i\omega t_d} \quad (3.68)$$

Where $\tilde{I}^{\pm AC}(\omega) = \tilde{I}(\omega)e^{\pm i\phi(\omega)}$. To continue we take the inverse Fourier transform of the interference spectrum. Due to the Fourier shift theorem this becomes

$$I(t) = I^{DC}(t) + I^{+AC}(t + t_d) + I^{-AC}(t - t_d) \quad (3.69)$$

So the inverse Fourier transform has a DC term centered at $t = 0$ and two AC sidebands centered at $t = \pm t_d$. The entire information about the spectral phase is contained in either of these sidebands.

To extract the phase we can filter the inverse Fourier transform to isolate one of the sidebands. By isolating the positive AC term and performing the Fourier transform on it we get

$$\tilde{I}^{+AC}(\omega) = \tilde{I}(\omega)e^{i\phi(\omega)+i\omega t_d} \quad (3.70)$$

By taking the argument we arrive at the phase difference between the modulated pulse and the reference pulse

$$\phi = \phi(\omega) + \omega t_d \quad (3.71)$$

The extra phase difference from the time delay can be subtracted if t_d is known, or it can be subtracted by the argument of a second spectral interferometry measurement taken in the absence of $\phi(\omega)$. Any spectral phase that pulses shared prior to the modulation is filtered out by this process. What we are left with is the phase $\phi(\omega)$ that we wished to measure.

To measure a temporal phase modulation using spectral interferometry, we perform the modulation on a chirped pulse. As we have seen before, applying a large amount of dispersion to a pulse will effectively perform a Fourier transform such that the temporal profile becomes a scaled copy of the initial spectrum. The spectral components are mapped to time, with the instantaneous frequency given by Eq. (3.21). Then a temporal phase modulation on a chirped pulse will also modulate the spectral components. So by measuring the spectral phase using interferometry, and using the appropriate scaling factor, we will find the temporal phase modulation.

Measurement

The setup to measure the phase modulation using spectral interferometer is shown in Fig. 3.16, this is similar to those used for the previous measurements. The driving signal for the EOM is created in the same way as the previous measurements, from the amplified impulse response of the photodiode using $200 \mu\text{W}$ of optical power. In the probe path we use a 500 m fiber, which applies a GDD of $\Phi_{\omega}^{(2)} = 20 \text{ ps}^2$, to chirp the probe pulse before it enters the EOM; so after dispersion the pulse has a temporal FWHM of 277 ps. The polarization of the probe is rotated by 45 degrees so that it is diagonal to the polarization modulated by the EOM. Due to the birefringence of the EOM, the probe is separated in to two orthogonally polarized pulses with a time delay between them. One of these pulses is modulated by the EOM while the other remains unmodulated. This creates the two pulses that we interfere with eachother. The time delay between the pulses caused by the EOM is an appropriate amount for our purposes, so no additional compensation is needed. The output of the EOM is sent through a another waveplate that rotates the polarization by 45 degrees. It then passes through a polarizing beam-splitter which mixes the two pulses and interferes them. The resulting spectral intensity is measured on the spectrometer with an integration time of 100 ms.

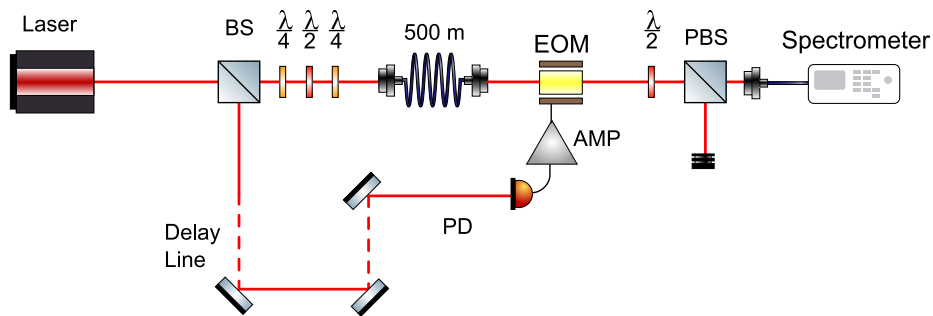


Figure 3.16. The spectral interferometry setup.

The measured interferogram is shown in Fig. 3.17, for the modulated measurement and for a reference unmodulated measurement where the driving signal is turned off. We can see that the interference fringes when are shifted by the phase modulation when the driving signal is turned on, we use this difference to extract the phase modulation. First we take the inverse Fourier transform of the interferogram.

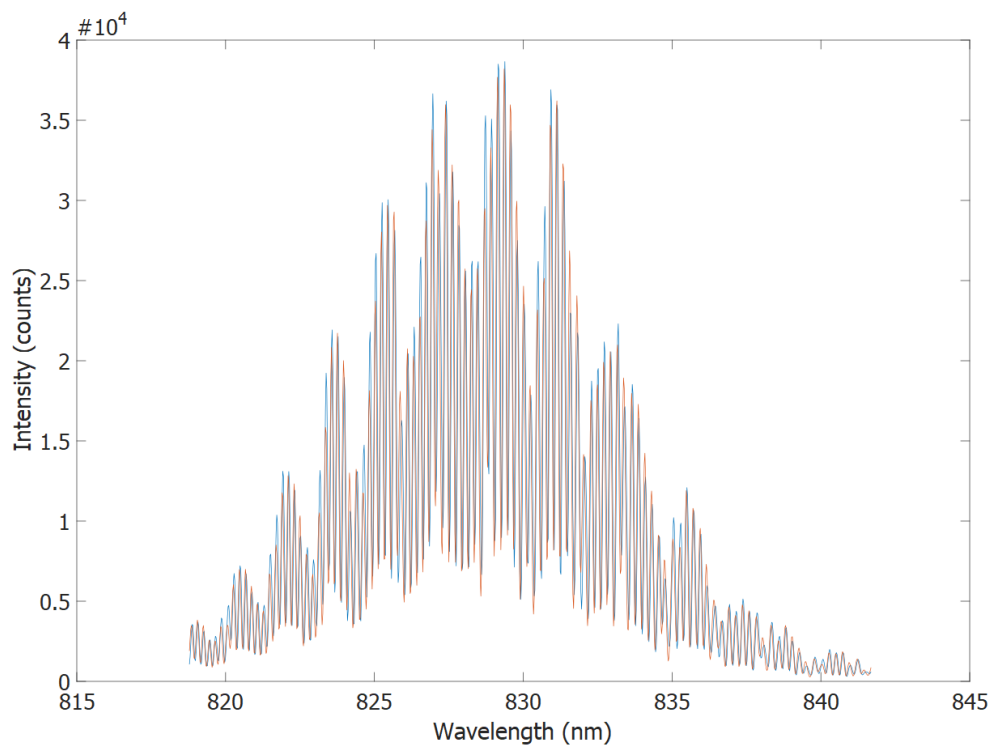


Figure 3.17. The measured spectrum showing interference fringes. The modulated spectrum is in blue, and the unmodulated spectrum is in red. With fringe spacing determined by the temporal delay.

Fig. 3.18 shows the inverse Fourier transform of the spectral intensity for the interferogram when the driving signal is turned on. This shows the DC term and the two AC sidebands. The distance of the AC sidebands from the DC term is determined by the time delay between the polarizations, which comes from the bire-

fringe of the EOM itself. We see that the delay is appropriately large enough that the AC sidebands can be resolved. The side-bands found in the inverse Fourier

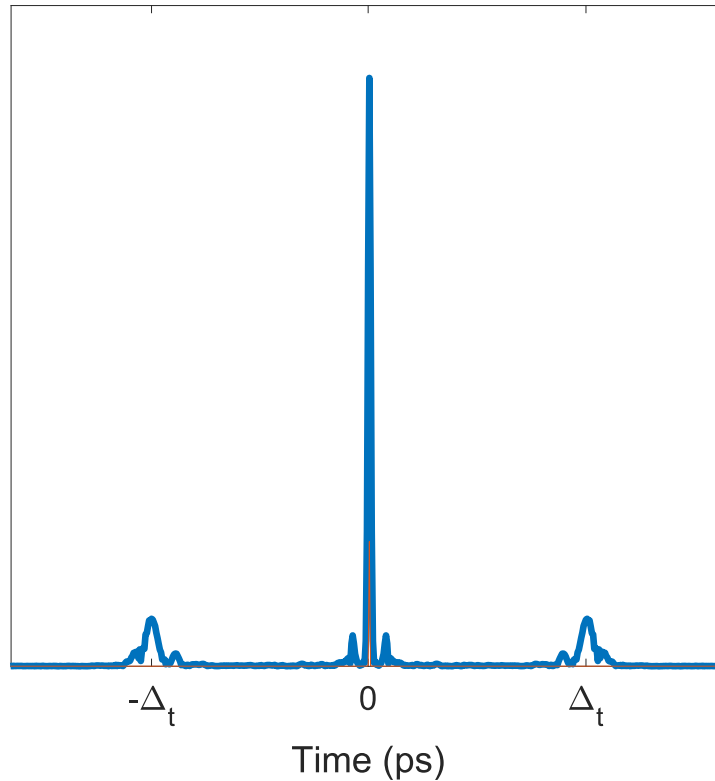


Figure 3.18. The inverse Fourier transform of the interference spectrum. The two side-bands contain the phase information.

transform both contain all the information about the phase difference between the modulated and reference pulse. We pick the positive sideband and isolate it using a Gaussian filter of variable width. We can access the phase information in this sideband by taking the Fourier transform and finding the argument of the result, which will include the phase from the modulator as well as a linear term from the time delay. We do the same process with interferogram where the driving signal is turned off, and subtract that argument to extract the phase modulation. Fig. 3.19 shows

the phase extracted via this process.

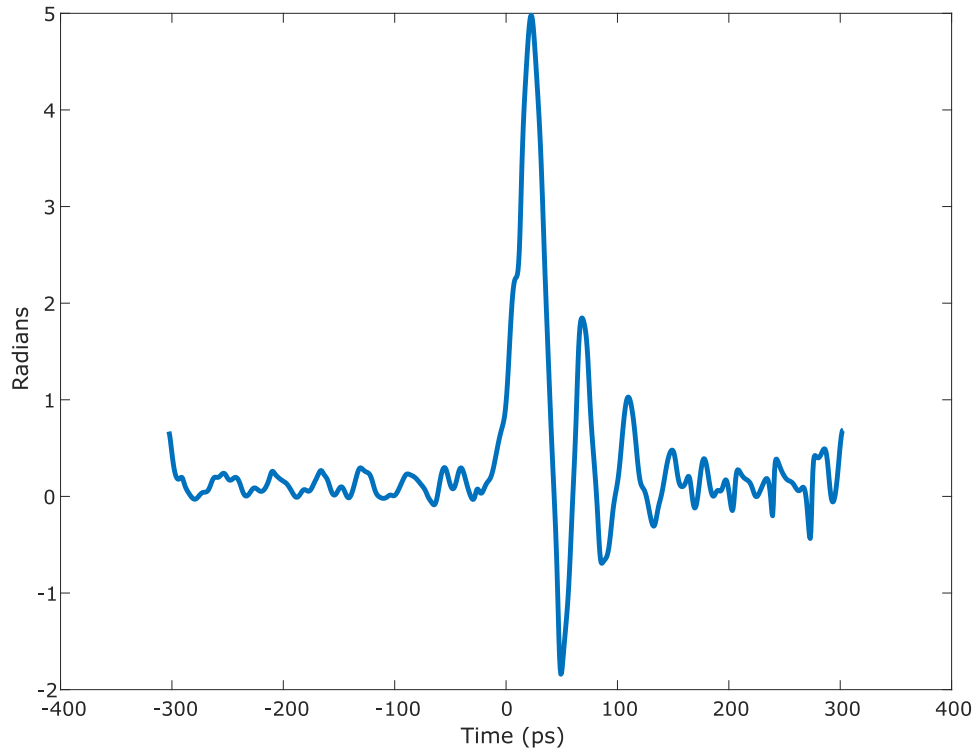


Figure 3.19. The phase measured using spectral interferometry, reconstructed from the fft.

Comparing this phase to the reconstructed phase from frequency shifting, we see that the initial peak is much more prominent with respect to the subsequent peaks. This is more consistent with the proportions of the peaks seen in the impulse response of the photodiode. But the timing between the peaks is consistent with both that from frequency shifting and bandwidth manipulation. This measurement doesn't have the downside of requiring the probe to fit within an aperture, so it doesn't encounter the difficulties found in the frequency shift or bandwidth measurements that wash out the effect of the phase modulation. Also, since the spectrum is measured over a single 100 ms integration time window, this tech-

nique avoids the problem of drift in the central wavelength or bandwidth of the laser pulse over time; a problem which could be encountered in the frequency shift and bandwidth measurements due to the time needed to scan through the phase.

CHAPTER 4

ARBITRARY UNITARY TRANSFORMATIONS

In the previous chapter we showed that temporal and spectral phase modulations have the ability to apply a variety of transformations to control and manipulate many important properties of temporal modes. In this chapter we show how arbitrary unitary transformations on temporal modes can be applied using a series of consecutive phase operations, and propose an experiment that can implement them. We investigate the feasibility of these transformations by simulating them using realistic constraints on the parameters of the phase modulations based on available equipment, and optimize them to find the ideal series of phase modulations able to apply unitary transformations using the fewest resources.

This chapter contains co-authored material previously published in volume 28 of *Optics Express* in December 2020 [Ash+20]. I was the primary contributor to the writing and simulations in this work, with assistance on the theoretical background from co-authors Valérian Thiel, Markus Allgaier, Peru d'Ornellas, Alex O. C. Davis, and Brian J. Smith.

4.1 Theory

The idea to use alternating temporal and spectral phase modulations to implement an arbitrary unitary transformation comes from a theorem proven in Ref. [Sch+00] that any unitary matrix can be decomposed into a sequence of unitary diagonal matrices and Fourier transforms. For any given unitary matrix U the decomposition can be written as:

$$U = D_1 F D_2 F^\dagger \dots D_n F^\dagger \tag{4.1}$$

Where D_n is a diagonal unitary matrix, F is the Fourier transform, and F^\dagger is its inverse. A diagonal unitary matrix has diagonal elements of the form $e^{i\phi}$, so the phase transformation seen in the previous chapter has a diagonal unitary matrix representation.

The unitary transformation described by Eq. (4.1) is agnostic to the basis it is acting on. Therefore unitary transformations on any physical basis can be decomposed in this way; including transformations modes of light such as temporal modes, spatial modes, and polarization.

The ability to use this theorem to create an arbitrary unitary transformation has been demonstrated in the spatial domain in [Mor+10], where the diagonal Unitary matrices are implemented phase transformations using deformable mirrors, and the Fourier transform takes place over free space propagation. With analogous methods to implement the diagonal unitary matrices and Fourier transforms, we propose to perform the arbitrary unitary transformations on a set of temporal modes.

4.2 Temporal Mode Implementation

In terms of the temporal modes the diagonal unitary matrices of Eq. (4.1) are equivalent to phase modulations in the time or frequency domains. So the decomposition of the unitary transformation consists of a series of phase modulations separated by Fourier transforms. As we saw in the previous chapter, temporal and spectral phases can be applied to a temporal mode using electro-optic modulation. Driven with the proper RF signals these phase modulations can be tailored to match each diagonal unitary in the decompositions.

Also, in the previous chapter we saw that the dispersive Fourier transform can

be used to effectively apply the Fourier transform to an optical pulse. This requires the use of a dispersive element to provide enough GDD to match the far-field condition. Equivalently, the inverse dispersive Fourier transform can be applied by using a dispersive element with a negative GDD.

So to apply an arbitrary unitary transformation on temporal modes, the implementation of the decomposition takes the form of an alternating series of phase modulations and dispersive Fourier transforms. Then we propose an apparatus, shown in Fig. 4.1, that can be used to apply these arbitrary unitary transformations. An optical pulse is sent through a series of electro-optic phase modulators, each driven by an RF signal that applies a phase modulation as required by the decomposition. Between the EOMs are circulators that send the pulse through chirped fiber Bragg gratings (CFBGs) that can apply the large amount of GDD needed for the dispersive Fourier transform.

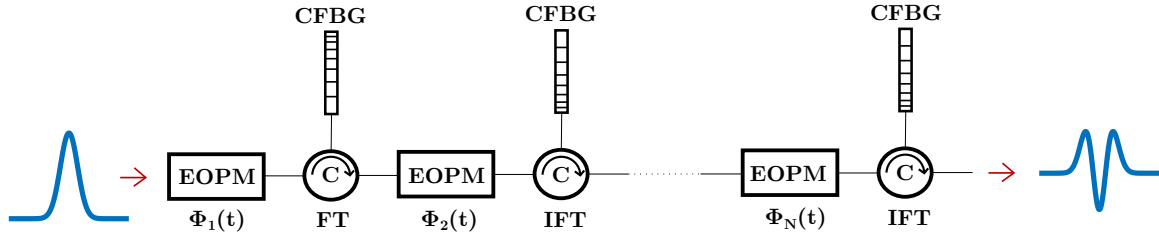


Figure 4.1. The proposed experimental setup

4.3 Simulation

Although theorem behind Eq. (4.1) proves that any unitary transformation on the temporal modes can be decomposed into a sequence of temporal phase modulations and Fourier transforms, it does not provide a prescription for determining the form of the phase modulations required for any particular transformation. So

to demonstrate that this unitary decomposition can be implemented on temporal modes, we perform numerical simulations to find an optimal set of phase modulations for a particular transformation. Additionally, the theorem places no limits on the shapes or widths of the temporal modes involved, or on the bandwidth of the phase modulations. For practical reasons we restrict these simulations to account for the finite bandwidths of the EOPMs and their driving electronics, as well as reasonable limits on the amount of GDD that can be applied.

Single-mode transformations

We begin with a single-mode transformation, in which the unitary we want to implement transforms an input mode $\psi(t)$ to an output mode $\xi(t)$.

The simulation begins by generating a set of random phase modulations $\{\Phi_j(t)\}$, $j = 1, \dots, N$, where N is a variable that defines the length of the decomposition. The phases are generated within a range $[-\pi, \pi]$. To account for the finite bandwidth restrictions that will be imposed by EOMs and the driving electronics we generate the phase modulations at a sampling rate $2B$, where B is the limited bandwidth, and the full phase modulation is created using the sampling theorem. With this set of phase modulations we compute the effect of the transformation $T = \hat{F}^\dagger D_N \cdots \hat{F} D_2 \hat{F}^\dagger D_1$ on the input mode $\psi(t)$, resulting the output $\chi(t)$. We compare the output of the simulation to the targeted output mode $\xi(t)$ by calculating the fidelity, defined as

$$F = \left| \int \chi^*(t) \xi(t) dt \right|^2, \quad (4.2)$$

where $F \leq 1$. The ideal transformation will have a fidelity of $F = 1$. The phase modulations are then optimized using a simulated annealing algorithm [KGV83]. The algorithm generates a second set of phase modulations $\{\Phi'_j(t)\}$ by randomly

perturbing a small sample of phase modulations from the original set. We compute the effect of the transformation again using the new set of phase modulations resulting in a new output mode $\xi'(t)$ and a new fidelity F' . The success of the new set of phase modulations is compared to the original set by computing $\Delta F = F' - F$. The algorithm begins with a "temperature" K , initially set to a large number. We make the decision to keep the new set of phase modulations with probability $P(\Delta F) = e^{\Delta F/K}$, otherwise we keep the old set. This process is repeated, generating a new set of phase modulations each time and comparing the fidelity of the results. Initially K is set to a large number, so that the chance of keeping a new set of phases is high even if the new fidelity is smaller than the old one; but K is decreased with each iteration, making that probability smaller, and the simulation will converge to a maximum fidelity.

For our first example we simulate the transformation of a 0th-order HG mode with a temporal width of 10 ps to a 5th-order HG mode with the same width. We restrict the bandwidth to $B = 40$ GHz, and we run the simulation for several values of the decomposition length N . The results of the simulation are shown in Fig. 4.2. We see that for a decomposition consisting of two phase modulations the simulation does not reach a high fidelity. But for a decomposition with a length of four phase modulations the simulated output mode looks similar to the 5-th order HG mode, with a fidelity of $F = 0.944$. The fidelity continues to increase with the length of the decomposition, reaching $F = 0.994$ at $N = 8$. So as the number of phase modulation steps increases the fidelity appears to converge to 1.

Additionally, for this transformation we investigate the effect of the bandwidth limit on the fidelity. We simulate the same transformation for several values of the bandwidth B over large number of steps to see how the fidelity converges. The results are shown in Fig. 4.3. We see that, in general, a larger bandwidth allows the

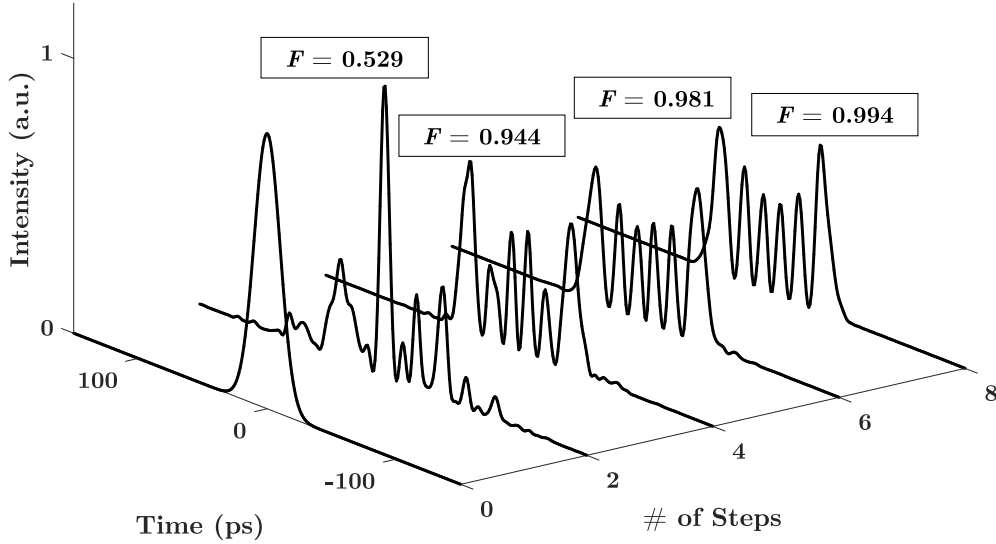


Figure 4.2. The transformation of a 0th-order HG mode to a 5-th order HG mode for various values of N . After 4 steps the transformed begins to have the 6-peaked character of the 5-th order HG mode. After 8 steps the transformation achieves a very high fidelity of $F = 0.994$.

transformation to reach a higher fidelity. A bandwidth of 5 GHz is unable to a high fidelity, even for a large number of steps. But for bandwidths of 10 GHz or more the transformation can reach a fidelity of greater than 0.9 and may even converge to 1 as the number of steps increases. It should be noted that the bandwidth required to reach a high Fidelity will depend on the width of the temporal mode being transformed.

Multi-mode transformations

Now we turn our attention to multi-mode transformations. Here we consider a transformation on a subspace of M modes, defining an $M \times M$ -dimensional unitary

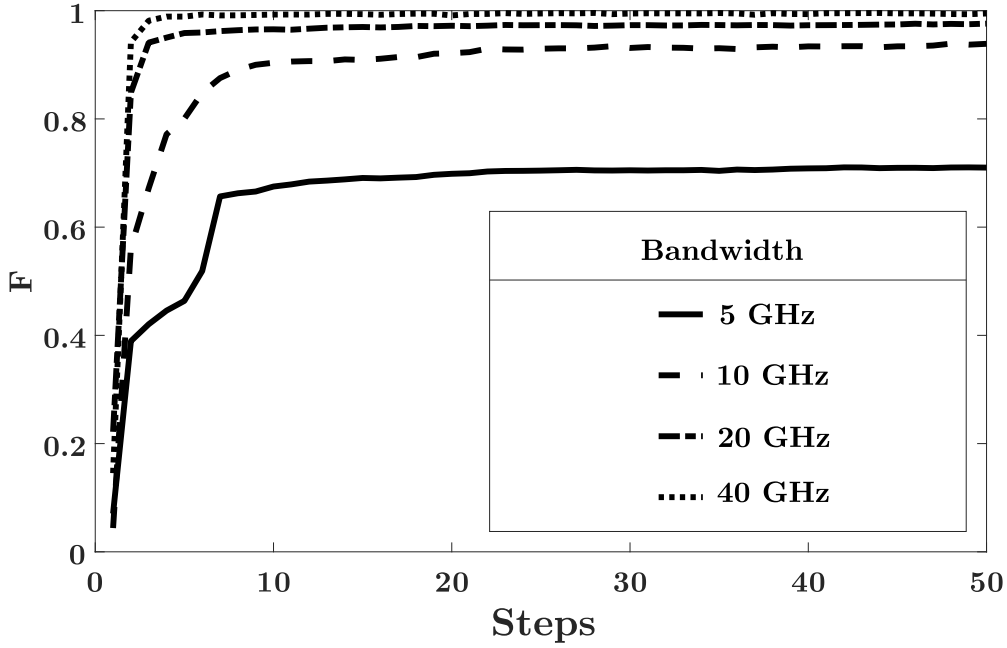


Figure 4.3. The transformation of a 0th-order HG mode to a 5-th order HG mode is simulated for various values of of the bandwidth B and the fidelity F is computed after a certain number of steps. The fidelity appears to approach a maximum that depends on the bandwidth.

matrix U . For these simulations we choose a set of input modes $|\psi_j\rangle$, $j = 1, \dots, M$, and a set of output modes $|\xi_j\rangle$, $j = 1, \dots, M$, where $|\xi_j\rangle$ is a linear combination of the input modes. The transformation U maps the input modes to the output modes as $|\xi_j\rangle = U|\psi_j\rangle$. The the matrix elements of this transformation are

$$U_{ij} = \langle \psi_i | \xi_j \rangle = \int \psi_i^*(t) \xi_j(t) dt. \quad (4.3)$$

We simulate multi-mode transformations as we did with the single-mode transformation, but now we compute the result of the unitary decomposition T on each input mode, resulting in a set of output modes $|\chi_j\rangle$, $j = 1, \dots, M$. The matrix elements of the simulated transformation T are

$$T_{ij} = \langle \psi_i | \chi_j \rangle = \int \psi_i^*(t) \chi_j(t) dt. \quad (4.4)$$

To evaluate how close the simulated transformation is to the desired unitary transformation, we construct the matrix T by computing all the elements T_{ij} . Then we can quantify the effectiveness of the transformation by defining the fidelity for multi-mode transformations as

$$F = \frac{1}{M^2} |Tr(T^\dagger U)| \quad (4.5)$$

It is possible that an imperfect transformation may include output modes that are outside the M mode subspace. To account for this, we introduce two new quantities. The first of these is the success probability

$$P = \frac{1}{M} Tr(T^\dagger T) \quad (4.6)$$

This is that probability, or the degree to which the output modes remain within the subspace. The other quantity is the Hilbert-Schmidt fidelity [WYY08]

$$F_{HS} = \frac{1}{M^2} \left| \frac{Tr(T^\dagger U)}{P} \right|^2 \quad (4.7)$$

Which is the fidelity normalized by the success probability. For the simulation the phases are optimized to maximize the fidelity, then we compute the success probability and the Hilbert-Schmidt fidelity to evaluate the performance.

Beam-splitter Transformation

To begin with we demonstrate the ability to perform a beam-splitter-like transformation between two Hermite-Gaussian modes. This transformation is represented by a 2-by-2 matrix as

$$U = \frac{1}{\sqrt{2}} \begin{pmatrix} 1 & 1 \\ 1 & -1 \end{pmatrix}. \quad (4.8)$$

For this simulation we choose the 0th and 5th order HG modes, both with a $\sigma = 10ps$ duration. The optimized output modes are shown in Fig. 4.4, displaying the real and imaginary parts along with the targeted outputs.

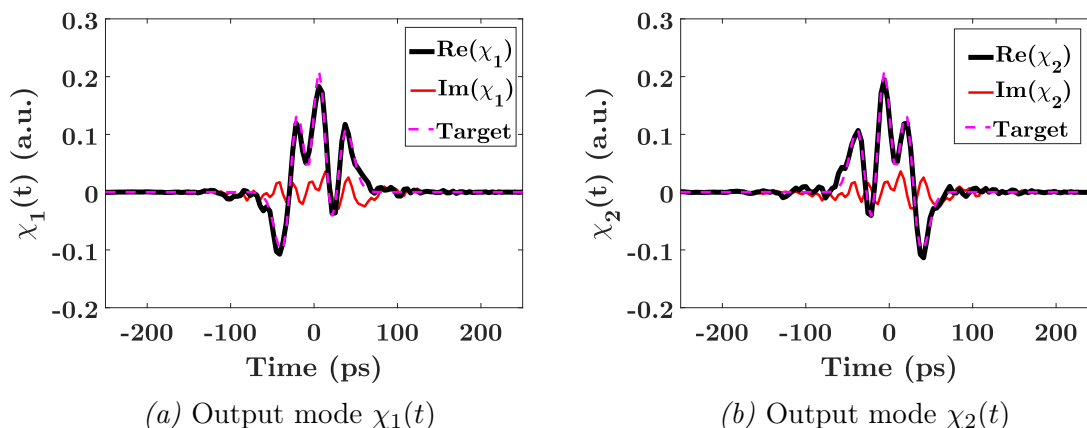


Figure 4.4. The temporal amplitude of the output modes of the simulated beam-splitter transformation. The simulation assumes a phase modulation bandwidth of $B = 20$ GHz, optimized over $N = 6$ phase steps. The temporal amplitude of the target modes are displayed as dashed lines.

Calculating the fidelity of the output modes themselves we find $F_1 = 0.923$ and $F_2 = 0.952$ respectively. Rapid oscillations in the output modes can be seen well outside the width of the desired modes. This can be interpreted as loss into higher-order HG modes outside of the two-mode subspace. Indeed, the success probability of this transformation is $P = 0.941$, less the ideal value of 1. After the computing the matrix elements, the optimized transformation is represented by the matrix

$$T = \frac{1}{\sqrt{2}} \begin{pmatrix} 0.96 - 0.10i & 0.98 - 0.03i \\ 0.96 - 0.02i & -0.97 - 0.01i \end{pmatrix} \quad (4.9)$$

Comparing this matrix to the desired beam-splitter transformation of Eq. (4.8), the Hilbert-Schmidt fidelity of the optimized transformation is $F_{HS} = 0.999$. This

indicates that despite the fact that there is overall loss into external HG modes, the optimized transformation performs well in the two-mode subspace.

Four mode beam-splitter transformation

In principle, we should be able to perform arbitrary unitary transformations on an arbitrarily large number of modes. However, large dimensional transformations may be restricted by practical constraints, and may require a large amount of resources. As an example of a unitary transformation beyond two modes, we simulate a four-mode beam-splitter transformation. This is represented by the unitary matrix

$$U = \frac{1}{2} \begin{pmatrix} 1 & 1 & 1 & 1 \\ 1 & -1 & 1 & -1 \\ 1 & 1 & -1 & -1 \\ 1 & -1 & -1 & 1 \end{pmatrix}. \quad (4.10)$$

We simulate this transformation with a bandwidth $B = 20GHz$ and using $N = 12$ phase steps. After computing the matrix elements, the optimized transformation is

$$T = \frac{1}{2} \begin{pmatrix} 0.67 + 0.07i & 1.00 + 0.04i & 1.10 + 0.01i & 0.80 - 0.47i \\ 1.01 + 0.00i & -0.98 - 0.02i & 0.75 - 0.07i & -0.85 + 0.12i \\ 0.98 - 0.03i & 0.98 + 0.08i & -0.91 + 0.07i & -0.89 + 0.07i \\ 0.95 + 0.01i & -0.68 - 0.05i & -0.86 + 0.01i & 1.16 - 0.11i \end{pmatrix} \quad (4.11)$$

Comparing this transformation to the desired Four-mode beam-splitter transformation we find a Hilbert-Schmidt fidelity of $F_{HS} = 0.975$ and a success probability of $P = 0.852$. Here we see that even though this transformation was optimized using

more steps than the two-mode beam-splitter, the fidelity and the success probability are lower. Fig. 4.5 shows the Hilbert-Schmidt fidelity and the success probability for the optimized two and four mode beam-splitter transformations at different values of N . The Fidelity converges toward 1 more slowly for the four-mode transformation. The proof of the decomposition of Eq. (4.1) does not give any information about how many elements are needed for any particular transformation, but these results suggest that for an increasing number of modes, the number of steps required to perform the transformation will increase as well.

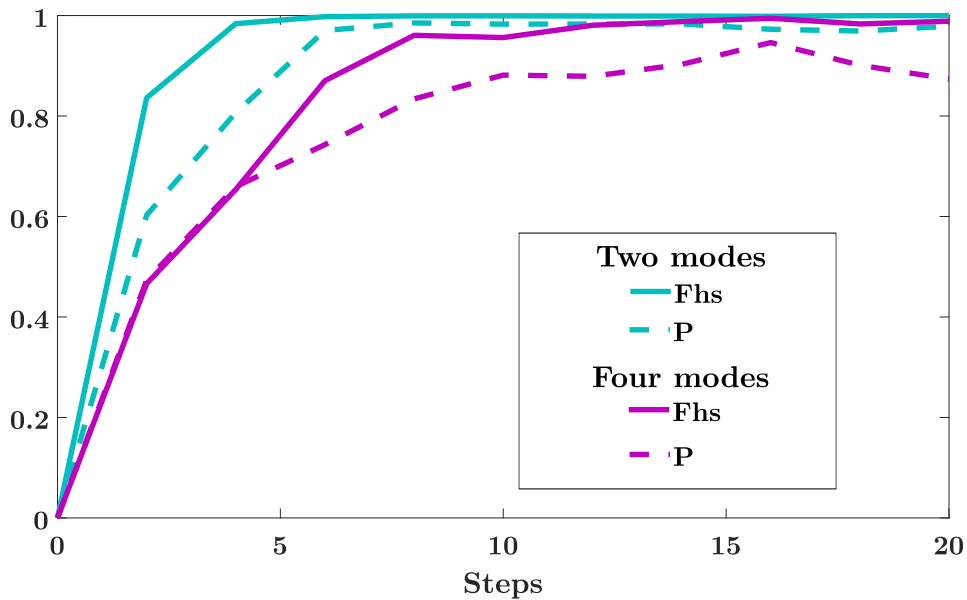


Figure 4.5. The Hilbert-Schmidt fidelity and the success probability as a function of the number of phase modulation steps for the two and four mode beam-splitter transformations

Demultiplexing

As an another example of a unitary transformation that can be performed using this technique we demonstrate the ability to demultiplex a number of HG

modes, separating them in time such that a fast detector could distinguish by the arrival times.

We simulate this operation on the first three HG modes with a temporal duration $\sigma = 20ps$, demultiplexing them into Gaussian pulses separated in time by $200ps$. We calculate the single-mode fidelity of each individual output mode, comparing them to the desired Gaussian, optimize to maximize the average sum fidelities over each mode. The results of this simulation are shown in Fig. 4.6 for an increasing number $N = 0, 4, 8, 12$ of phase steps. After four steps the initial modes appear to be splitting into separate time bins but still have a lot of overlap with each other; compared with the target modes, the average fidelity at this step is $F = 0.478$. After eight steps the modes are clearly separated into their respective time bins, but they still have a lot of oscillating features overlapping with the other modes; the average fidelity at this step is $F = 0.876$. After twelve steps the modes are demultiplexed into the target modes with an average fidelity of $F = 0.977$.

Another way to evaluate the efficacy of this transformation for demultiplexing is to calculate the average signal-to-noise ratio (SNR) across the time bins. The SNR for each time bin given by the ratio of the energy in each time bin arising from the targeted mode to the energy in each time bin from the other two modes. For this transformation we find an SNR of 187, 66, and 88 for modes 0, 1, and 2 respectively. We see that this system is capable of performing the demultiplexing operation on three modes..

Practical Comments

The simulations we have demonstrated here have not included the effect of loss. Because only phase operations are involved in creating the temporal mode

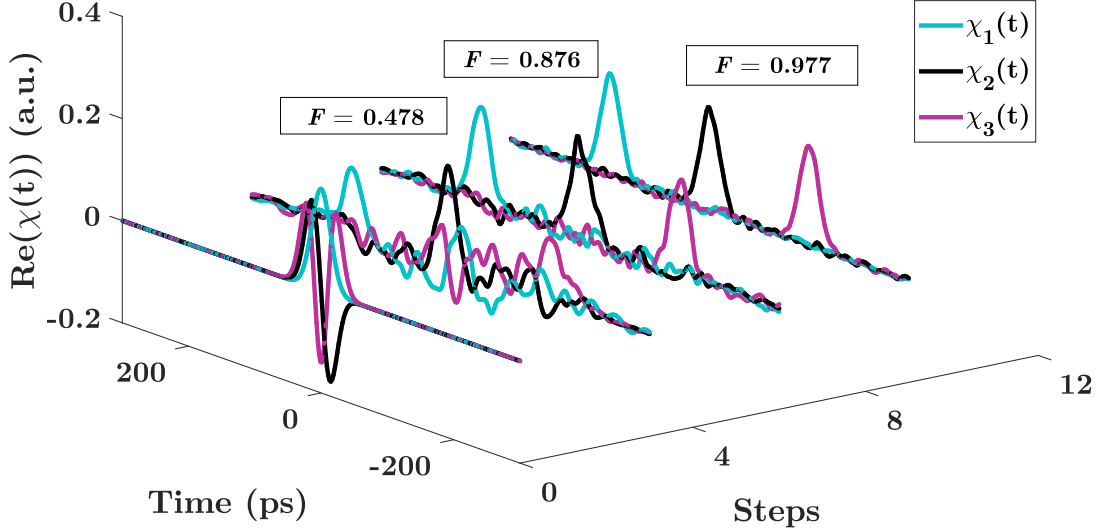


Figure 4.6. Demultiplexing the temporally overlapped Gaussian (turquoise), a 1st-order HG (black), and 2nd-order HG (magenta) pulses into temporally separated Gaussian pulses for an increasing number of phase modulation steps. The initial temporally overlapping HG pulses and target pulses have widths $\sigma = 20$ ps. The target Gaussian modes are separated by 200 ps. The average fidelity is shown for each transformation.

transformations, in principle the transformation should be lossless. However, a realistic experimental setup that implements these transformations will include components and connections between them that will introduce loss to the system. We do not anticipate time- or frequency- dependent losses at the time scales considered for our proposed transformations. But insertion losses can occur out each connection between the optical components. For instance, the EOM used in the experiments of chapter 3 has a stated insertion loss of 3.6 decibels. Insertion losses will have the effect of lowering the the transmission possibility of the transformation. A potential solution to this issue is to use low-loss integrated photonic circuits, which are in

active development [Man+16; Els+20].

CHAPTER 5

CREATING AND MEASURING ARBITRARY PHASE MODULATIONS

In the previous chapter we showed that it is possible to create arbitrary unitary transformations on the temporal modes using a series temporal and spectral phase modulations. In Chapter 3 we demonstrated that electro-optic phase modulation is an effective way to create temporal phase modulations. In this chapter we turn our attention to the problem of creating phase modulations of the form needed to implement arbitrary transformations such as those that have been simulated. We show that these programmable phase can be created through the use of photonic arbitrary waveform generation, and we use the spectral interferometry technique described in Chapter 3 to measure the shape these temporal phase modulations.

5.1 Photonic Arbitrary Waveform Generation

The phase modulations needed to performs arbitrary unitary transformations, under our experimental restrictions, will be on picosecond time scales. We will thus need RF signals on the same scale to drive these modulations, and they must also be programmable to match the desired modulation. Such programmable RF signals are typically created using arbitrary waveform generators (AWG). Current state-of-the-art AWGs can generate signals with rise times as low as 3 ps. But there are alternative all-optical ways to generate programmable RF signals.

Photonic arbitrary waveform generation (PAWG) is a technique which generates shaped broadband RF waveforms using high-speed photodetection of an optical pulse. This requires first shaping an optical pulse in the time domain using an ultrafast pulse shaping technique. There are many approaches to pulse shaping for photonic arbitrary waveform generation: direct space-to-time pulse shaping [LW01],

shaping through the use of optical frequency combs [Tan+20], or by using the temporal Talbot effect [Chi+21]. The approach we will focus on uses Fourier transform pulse shaping and frequency-to-time mapping [LMW05], to create a pulse with a shaped temporal profile suitable for PAWG.

Pulse Shaping

Ultrafast pulse shaping is a set of techniques that allow for nearly arbitrary control over the spectrum and temporal profile of an ultrafast optical pulse in the femtosecond or picosecond regimes [Wei11]. The particular technique we will focus on is Fourier transform pulse shaping which uses Fourier optics to modulate the spectrum of a pulse, in turn having an effect on the temporal profile. Whereas modulating the pulse in the time domain directly would require fast modulators; Fourier transform pulse shaping is passive.

A Fourier transform pulse shaper involves the use of a 4f-line, a diagram of which is shown in Fig. 5.1

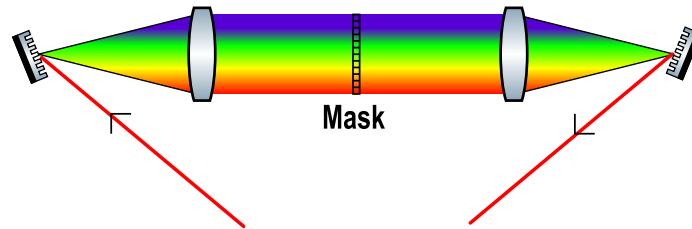


Figure 5.1. Diagram of a 4f-line Fourier transform pulse shaper. Made up of a pair of gratings and lenses, and a mask placed at the Fourier plane.

This approach involves the use of a grating-pair in a zero-dispersion configuration, a pair of lenses, and a mask [WHK88]. The first grating disperses the spectral components of a pulse across a range of angles and a lens focuses these spectral components to a point at the Fourier plane. A mask placed at the Fourier plane is

used to modulate the spectrum. The second lens and grating are used to recompress the spectral components, resulting in a shaped optical pulse. If we define the mask by the transfer function $H(\omega)$ then the output spectrum of the pulse shaper will be

$$u_{out}(\omega) = H(\omega)u_{in}(\omega) \quad (5.1)$$

Alternatively, the mask can be expressed in the time domain using the Fourier transform

$$h(t) = \int H(\omega)e^{-i\omega t} \quad (5.2)$$

The output temporal profile of the pulse can be obtained by convolving the input temporal profile by the $h(t)$

$$u_{out}(t) = \int u_{in}(\tau)h(t - \tau)d\tau \quad (5.3)$$

Then the problem of creating a pulse with a desired temporal profile amounts to finding the appropriate mask $H(\omega)$ that shapes the corresponding spectrum.

Fourier transform pulse shaping is often performed using a liquid crystal spatial light modulator (SLM) for the mask [Wei00]. An SLM is an array of independently controlled pixels that modulate the amplitude and phase of the incident light. Then, placed at the Fourier plane in a 4f-line, the SLM can be used to modulate the spatially dispersed spectral components according to an applied mask.

Fourier transform pulse shaping can effectively create pulses on a femtosecond time scale. But on a picosecond time scale the bandwidth of a pulse is too small to feasibly be modulated with a 4f-line with high enough resolution. To create pulses on a picosecond time scale we use frequency-to-time mapping.

As we saw in Chapter 3, we can use the dispersive Fourier transform to map frequency-to-time, such that the temporal profile of the pulse is a scaled version

of the spectrum. So to get a specific shape of the pulse in the time domain we can first shape the spectrum using Fourier transform pulses shaping. We then add dispersion at the output of the 4f-line, which stretches the pulse in time and performs the dispersive Fourier transform. By doing this we can create shaped pulses on picosecond time scales.

Photonic Arbitrary Waveform Generation.

A photonic arbitrary waveform generator (PAWG) uses a fast photo-diode to create a shaped RF signal from an optical pulse which can then be used for temporal phase modulation. The temporal profile of the resulting RF signal will be a convolution of the pulse and the impulse response of the photodiode. This will create an RF that with a similar shape to that of the optical pulse used to create it.

5.2 Creating Arbitrary Phase Modulations

We use PAWG to create arbitrary phase modulations. Our PAWG uses the Fourier transform pulse shaping technique along with frequency-to-time mapping to create the temporal profile of the RF signal that is generated.

A diagram of our PAWG is shown in Fig. 5.2. A pulse enters via fiber and passes through a set of half and quarter waveplates that are used to control the polarization of the pulse. It then enters a Fourier transform pulse shaper similar to the 4f-line described above, but set to work in a reflection configuration. A single diffraction grating disperses the spectral components over a range of angles. Instead of a lens, a cylindrical mirror is used to focus the spectral components into a horizontal beam at the Fourier plane. A SLM is placed at the Fourier plane of the mirror, perpendicular to the incoming beam.

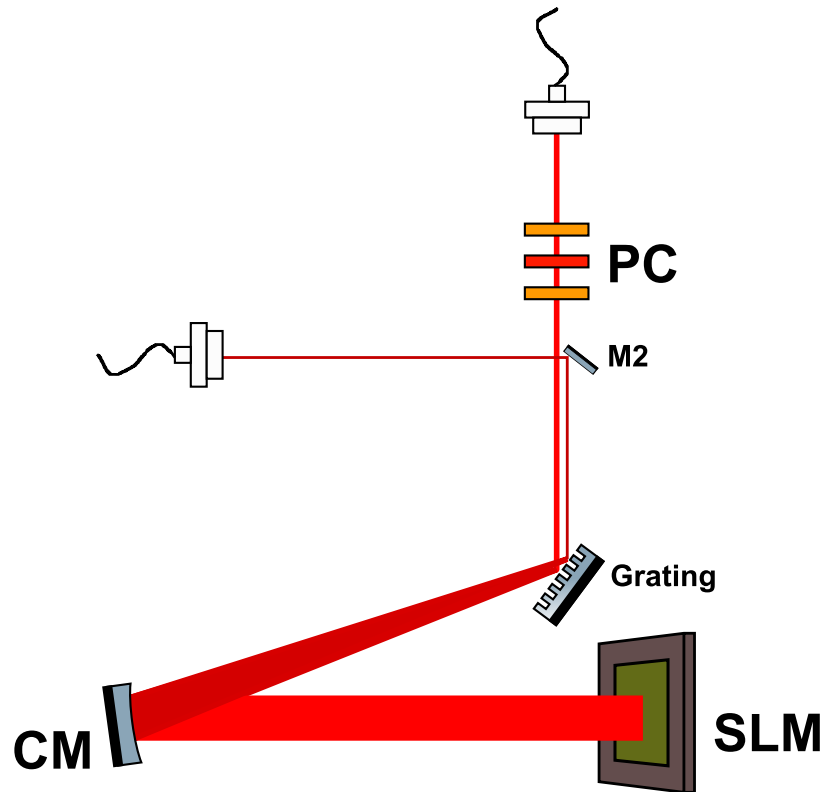


Figure 5.2. A schematic of the pulse shaper. A polarization controller (PC) set the polarization to the optimal wavelength. A grating disperses the beam across a range of angles. The cylindrical mirror (CM) collimates the beam. An SLM is placed at the Fourier plane of the mirror. The reflected beam is spatially separated and directed to a fiber coupler by the mirror M2.

The SLM consists of 1272×1024 pixels controlled by PC via a DVI interface. Each pixel can be set to one of 256 grey-scale levels, which determines the phase shift imparted by the pixel. Although the SLM can only modulate phase, it can be used to control both the amplitude and phase of the spectral components with a mask that creates a phase grating vertically on each column of the SLM [FS09]. The SLM is slightly tilted vertically so that the outgoing beam is spatially separated from the incoming beam. The outgoing beam is focused by the cylindrical mirror and recombined on the grating. Being spatially separated from the incoming

beam, it is picked off by another mirror and coupled into fiber.

Frequency-to-time mapping is performed using 250 m of fiber, with a group delay dispersion of 10 ps^2 . The dispersed pulse is detected using the DX25CF photodiode, which generates an RF signal. Since the width of the optical pulse after dispersion is much longer than the impulse response of the photodiode, the RF signal will be an approximate replica of the temporal profile of the pulse. This RF signal is amplified and used to drive the EOM, causing a phase modulation with a shape determined by the shape of the optical pulse created using the pulse shaper.

5.3 Measurement

Equipped with the techniques of pulse shaping and PAWG, we can measure temporal phase modulations of various shapes driven a shaped RF driving signal. We measure these phase modulations are measured using the spectral interferometry technique demonstrated in Chapter 3. The setup for measuring phases created using PAWG is shown in Fig. 5.3

The setup is similar to that used for the previous spectral interferometry measurements, with the extra inclusion of the Fourier transform pulse shaper. The pulse that passes through the delay line is sent through the pulse shaper. The SLM is controlled by sending a programmed mask via the DVI interface. Frequency-to-time mapping is performed using a 250 m which has a $\Phi_{\omega}^{(2)}$ of 10 ps^2 . The end of the fiber is connected to the input of the photodiode, where it is detected. The RF signal from the photodiode is amplified and used to drive the EOM. The probe path is the same as the previous spectral interferometry measurements. The pulse is diagonally polarized and chirped using a 500 m fiber before it is sent through the EOM. The two time-delayed orthogonally polarized pulses are interfered using a

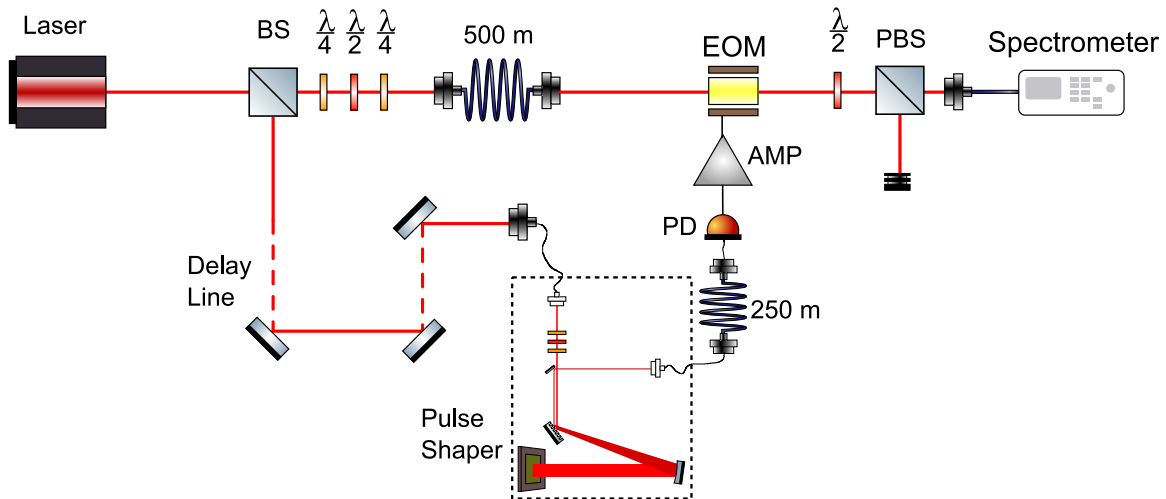


Figure 5.3. The PAWG measurement setup uses the same measurement scheme to the spectral interferometry measurement in chapter 3, but the output of the delay line is sent through PAWG. The pulse shaper is equipped with a SLM to shape the spectrum of the pulse. A 250m optical fiber is used for frequency-to-time mapping. The output of the fiber is detected by the fast photodiode, converting it into an RF signal that is amplified and used to drive the EOM.

polarizing beam-splitter and the spectrum is measured on the spectrometer. The phase modulation is extracted using the same procedure as before.

To demonstrate the versatility and effectiveness of PAWG for temporal phase modulation we present measurements for several different phase shapes. These shapes all have potentially useful applications. The first phase we demonstrate is a triangle phase, which consists of two linear sections with opposite slopes. First a triangular optic pulse is shaped using PAWG. An example of the SLM mask used to create the triangle shape is shown in Fig. 5.4, showing the phase grating pattern used to perform both amplitude and phase modulation. The mask is designed to compensate for the Gaussian shape of the input pulse by scaling the higher on the wings than in the center. The output pulse will thus have less total energy, but it will more accurately create the desired shape.

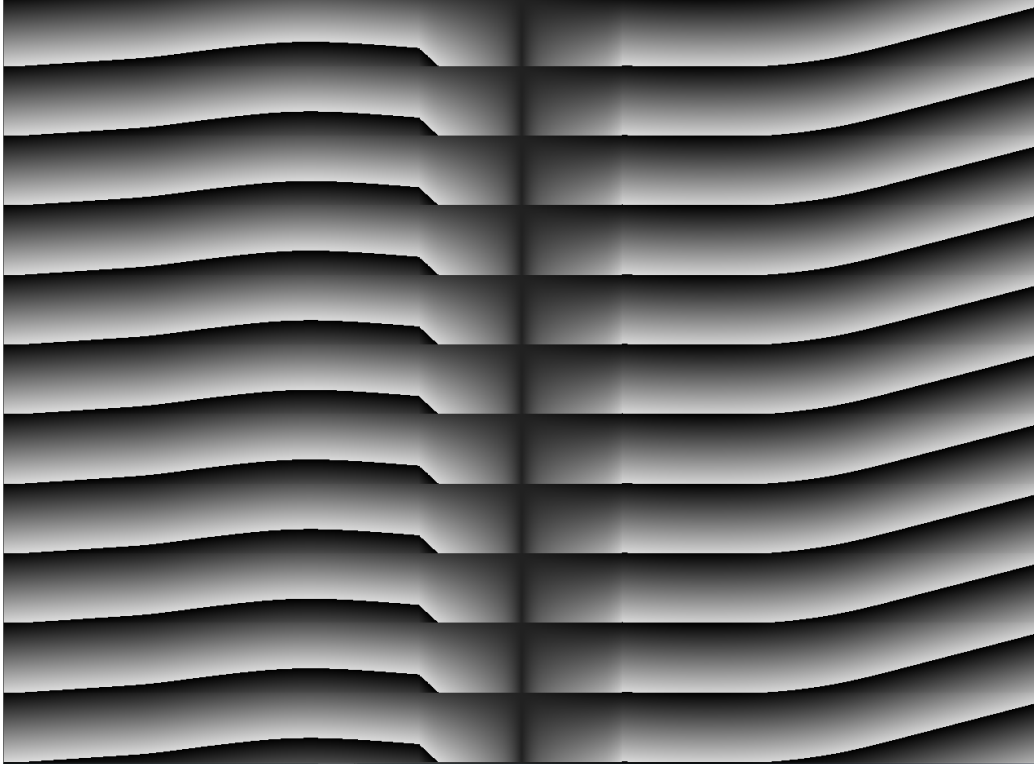


Figure 5.4. The 1272 x 1024 pixel mask sent to the SLM, used to create a pulse with a triangular shape.

The measurement of the triangle phase, extracted from spectral interferometry is shown in Fig. 5.5. The phase is triangular, with two approximately linear sections of opposite slope on either side. It has a FWHM of approximately 200 ps. The peak of the phase itself is not sharp as the ideal triangle would be, this is due to the resolution of the pulse shaper limiting the precision with which the shape can be defined. Additionally, while a truly triangular pulse would have a bandwidth of infinite extent, the higher frequency components of the photodiode RF signal will be filtered out by the finite bandwidth of the amplifier and the EOM; leading to a phase with limited sharpness. The jumps in the phase at the edges of the measurement are likely due to the difficulty of measuring the phase at the edges of the probe where the intensity is small.

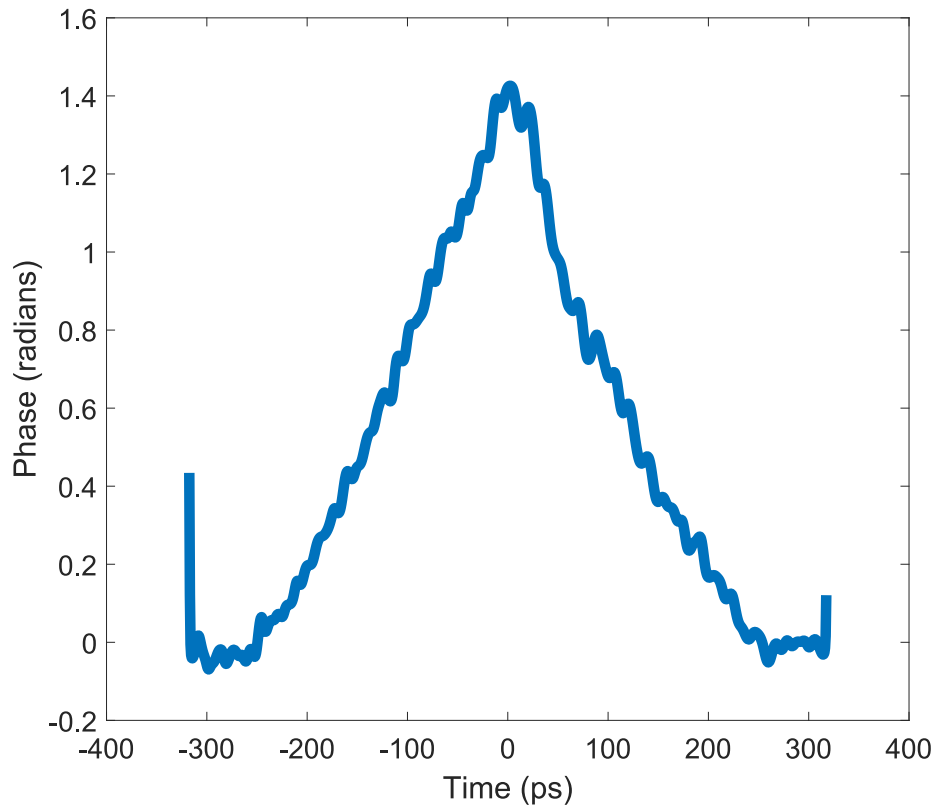


Figure 5.5. The measurement of the phase modulation using a triangular driving signal created using PAWG. The phase is extracted from a spectral interferometry measurement.

As another example we create a rectangular phase modulation. Ideally the rectangle phase would have an instantaneous rise and fall time, and a completely flat top. The result of the phase modulation measured through spectral interferometry is shown in Fig. 5.6.

We find a rectangular phase with an FWHM of approximately 400 ps. The top of the phase is nearly flat but appear to be lower on the right side. Notably, the rising and falling edges of the phase are not instantaneous. It takes approximately 40 ps for the phase to rise to the top from 0 radians, and it takes a similar amount

of time to fall. These rise and fall times fit with the explanation that the speed of the phase modulation is limited by the 20 GHz bandwidth of the EOM.

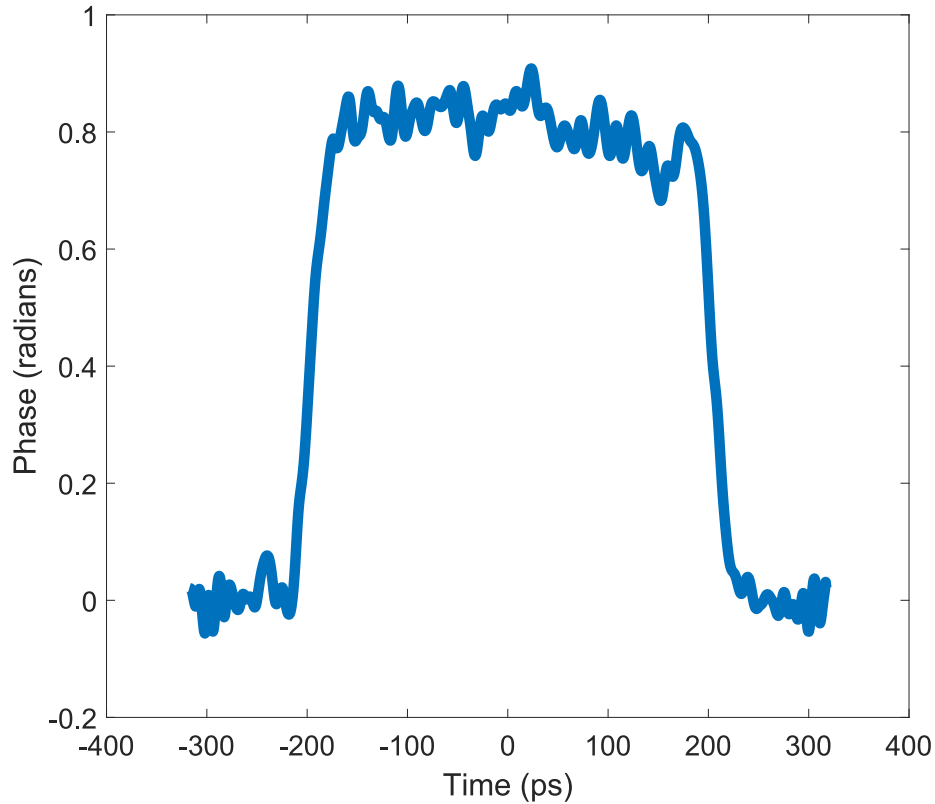


Figure 5.6. The measurement of a rectangular phase created using PAWG. The phase is extracted from a spectral interferometry measurement.

As a final example we create a phase in the shape of a series of peaks of constant width and constant period. The result of the spectral interferometry measurement of this phase modulation is shown in Fig. 5.7. In the measured phase we find six peaks at a period of approximately 105 ps. Each peak has a FWHM of approximately 30 ps. They are nearly the same height, with the later peaks having a slightly lower amplitude than the earlier peaks, similar to what we saw in the rectangular phase. The difference in the heights is likely the result of the compensation

applied to the mask to account for the Gaussian shape of the initial optical pulse being slightly misaligned. The peaks in this phase are approaching the limit of the smallest features that can be created using our PAWG system, the widths of the peaks being equal to the width of the impulse response of the photodiode.

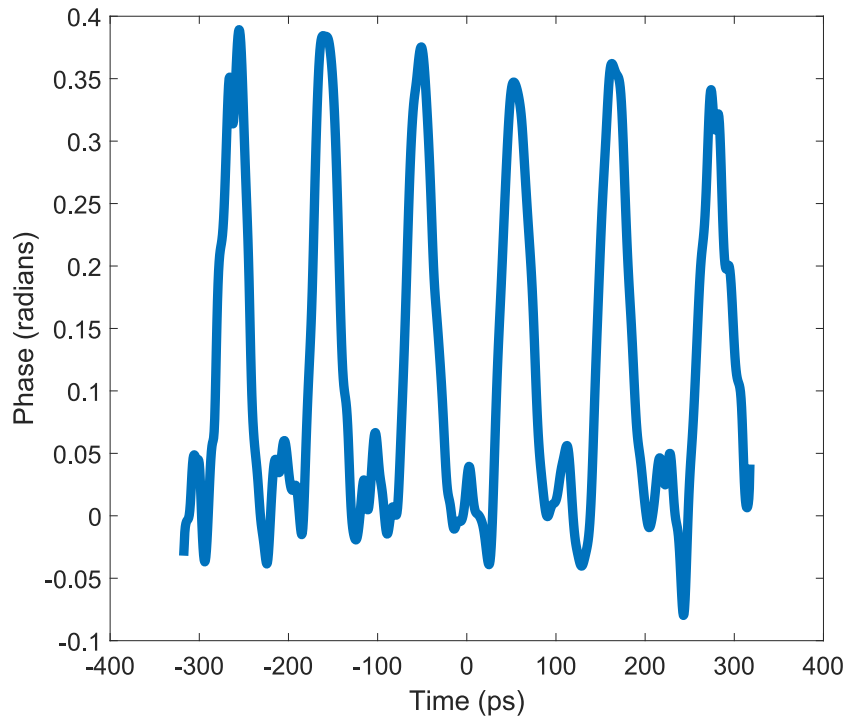


Figure 5.7. The measurement of a phase created using PAWG, consisting of a series of peaks. The phase is extracted from a spectral interferometry measurement.

Each example shown here demonstrates the ability of PAWG to create temporal phase modulations with programmable shapes. This is an important step toward implementing arbitrary unitary transformations as described in Chapter 4. In the next chapter we will discuss future steps to be taken to get closer to making the arbitrary unitary transformations a reality.

CHAPTER 6

FUTURE STEPS AND CONCLUSIONS

In this chapter we propose two experiments that will take further steps toward implementing arbitrary unitary transformations temporal modes, and make concluding remarks. The first experiment will improve on the techniques we have presented to measure and characterize phase modulations. For the second experiment we propose a design for an apparatus that can efficiently apply a series of consecutive temporal and spectral phase modulations, requiring minimal resources.

6.1 Single-Shot Phase Characterization

Each spectral measurement we have performed to characterize temporal phase modulations has been taken over an integration time of 100 ms, which is the fastest possible with our spectrometer. This means that the measurement is an average over many pulses in our 80 MHz pulse train. Therefore, these measurements are affected by timing jitter.

To limit the effect of timing jitter, we propose an experiment to perform the same phase characterization measurement in a single shot. This can be done using a pulse picker to pick probe pulses out of the pulse train a repetition rate at or below 10 Hz such that only one pulse will be detected by the spectrometer within the 100 ms integration window. The pulse picker can be created using an acousto-optic modulators (AOM) or EOMs. There currently commercially available AOMs that can be operated at the speeds necessary to create this pulse picker.

Using single-shot phase characterization measurements would allow us to get a more accurate picture of the phase modulations by limiting the effect of timing jitter on the measurement. It would also allow us to characterize the stability of

the phase modulation over time through consecutive single-shot measurements.

To our knowledge, single-shot phase characterization measurements of this type have so far never been performed.

6.2 Cavity Configuration for Arbitrary Unitary Transformations

In Chapter 4 we showed through simulations that arbitrary unitary transformations can be implemented using electro-optic modulators and dispersive elements. The number of phase modulations needed to reach a high fidelity for multimode transformations grows with the dimensionality of the transformation. For instance, a transformation on two temporal modes may require four phase modulations or more, while a transformation on four modes may require up to 16 phase modulations to achieve an adequate fidelity. Then implementing the arbitrary unitary would involve the use of many electro-optic modulators and dispersive elements, as well as the electronics and pulse shapers to create the driving signals, which may be impractical.

One way around this is the possibility of implementing the arbitrary unitary in a loop configuration as shown in Fig. 6.1. A pulse can enter the cavity via a Mach-Zehnder modulator (MZM) switch. The pulse passes through the EOM, which applies a temporal phase modulation, and then passes through a dispersive element with a GDD of $\Phi^{(2)}$. The pulse is reflected back through the dispersive element, effectively doubling the amount of dispersion. If $\Phi^{(2)}$ is large enough then the dispersive Fourier transform will be applied to the pulse, so when it passes back through the EOM it can apply a spectral phase modulation. On the other end of the cavity is a dispersive element with a negative GDD of the same magnitude as $\Phi^{(2)}$. This element applies the inverse dispersive Fourier transform, so when the pulse travels

through the EOM again it can apply a temporal phase modulation. In this way we can apply a series of consecutive temporal and spectral phase modulations as required by the arbitrary unitary transformation, using only a single EOM and two dispersive elements. After the transformation is applied the pulse can exit the cavity via the MZM switch. It should be noted that the configuration shown here requires an EOM that is operable in both directions, which may not be available. A similar setup in a loop configuration, using two EOMs instead of one, is proposed in [Thi+17].

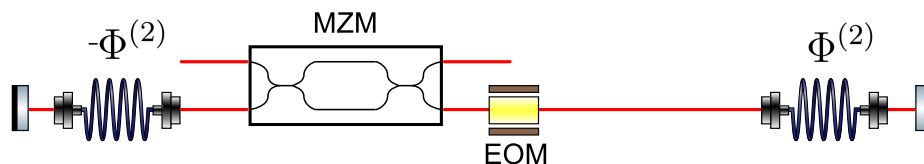


Figure 6.1. The proposed schematic for a setup that can efficiently perform many successive phase modulations to implement arbitrary unitary transformations.

One problem to consider is the creation and synchronization of the driving signals. Each consecutive phase modulation needs to be driven by the appropriately shaped RF signal. The driving signals must also be timed to arrive when the pulse passes through the EOM, which depends on the travel time through the cavity. If the dispersive elements used in the cavity are optical fibers with lengths of hundreds of meters, as we have used to apply the DFT before, then the travel time through the cavity will be on the order of $1 - 10 \mu\text{s}$. However, the SLM we used in PAWG has a rise time of 33 ms, so the switching time between different masks is very slow compared to the cavity travel time.

A potential solution is to write several different masks on the SLM simultaneously. Since the beam in the pulse shaper is dispersed horizontally before it reaches the SLM, it does not fill the entire vertical space on the mask. Then we propose

writing several masks, each designed to create their own independent pulse shape, at different vertical positions on the SLM. Then consecutive pulses passing through the pulse shaper, provided a way to vertically displace the pulses, can each be modulated by a different mask required to create the consecutive RF driving signals.

6.3 Conclusions

In this dissertation we have demonstrated the ability of temporal and spectral phase modulation to apply unitary transformations on temporal modes. We have shown that elementary linear and quadratic phase modulations can achieve remarkable control over several key properties of temporal modes, including the frequency and bandwidth; and in particular that they form a complete set of transformations on Gaussian modes.

We presented techniques capable of measuring and characterizing temporal phase modulations by exploiting the effect of the elementary modulations on the frequency and bandwidth of a temporal mode. And we presented another technique to measure that can measure both temporal and spectral phase modulations using spectral interferometry.

We showed theoretically that any unitary transformation on temporal modes can be applied by using an alternating of consecutive temporal and spectral phase modulations. To this effect we proposed an experimental scheme to perform arbitrary unitary transformations using a series of electro-optic phase modulators and dispersive elements. Assuming practical constraints on the phase modulations that can be created in the lab, we performed simulations to find the optimal series of phases for a variety of unitary transformations, showing that high fidelity transformations can feasibly be achieved with a reasonably small number of phase opera-

tions.

Needing a way to create the phase modulations required to apply arbitrary unitary transformations, we showed that programmable phase modulations can be created using photonic arbitrary waveform generation; demonstrating this by creating phase modulations for several elementary shapes and measuring them using spectral interferometry.

Finally, we proposed two experiments that would take further steps in making arbitrary unitary transformations on temporal modes a reality. Further development of these techniques will be an important step toward making temporal modes a viable platform for quantum information science and technology.

REFERENCES CITED

- [Ans+17] V. Ansari et al., *Temporal-mode measurement tomography of a quantum pulse gate*, Phys. Rev. A **96** (6 2017), 063817, DOI: 10.1103/PhysRevA.96.063817.
- [Ash+20] J. Ashby et al., *Temporal mode transformations by sequential time and frequency phase modulation for applications in quantum information science*, Opt. Express **28** (2020), no. 25, 38376–38389, DOI: 10.1364/OE.410371.
- [BB14] C. H. Bennett and G. Brassard, *Quantum cryptography: Public key distribution and coin tossing*, Theoret. Comput. Sci. **560** (2014), 7–11, DOI: <https://doi.org/10.1016/j.tcs.2014.05.025>, Theoretical Aspects of Quantum Cryptography – celebrating 30 years of BB84.
- [Ben80] P. Benioff, *The computer as a physical system: A microscopic quantum mechanical Hamiltonian model of computers as represented by Turing machines*, J. Stat. Phys. **22** (1980), no. 5, 563–591, DOI: 10.1007/BF01011339.
- [Ben82] ———, *Quantum Mechanical Models of Turing Machines That Dissipate No Energy*, Phys. Rev. Lett. **48** (23 1982), 1581–1585, DOI: 10.1103/PhysRevLett.48.1581.
- [Bre+15] B. Brecht et al., *Photon Temporal Modes: A Complete Framework for Quantum Information Science*, Phys. Rev. X **5** (4 2015), 041017, DOI: 10.1103/PhysRevX.5.041017.
- [Chi+21] H. Chi et al., *Photonic arbitrary waveform generation based on the temporal Talbot effect*, Opt. Express **29** (2021), no. 11, 16927–16938, DOI: 10.1364/OE.425209.
- [Dav+17] A. O. C. Davis et al., *Pulsed single-photon spectrometer by frequency-to-time mapping using chirped fiber Bragg gratings*, Opt. Express **25** (2017), no. 11, 12804–12811, DOI: 10.1364/OE.25.012804.
- [Dav+18] A. O. C. Davis et al., *Experimental single-photon pulse characterization by electro-optic shearing interferometry*, Phys. Rev. A **98** (2 2018), 023840, DOI: 10.1103/PhysRevA.98.023840.
- [DP85] D. Deutsch and R. Penrose, *Quantum theory, the Church–Turing principle and the universal quantum computer*, Proceedings of the Royal Society of London. A. Mathematical and Physical Sciences **400** (1985),

no. 1818, 97–117, DOI: 10.1098/rspa.1985.0070, eprint: <https://royalsocietypublishing.org/doi/pdf/10.1098/rspa.1985.0070>.

- [Els+20] A. W. Elshaari et al., *Hybrid integrated quantum photonic circuits*, Nature Photonics **14** (2020), no. 5, 285–298, DOI: 10.1038/s41566-020-0609-x.
- [Fey82] R. P. Feynman, *Simulating physics with computers*, Internat. J. Theoret. Phys. **21** (1982), no. 6, 467–488, DOI: 10.1007/BF02650179.
- [FS09] E. Frumker and Y. Silberberg, *Two-dimensional phase-only spatial light modulators for dynamic phase and amplitude pulse shaping*, J. Modern Opt. **56** (2009), no. 18-19, 2049–2054, DOI: 10.1080/09500340903199913, eprint: <https://doi.org/10.1080/09500340903199913>.
- [God13] J. B. Goda K., *Dispersive Fourier transformation for fast continuous single-shot measurements*, Nature Photonics **7** (2013), 102–112, DOI: 10.1038/NPHOTON.2012.359.
- [Kar+17] M. Karpiński et al., *Bandwidth manipulation of quantum light by an electro-optic time lens*, Nature Photonics **11** (2017), no. 1, 53–57, DOI: 10.1038/nphoton.2016.228.
- [KGV83] S. Kirkpatrick, C. D. Gelatt, and M. P. Vecchi, *Optimization by Simulated Annealing*, Science **220** (1983), no. 4598, 671–680, DOI: 10.1126/science.220.4598.671, eprint: <http://science.sciencemag.org/content/220/4598/671.full.pdf>.
- [Kim08] H. J. Kimble, *The quantum internet*, Nature **453** (2008), no. 7198, 1023–1030, DOI: 10.1038/nature07127.
- [KN89] B. H. Kolner and M. Nazarathy, *Temporal imaging with a time lens*, Opt. Lett. **14** (1989), no. 12, 630–632, DOI: 10.1364/OL.14.000630.
- [LMW05] I. Lin, J. McKinney, and A. Weiner, *Photonic synthesis of broadband microwave arbitrary waveforms applicable to ultra-wideband communication*, IEEE Microwave and Wireless Components Letters **15** (2005), no. 4, 226–228, DOI: 10.1109/LMWC.2005.845698.
- [LW01] D. Leaird and A. Weiner, *Femtosecond direct space-to-time pulse shaping*, IEEE Journal of Quantum Electronics **37** (2001), no. 4, 494–504, DOI: 10.1109/3.914397.

- [Man+16] P. Manurkar et al., *Multidimensional mode-separable frequency conversion for high-speed quantum communication*, *Optica* **3** (2016), no. 12, 1300–1307, DOI: 10.1364/OPTICA.3.001300.
- [MK18] W. W. Michał Jachura Jan Szczepanek and M. Karpiński, *Measurement of radio-frequency temporal phase modulation using spectral interferometry*, *J. Modern Opt.* **65** (2018), no. 3, 262–267, DOI: 10.1080/09500340.2017.1387676, eprint: <https://doi.org/10.1080/09500340.2017.1387676>.
- [Mon+14] C. Monroe et al., *Large-scale modular quantum-computer architecture with atomic memory and photonic interconnects*, *Phys. Rev. A* **89** (2014), 022317, DOI: 10.1103/PhysRevA.89.022317.
- [Mor+10] J.-F. Morizur et al., *Programmable unitary spatial mode manipulation*, *J. Opt. Soc. Am. A* **27** (2010), no. 11, 2524–2531, DOI: 10.1364/JOSAA.27.002524.
- [NPT99] Y. Nakamura, Y. A. Pashkin, and J. S. Tsai, *Coherent control of macroscopic quantum states in a single-Cooper-pair box*, *Nature* **398** (1999), no. 6730, 786–788, DOI: 10.1038/19718.
- [Sch+00] M. Schmid et al., *Decomposing a matrix into circulant and diagonal factors*, *Linear Algebra Appl.* **306** (2000), no. 1, 131–143, DOI: [https://doi.org/10.1016/S0024-3795\(99\)00250-5](https://doi.org/10.1016/S0024-3795(99)00250-5).
- [SFG13] R. Salem, M. A. Foster, and A. L. Gaeta, *Application of space-time duality to ultrahigh-speed optical signal processing*, *Adv. Opt. Photon.* **5** (2013), no. 3, 274–317, DOI: 10.1364/AOP.5.000274.
- [Sho94] P. Shor, *Algorithms for quantum computation: discrete logarithms and factoring*, *Proceedings 35th Annual Symposium on Foundations of Computer Science*, 1994, 124–134, DOI: 10.1109/SFCS.1994.365700.
- [Sho97] P. W. Shor, *Polynomial-Time Algorithms for Prime Factorization and Discrete Logarithms on a Quantum Computer*, *SIAM J. Comput.* **26** (1997), no. 5, 1484–1509, DOI: 10.1137/S0097539795293172, eprint: <https://doi.org/10.1137/S0097539795293172>.
- [Soś+23] F. Sośnicki et al., *Interface between picosecond and nanosecond quantum light pulses*, *Nature Photonics* **17** (2023), no. 9, 761–766, DOI: 10.1038/s41566-023-01214-z.

- [Tan+20] M. Tan et al., *Photonic RF Arbitrary Waveform Generator Based on a Soliton Crystal Micro-Comb Source*, *Journal of Lightwave Technology* **38** (2020), no. 22, 6221–6226, DOI: 10.1109/JLT.2020.3009655.
- [Thi+17] V. Thiel et al., *Programmable unitary transformation of spectro-temporal modes*, *Frontiers in Optics 2017*, Optica Publishing Group, 2017, JW4A.5.
- [Wei00] A. M. Weiner, *Femtosecond pulse shaping using spatial light modulators*, *Review of Scientific Instruments* **71** (2000), no. 5, 1929–1960, DOI: 10.1063/1.1150614, eprint: https://pubs.aip.org/aip/rsi/article-pdf/71/5/1929/19187334/1929_1_online.pdf.
- [Wei11] A. M. Weiner, *Ultrafast optical pulse shaping: A tutorial review*, *Optics Communications* **284** (2011), no. 15, 3669–3692, DOI: <https://doi.org/10.1016/j.optcom.2011.03.084>, Special Issue on Optical Pulse Shaping, Arbitrary Waveform Generation, and Pulse Characterization.
- [WHK88] A. M. Weiner, J. P. Heritage, and E. M. Kirschner, *High-resolution femtosecond pulse shaping*, *J. Opt. Soc. Am. B* **5** (1988), no. 8, 1563–1572, DOI: 10.1364/JOSAB.5.001563.
- [Wri+17] L. J. Wright et al., *Spectral Shearing of Quantum Light Pulses by Electro-Optic Phase Modulation*, *Phys. Rev. Lett.* **118** (2 2017), 023601, DOI: 10.1103/PhysRevLett.118.023601.
- [WYY08] X. Wang, C.-S. Yu, and X. Yi, *An alternative quantum fidelity for mixed states of qudits*, *Physics Letters A* **373** (2008), no. 1, 58–60, DOI: <https://doi.org/10.1016/j.physleta.2008.10.083>.
- [Zhu+22] D. Zhu et al., *Spectral control of nonclassical light pulses using an integrated thin-film lithium niobate modulator*, *Light: Science & Applications* **11** (2022), no. 1, 327, DOI: 10.1038/s41377-022-01029-7.